THE UNIVERSITY OF HULL

Numerical Modelling of Plasmas Produced by Long Pulse Lasers

being a Thesis submitted for the Degree of

Doctor of Philosophy

in the University of Hull

by

David Thomas Toft, B.Sc.

August, 1979.

VOLUME CONTAINS CLEAR OVERLAYS

OVERLAYS HAVE BEEN SCANNED SEPERATELY AND THEN AGAIN OVER THE RELEVANT PAGE

ACKNOWLEDGEMENTS

My thanks go to Dr. G. J. Pert and Dr. J. Dunning-Davies for their invaluable help and supervision during the research for, and preparation of, this thesis, and to the University of Hull for financial support during the first three years of research.

I should also like to thank Mrs. P. Reynolds and Mrs. J. Williams for their efficient typing of the final manuscript.

CONTENTS

page

CHAPTER 1

General Introduction 1

CHAPTER 2

The Hydrodynamic Code

The Model 4

Governing Equations 4

Numerical Method 8

CHAPTER 3

Laser-Target Models

Introduction 22

The Deflagration 26

Deflagration-Wave Regime 29

Self-Regulating Regime 33

D-W and S-R Regime Boundary 35

Thick Regimes 36

Regime Diagram 38

Flux Limitation 41

CHAPTER 4

Results

Introduction 46

A Computational Consideration 46

Flux Limitation 49

General Behaviour 49

Comparison with Steady-State Models 73

Conclusion 83

CHAPTER 5

The Ray-Tracing Code

Ray Tracing 84

Absorption 93

Energy Assignment 97

Test Cases 104

CHAPTER 6

Results

Introduction 116

Results 117

Conclusion 129

Appendix I 133

Appendix II 134

References 136

CHAPTER 1

The phenomena that occur when an intense laser beam interacts with matter have been of interest for some time, mainly due to the possibility of constructing a laser-driven fusion reactor. In particular a number of models describing the effect of a laser striking a plane solid target, and the behaviour of the resulting plasma, have been proposed. In 1965-66 the self-regulating model* was developed independently by Caruso et al and Krokhin et al. The validity of this model has been confirmed by experiment and shown to be applicable in the case of relatively low-powered lasers. To accommodate higher intensity lasers Fauquignon and Floux, and Bobin developed the deflagration-wave model in 1970-71. The fact that these models are really two regimes of the same basic model has been demonstrated by Puell. In 1973 Pert showed that at higher intensities the effects of thermal conduction modify these models to such an extent that it is necessary to introduce two new models, these being termed thick self-regulating and thick deflagration-wave.

An alternative method of attacking the problem is to solve the hydrodynamic equations governing the plasma motion by means of a computer code. It was found that the Lagrangian

---

*A detailed description of laser-target models, with the relevant references, is given in Chapter 3.

form of the equations of motion was the most suitable for this treatment, and a number of one-dimensional codes of this type have been written. Notable among these are, in chronological order: Fader (1), Kidder (2), Shearer and Barnes (3), Mulser(4), Nuckolls et al (LASNEX) (5), Goldman (6) and Clarke et al (7). The production of a two-dimensional code was delayed by the fact that Lagrangian coordinates become extremely difficult to work with in more than one dimension, and simple Eulerian techniques cannot handle the strong shocks produced in the problem. However with the advent of more sophisticated numerical methods the production of a working two-dimensional Eulerian code became feasible. There is now a code of this type due to Winsor at the Naval Research Laboratory Washington, and in this country there is the CASTOR code due to Christiansen, LASERB of Craxton, and 2DEL of Pert. There is also now a 2-D Lagrangian version of LASNEX at Livermore. All of these codes include, among other sophistications, the effects due to magnetic fields generated within the plasma.

The object of the first part of this thesis is to compare the results of a specially written two-dimensional code with steady-state versions of the theoretical models, and in particular to examine the 'thick' models of Pert and to determine the extent to which these models are lost due to flux limitation effects. To ensure that a steady-state is attained, relatively long runs of the computer code are required; therefore the code was reduced to the

simplest form that could still model the physical situation adequately. Hence sophistications such as magnetic field effects were neglected. These omissions are justified since it is basically hydrodynamic effects that are of interest. In Chapter 2 the plasma model is described, the equations of motion are presented, and a description is given of the computer code. Chapter 3 examines the various analytic steady-state models and Chapter 4 presents the results of the computer code and compares them with the models of the previous chapter.

The second part of this thesis deals with the development of a ray-tracing code to examine the effects of refraction in a laser-plasma interaction. The code is described in Chapter 5 and the results obtained presented in Chapter 6.

CHAPTER 2

(i) The Model

The model consists of an initially plane, cold, but fully ionized hydrogen target, upon which the laser is perpendicularly incident. The resulting plasma is fully ionized and quasi-neutral; the ions are singly charged, and both ions and electrons are perfect gases. The plasma flow is treated macroscopically, the component temperatures being considered distinct. Cylindrical symmetry about the axis of the laser beam is assumed.

The absorption of laser energy in the underdense plasma is assumed to be solely due to inverse bremsstrahlung, and radiation loss from the plasma is neglected. The laser intensity remains constant in time, until an approximate steady-state is achieved. The cross-sectional intensity within the beam is also given a square profile.

The equations governing the plasma behaviour will now be presented in section (ii), while section (iii) will deal with the numerical method used for their solution.

(ii) Governing Equations

The condition of quasi-neutrality implies that ions and electrons will have the same number density n, and hence the plasma density is given by:-

$$\rho = n(M + m) \tag{2.1}$$

where M and m are the ion and electron masses. Further, it is assumed that no electric current flows within the plasma, and hence the ions and electrons have a common velocity $\underset{\sim}{v}$.

Equations of Conservation

Conservation of mass is expressed by:-

$$\frac{D\rho}{Dt} + \rho\nabla.\underset{\sim}{v} = 0 \tag{2.2}$$

where $$\frac{D}{Dt} \equiv \frac{\partial}{\partial t} + \underset{\sim}{v}.\nabla$$

Similarly, on neglecting real gas viscous terms in favour of an artificial viscosity to be introduced in the numerical scheme, conservation of momentum is given by:-

$$\rho \frac{D\underset{\sim}{v}}{Dt} + \nabla p = 0 \tag{2.3}$$

where p is the sum of the ion and electron pressures p^+ and p^-. Finally, conservation of energy is expressed by:-

a) for ions

$$\rho\frac{DI^+}{Dt} + p^+ \nabla.\underset{\sim}{v} = \nabla.(\sigma^+\nabla T^+) + E^{+-} \tag{2.4}$$

b) for the electrons

$$\rho\frac{DI^-}{Dt} + p^- \nabla.\underset{\sim}{v} = \nabla.(\sigma^-\nabla T^-) + E^{-+} + W \tag{2.5}$$

where T^+ and T^- are the ion and electron temperatures, I^+ and I^- the ion and electron internal energies per unit mass of plasma, σ^+ and σ^- the ion and electron thermal conductivities, E^{+-} and E^{-+} terms due to energy transfer between species, and W the rate of absorption of laser energy by the free electrons of the plasma.

Taking the ratio of specific heats of each species to be 5/3, the energies and temperatures are related by:-

$$I^{\pm} = \frac{3}{2} k T^{\pm} / (M + m) \qquad (2.6)$$

where k is Boltzmann's constant.

Energy Absorption

Absorption in the underdense plasma is assumed to be entirely due to inverse bremsstrahlung. In a cylindrical geometry with the laser fired along the z-axis, the classical absorption law gives, in the absence of refraction:-

$$\phi(r,z,t) = \phi_{\infty}(r,t)\exp\left[-\int_{z}^{\infty} \alpha(z',t)\,dz'\right] \qquad (2.7)$$

where ϕ is the local laser intensity, ϕ_{∞} is the laser intensity at source and α is the absorption coefficient of the plasma. Dawson and Oberman (1) give:-

$$\alpha = \frac{32\pi^3 Z^2 n^+ n^- e^6 \ln\Lambda}{3cw^2 (2\pi m k T^-)^{\frac{3}{2}}} \cdot \left(1 - \left(\frac{w_p}{w}\right)^2\right)^{-\frac{1}{2}} \qquad (2.8)$$

where e is the electronic charge, c the speed of light, w the laser frequency, Z the average charge of the ions, $\ln\Lambda$ the Coulomb logarithm (in this work Z = 1 and $\ln\Lambda$ = 10 is assumed throughout), and w_p the plasma frequency given by:-

$$w_p^2 = \frac{4\pi n^- e^2}{m} \qquad (2.9)$$

The energy absorption term W in (2.5) can be calculated numerically using (2.7).

Thermal Conductivities

Spitzer (2) gives the electron thermal conductivity as:-

$$\sigma^- = \varepsilon\delta_r 20\left(\frac{2}{\pi}\right)^{\frac{3}{2}} \cdot \frac{(kT^-)^{\frac{5}{2}}k}{m^{\frac{1}{2}}e^4 Z\ln\Lambda} \qquad (2.10)$$

where ε and δ_r depend on Z. (For Z = 1, ε = 0.419 and δ_r = 0.225). A corresponding expression gives the ion thermal conductivity. These of course take no account of flux limitation; a method of modelling the latter will be described in section (iii).

Equilibration

Spitzer (2) shows that the exchange of energy between species is governed by:-

$$\frac{dT^-}{dt} = -\frac{(T^- - T^+)}{t_q} \qquad (2.11)$$

where t_q is the time of equipartition given by:-

$$t_q \doteq \frac{3Mm\ k^{\frac{3}{2}}}{8(2\pi)^{\frac{1}{2}}\ n^+ Z^2 e^4 \ln\Lambda} \cdot \left(\frac{T^+}{M} + \frac{T^-}{m}\right)^{\frac{3}{2}} \qquad (2.12)$$

A numerical method of computing the energy exchange terms E^{-+} and E^{+-}, using (2.11), will be described in section (iii).

Equation of State

Since both species are assumed to be perfect gases, their pressures are given by

$$p^{\pm} = n\ k\ T^{\pm} \qquad (2.13)$$

(iii) Numerical Method

A suitable numerical scheme for solving the above equations must now be found. Since strong shocks and large density gradients are expected, a Lagrangian approach would appear the most suitable. Although this is certainly the case in one dimension, in two or more dimensions Lagrangian schemes become extremely complex, due to grid distortion, and hence an Eulerian approach is used here.

Simple Eulerian schemes such as Lax (3) are unsuitable since, to maintain stability, they include an artificial mass diffusion which, in this problem, would tend to dominate all other processes. Fortunately more sophisticated techniques have been developed. Of particular note are Lax-Wendroff (4), the Fluid in Cell (FLIC) or donor cell method of Gentry, Martin and Daly (5), which is in fact used here, and the Flux-Corrected Transport (FCT) technique of Boris, Book and Hain (6) and (7).

FLIC treats the problem in two stages. Firstly, the momentum and energy equations are solved with an artificial viscosity included but with the transport terms omitted, this being equivalent to allowing the cells to expand and contract in a Lagrangian fashion. Secondly, the missing terms and the continuity equation are accounted for by transport of fluid across the cell boundaries, this being equivalent to interpolating back onto the original grid. The direction of this flow is determined using intermediate velocity values, the rate of transfer being proportional to the density of the cell from which fluid is flowing (the donor cell). Transport of momentum and energy is then determined assuming that the transferred mass carries momentum and energy corresponding to their intermediate values in the donor cell. Finally, updated values of the variables are then obtained from conservation requirements.

FCT is a technique that can be applied to simpler Eulerian schemes (including FLIC). Basically it provides an antidiffusion stage whereby unphysical diffusion due to the finite difference approximation is corrected by an appropriate term, which converts the initially first order (in space) form into an effectively second order scheme. As a result of this correction no artificial viscosity is required to maintain stability or prevent oscillations in the neighbourhood of shocks. Pert (8) has incorporated this technique into a code similar to the one used here and

reports that, apart from a slight sharpening of the variable distributions (due to the fact that the smoothing effects of artificial viscosity can be omitted) it appears to have very little effect when applied to this problem. Hence only the basic FLIC method is used here.

FLIC as presented in ref.(5) only allows for treatment of a simplified form of the energy equation, and modifications to include energy absorption, thermal conduction, and energy transfer between species must be included. These will now be described.

Energy Absorption

At the start of each time step the absorption coefficient α_{ij} at each cell centre in the underdense plasma can be calculated using (2.8). Assuming this to be constant across each cell, (2.7) gives:-

$$\phi_{i-\frac{1}{2},j} = \phi_{i+\frac{1}{2},j} \exp\left[-\alpha_{ij}\Delta z\right] \qquad (2.14)$$

where Δz is the space step size in the z direction, and $\phi_{i+\frac{1}{2},j}$ is the laser intensity at the boundary between cells (i,j) and (i+1,j). The energy per unit mass absorbed by cell (i,j) during timestep Δt is then:-

$$W_{ij} = \frac{\Delta t}{\rho_{ij}\Delta z}\left(\phi_{i+\frac{1}{2},j} - \phi_{i-\frac{1}{2},j}\right) \qquad (2.15)$$

Since the intensity at the extreme right cell boundary is that of the laser source, the energy absorbed by each

cell of the underdense plasma can be calculated iteratively using (2.14) and (2.15).

The non-linear processes that occur in the critical density region are accounted for by a 'dumping' process. When the laser encounters an overdense cell, a fraction β of the energy still available in the beam is absorbed in that cell. The weakened beam is reflected from the cell boundary back into the underdense plasma, absorption calculations being performed as above. Here β is taken to be 0.5.

Thermal Conduction

It is preferable that the energy diffusion equations be treated implicitly, since the explicit treatment of heat conduction problems leads to very restrictive stability conditions. However an implicit scheme such as Crank-Nicholson (see reference (9)), although unconditionally stable, can still lead to restrictions on the time step. This is due to the fact that, in the low density regions of the plasma, the characteristic time of heat flow will be very short, and hence large Δt can produce negative energies. This is avoided here by using, with a slight loss of accuracy the fully implicit scheme of Laasonen (see reference (9)). Positivity is assured since the heat flow out of a cell is entirely dependent upon values at the updated time.

There are two ways of accounting for heat flow in two dimensions. These are the fractional-step and alternating-direction methods (see ref.(9)); however in this case these are almost identical. The two directions are treated separately, thermal conduction in one direction being allowed to operate at double strength for the first half of the time step, the other direction being treated similarly in the latter half. (A new, much superior method has recently been described by Kershaw (10)).

On examining the geometry of a typical cell (i,j) as shown in Figure 2.1, expressions for the heat flow through the cell surfaces can be determined. The heat flux $-\sigma\nabla T$ through the outer surface, in the radial direction, is given by $-\sigma_{j+\frac{1}{2}}(T_{i,j+1} - T_{ij})/\Delta r$, and similarly through the inner surface is $-\sigma_{j-\frac{1}{2}}(T_{ij} - T_{i,j-1})/\Delta r$. Therefore the net heat gained by the cell, due to flow in the radial direction, during time Δt is:-

$$\left[S^r_{j+\frac{1}{2}}\,\sigma_{i,j+\frac{1}{2}}(T_{i,j+1} - T_{ij}) - S^r_{j-\frac{1}{2}}\sigma_{i,j-\frac{1}{2}}(T_{ij} - T_{i,j-1})\right]\frac{\Delta t}{\Delta r} \qquad (2.16)$$

where $S^r_{j+\frac{1}{2}} = 2\pi(j+1)\Delta r\Delta z$

is the area of contact between cells (i,j) and (i,j+1). Similarly the heat gained by the cell due to heat flow in the transverse direction is given by:-

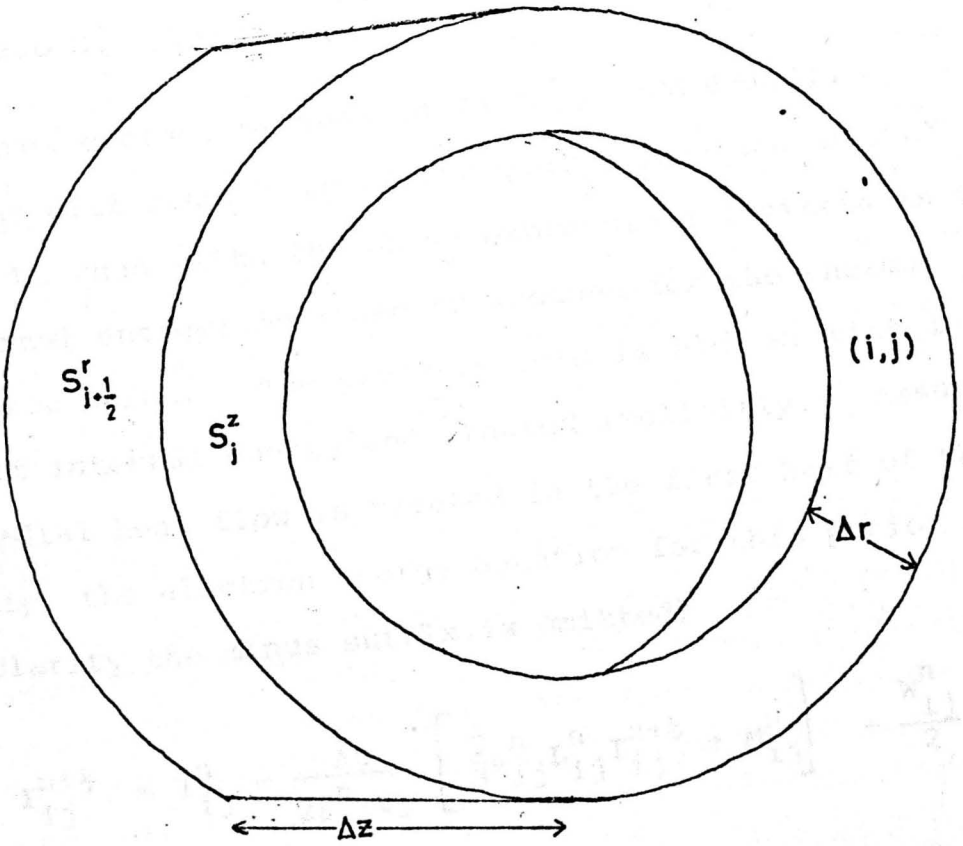

Fig. 2.1

Typical grid cell

$$\left[\sigma_{i+\frac{1}{2},j}(T_{i+1,j} - T_{ij}) - \sigma_{i-\frac{1}{2},j}(T_{ij} - T_{i-1,j})\right] S^z_j \frac{\Delta t}{\Delta z} \quad (2.17)$$

where $S^z_j = 2\pi(j+\frac{1}{2})\Delta r^2$,

is the area contact between cells (i,j) and (i+1,j).

The difference form of the energy equation in FLIC can now be used, with the above expressions (written in terms of internal energy) included to account for the thermal conduction terms. The pressure term is also written in terms of internal energy and treated implicitly. Assuming that radial heat flow is treated in the first half of the timestep, the electron energy equation for this period is:- (For clarity the minus suffix is omitted.)

$$I^{n+\frac{1}{2}}_{ij} = I^n_{ij} - \frac{\Delta t}{2\rho^n_{ij} V_j}\left[\frac{2}{3}\rho^n_{ij} L^n_{ij} I^{n+\frac{1}{2}}_{ij} + M^n_{ij}\right] + \frac{W^n_{ij}}{2}$$

$$+ \frac{2(M+m)}{3\rho^n_{ij} V_j k}\cdot\frac{\Delta t}{\Delta r}\left[S^r_{j+\frac{1}{2}}\sigma^{n+\frac{1}{2}}_{i,j+\frac{1}{2}}\left(I^{n+\frac{1}{2}}_{i,j+1} - I^{n+\frac{1}{2}}_{ij}\right)\right.$$

$$\left. - S^r_{j-\frac{1}{2}}\sigma^{n+\frac{1}{2}}_{i,j-\frac{1}{2}}\left(I^{n+\frac{1}{2}}_{ij} - I^{n+\frac{1}{2}}_{i,j-1}\right)\right] \quad (2.18)$$

where V_j is the volume of cell (i,j), L^n_{ij} is a function of velocities and M^n_{ij} is the artificial viscosity. For each i this can be written in the form:-

$$-A_j I^{n+\frac{1}{2}}_{j+1} + B_j I^{n+\frac{1}{2}}_j - C_j I^{n+\frac{1}{2}}_{j-1} = D^n_j \quad (2.19)$$

This is the well known tridiagonal form and can be solved by a standard method (see ref. (9)). However since the A, B and C terms depend on σ, the solution process should be iterated until a suitable convergence is obtained. In practice the iteration is performed twice, the initial value of the σ's being calculated from temperatures obtained by solving the energy equation assuming no thermal conduction.

In the second half of the timestep heat is allowed to flow in the transverse direction, and hence the energy equation is:-

$$I_{ij}^{n+1} = I_{ij}^{n+\frac{1}{2}} - \frac{\Delta t}{2\rho_{ij}^{n} V_j}\left[\frac{2}{3}\rho_{ij}^{n} I_{ij}^{n+1} + M_{ij}^{n}\right] + \frac{W_{ij}^{n}}{2}$$

$$+ \frac{2(M+m)}{3\rho_{ij}^{n} V_j k \Delta z}\frac{\Delta t S_j^{z}}{}\left[\sigma_{i+\frac{1}{2},j}^{n+1}\left(I_{i+1,j}^{n+1} - I_{ij}^{n+1}\right)\right.$$

$$\left. - \sigma_{i-\frac{1}{2},j}^{n+1}\left(I_{ij}^{n+1} - I_{i-1,j}^{n+1}\right)\right] \qquad (2.20)$$

For each j this can again be written in the tridiagonal form and treated as above. The ion energy equation is treated in a similar manner.

The above takes no account of energy transfer between species. This is accomplished in a separate stage, which will be described later. Firstly the possibility of including flux limitation in the above integration will be examined.

Flux Limitation

In the derivation of the expression for electron thermal conductivity (2.10), it is assumed that:-

$$\lambda_e \nabla \bar{T} \ll \bar{T} \tag{2.21}$$

where λ_e is the electron-electron mean free path. When (2.21) is not satisfied, unrealistically large heat fluxes will be predicted and it is obvious that some kind of flux limiting process must operate within the plasma. Various processes that produce such a limit have been suggested (see Chapter 3 sec VIII) but since it is not yet clear which of these, if any, is dominant, it is necessary to appeal to experiment. Since the maximum possible heat flux is given by the product of random particle flux and their mean thermal energy, the limiting flux for electron conduction is assumed to be of the form:-

$$Q_{max} = f \frac{n\bar{c}}{4} \left(\frac{3}{2} k\bar{T}\right) = f\, nk\, \bar{T} (k\bar{T}/m)^{\frac{1}{2}} \tag{2.22}$$

where $\bar{c}$ is the mean electron velocity and f is a dimensionless number characterising the flux limiting process.

Since for $\lambda_e \nabla \bar{T} \ll \bar{T}$ the heat flux is $-\sigma \nabla \bar{T}$, and for $\lambda_e \nabla \bar{T} \gg \bar{T}$ it is Q_{max}, this suggests taking, for numerical purposes, a heat flux of the form $-\sigma' \nabla \bar{T}$, where:-

$$\sigma' = \sigma / \left[1 + \lambda' |\nabla \bar{T}| / \bar{T}\right] \tag{2.23}$$

Here λ' must be chosen to give the desired expression for Q_{max} in the limit. As $\nabla T^-/T^-$ becomes large:-

$$\sigma' \nabla T^- \simeq \sigma^- T^- \nabla T^- / |\nabla T^-| \lambda' = Q_{max} \frac{\nabla T^-}{|\nabla T^-|}$$

$$\text{hence } \lambda' = \sigma^- T^- / Q_{max} = \sigma^- / f\ nk(kT^-/m)^{\frac{1}{2}} \qquad (2.24)$$

Therefore σ' can be substituted for σ^- in the energy integration, to give an adequate model of flux limitation.

Equilibration

The first stage integration of the energy equation is performed assuming that there is no heat exchange between species. This omission is rectified in a separate stage. For this purpose it is assumed that heat is absorbed at the beginning of the time step and energy exchange then proceeds for a time Δt as if no more heat is absorbed. By this means, equilibration is reduced to a simple adjustment of the internal energy values already obtained.

Writing (2.11) in terms of internal energy and integrating, with the assumption that energy is conserved during the exchange, gives:-

$$(I^- - I^+)_* = (I^- - I^+)_o \exp\left[-2\Delta t/t_q\right] \qquad (2.26)$$

where it is assumed that t_q is constant throughout the time step, and o and $*$ refer to values before and after heat

exchange respectively. Conservation of energy gives:-

$$I_*^- - I_o^- = I_o^+ - I_*^+ \tag{2.27}$$

and hence:-

$$2I_*^{\pm} = I_o^- + I_o^+ \pm (I_o^- - I_o^+) \exp\left[-2\Delta t/t_q\right] \tag{2.28}$$

Taking I_o^- and I_o^+ to be values obtained after the first stage integration, adjusted energy values can be easily calculated using (2.28).

A similar treatment to the above has been described by Christiansen and Roberts (11).

Stability and Accuracy

A brief stability analysis of FLIC is given in ref.(5), and a slightly different approach to the problem is given by Hirt (12). It is recommended that, to ensure an accurate solution, the time step be restricted to satisfy

$$\left.\begin{aligned} v_r \Delta t &< 0.4 \Delta r \\ \text{and} \qquad v_z \Delta t &< 0.4 \Delta z \end{aligned}\right\} \tag{2.29}$$

where v_r and v_z are the components of $\underset{\sim}{v}$. In addition, to ensure stability, the Courant-Levy-Friedrichs condition

must be satisfied i.e.

$$C_s \Delta t < \gamma \Delta x \qquad (2.30)$$

where C_s is the local sound speed, Δx is the minimum of Δr and Δz, and γ is a number, less than one, that must be determined by trial and error. A value of $\gamma = 0.5$ was found to be suitable. To avoid unphysical behaviour, it was also found advisable to restrict the energy absorbed by any cell during one timestep, to a fraction α of the energy already contained in that cell i.e.

$$W_{ij} < \alpha I_{ij}$$

where $I_{ij} = I^-_{ij} + I^+_{ij}$, this being accomplished by again restricting the timestep. $\alpha = 0.1$ was found to be suitable.

It was found that the rather artificial conditions that exist in regions of large density gradient could occasionally produce velocities high enough to drive the density negative. Since this only occurred in the relatively unimportant cells at the edge of the expanding plasma, it was felt justifiable to maintain positivity by simply reducing the high velocities to the maximum allowed by (2.29).

Initial and Boundary Conditions

Initially the number density n_s of the target was set at 5×10^{22}/cc. The density assigned to the vacuum n_v must be chosen so that the initial density gradient is not too extreme, and was here taken to be 5×10^{16}/cc. These were connected by a six-cell transition region, having a density profile of the form:-

$$n = n_v + (n_s - n_v)\exp(-z'/l) \qquad (2.31)$$

where z' is measured from the target edge, and l is a scaling factor, here taken as $\Delta z/2$. Both ion and electron temperatures were initially set at 300^{o}K, and of course initial velocities were taken as zero.

Due to the cylindrical geometry there is no real boundary at r = 0, and on the remaining three boundaries the space derivatives normal to the boundary of all variables were set at zero for all time. To prevent heat being conducted into the vacuum, the thermal conductivity at the plasma-vacuum interface was similarly always set to zero.

To reduce the computing time, the boundary $z = z_{max}$ was allowed to move a few cells ahead of the expanding plasma, until the maximum grid size was reached.

Space and Time Steps

Since a fixed number of cells is always used, the space step sizes must be varied to suit the case under consideration. The radius of laser beam is normally taken to cover four cells (this is reduced for the higher laser intensities) and hence the value of Δr is automatically fixed by the beam width. Δz must be chosen, by trial and error, to allow the plasma sufficient room to expand. The long physical times required tend to lead to somewhat large values of Δz; this problem will be discussed further in Chapter 4.

The possibility of allowing Δz to vary with the plasma dimensions was at first considered but rejected, since this is equivalent to forcing the grid to move through the fluid in a non-uniform fashion, and hence requires the use of a rezoning technique. A method that includes the possibility of rezoning has been described by Hirt et al (13). However this kind of technique is fraught with difficulties due to the ease with which errors and instabilities can arise, and is really to be used only when absolutely necessary. Its use is not justified in this case.

Initially Δt is set at 10^{-12} sec, and then allowed to vary continuously, taking the maximum value allowed by the stability conditions.

CHAPTER 3

Laser-Target Models

(i) Introduction

This section is intended as a brief history and description of the various models proposed for laser-target interactions. These models, and the results that are of interest here, will be discussed more fully in the following sections.

The groundwork of the theory was laid by Dawson (1), Basov and Krokhin (2), and Caruso and Gratton (3); from this, the self regulating (S-R) model was developed, apparently independently, by Krokhin et al (4),(5),(6) and (7) and Caruso et al (8) and (9).

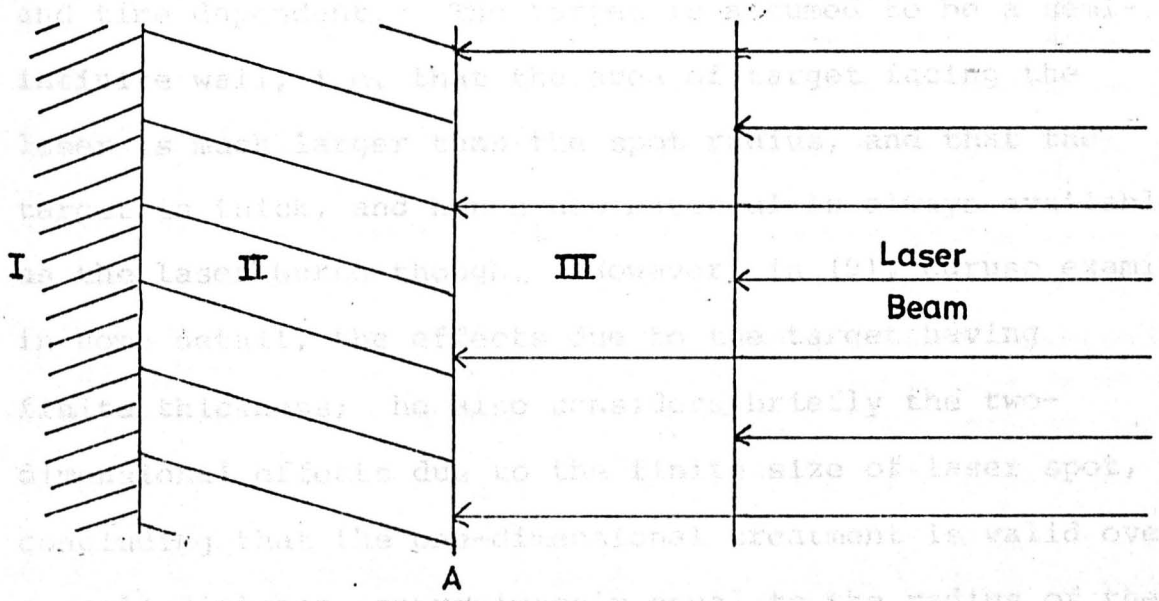

Figure (3.1)

The model assumes three distinct regions in the target material (see Fig. (3.1)). Region I is the undisturbed target, region II is dense matter heated by a shock wave travelling back into the target, while region III consists of low density plasma, burnt away at surface A and expanding out into vacuum. It is assumed that laser energy is absorbed in region III via inverse bremsstrahlung, most of this going into a very thin layer in the region of surface A, which being strongly heated continually produces more plasma to augment region III. The name of the model derives from the assumption that this production of plasma is regulated automatically by region III. i.e. If region III tends towards opacity less plasma will be produced at A and hence the density of region III will decrease leading towards transparency. Alternatively, if region III tends towards transparency the process will be reversed.

The model, in its initial form, is one-dimensional and time dependent. The target is assumed to be a semi-infinite wall, i.e. that the area of target facing the laser is much larger than the spot radius, and that the target is thick, and hence new material is always available as the laser burns though. However, in (9), Caruso examines, in some detail, the effects due to the target having finite thickness; he also considers briefly the two-dimensional effects due to the finite size of laser spot, concluding that the one-dimensional treatment is valid over a small distance, approximately equal to the radius of the spot, in front of the target. Using this result, Puell (10) produced a steady-state treatment of the S-R model, still

assuming a region of one-dimensional behaviour, but also estimating effects due to the two dimensional expansion of the plasma.

It had been deduced (9) that the S-R model is suitable for relatively low laser intensities (10^{16} - 10^{21} cgs, in the case of ruby or glass lasers). To accommodate higher fluxes, Fauquignon and Floux (11) developed the deflagration-wave (D-W) model. This was later given a more detailed treatement by Bobin (12) using the radiation-front theory of Fraser (13). This model, see fig. (3.2), assumes that all of the laser energy is absorbed

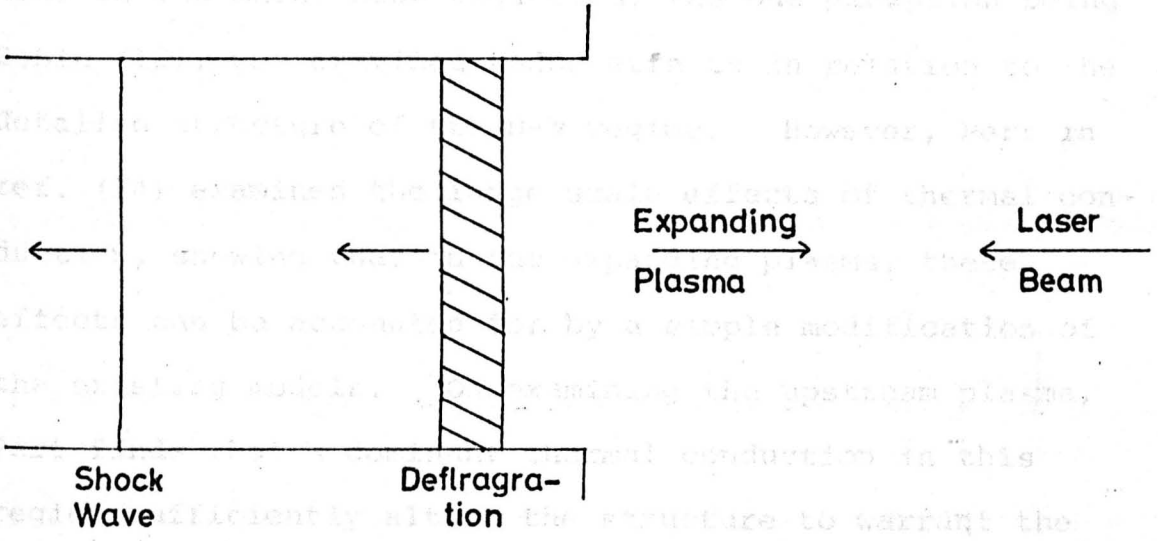

Figure (3.2)

by an unspecified mechanism, in a narrow region at density of the order of the critical density. This region, the deflagration, becomes heated and attains a high pressure that drives a shock wave into the solid target, producing cold high density plasma. At the same time a hot tenuous plasma

is formed that expands out towards the laser. The treatment is one dimensional, and it is assumed that the postulated structure is instantaneously produced at time t = 0, hence treating the problem as one of steady state.

However, Puell (10) has demonstrated how the D-W model arises as a natural consequence of the S-R model, with inverse bremsstrahlung absorption, and thus that the two models can be considered to be two different regimes of the same fundamental model, separated by a reasonably well-defined condition.

Up to this point, the effects of thermal conduction had, in the main, been neglected, the one exception being Bobin (12), who examined these effects in relation to the detailed structure of the D-W regime. However, Pert in ref. (14) examines the large scale effects of thermal conduction, showing that in the expanding plasma, these effects can be accounted for by a simple modification of the existing models. On examining the upstream plasma, Pert finds that a dominant thermal conduction in this region sufficiently alters the structure to warrant the introduction of two new regimes, namely the thick S-R and thick D-W regimes. Effects due to flux limitation, which could be of some importance, are however neglected.

It should be pointed out that none of the above models take account of any time variation of the laser pulse, it being assumed that the laser attains it maximum intensity instantaneously at time t = 0, and continues at a constant

power until the steady-state is attained. Also, in the case of two-dimensional models it is assumed that there is no space variation in intensity across the laser beam.

The steady state models, with the modifications due to Pert, will now be described in more detail. However first it is necessary to examine the properties of a one-dimensional deflagration.

(ii) The Deflagration

Consider flow through a stationary, one dimensional deflagration (see Fig. 3.3) where suffices 1 and 2 refer to parameters on the upstream and downstream boundaries respectively. From the conservation conditions across the deflagration (see e.g. Landau and Lifshitz (15)) and assuming $\rho_1 >> \rho_2$ and that the deflagration is strong i.e. $h_2 >> h_1$ where h is specific enthalpy, one obtains:-

$$\left.\begin{aligned} \rho_1 v_1 &= \rho_2 v_2 = J \\ p_1 &= p_2 + \rho_2 v_2^2 \\ \frac{\phi}{J} &= h_2 + \tfrac{1}{2} v_2^2 \end{aligned}\right\} \qquad (3.1)$$

Assuming that the downstream velocity v_2 is the adiabatic sound speed (Chapman-Jouget condition):-

$$v_2 = \sqrt{\frac{\gamma p_2}{\rho_2}} \qquad (3.2)$$

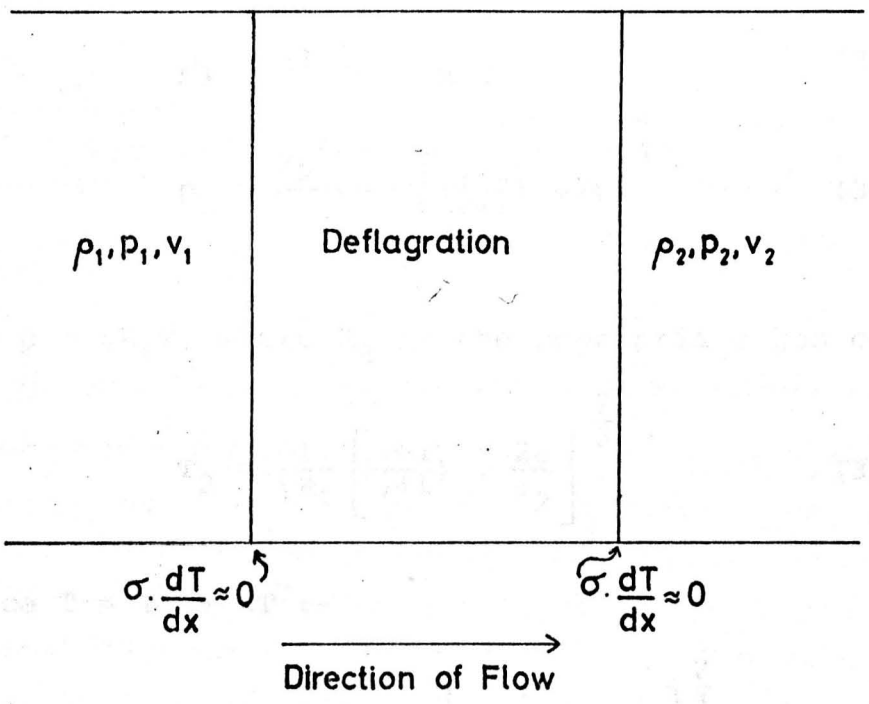

Fig. 3.3

One-dimensional deflagration

where γ is the ratio of the specific heats, assumed constant (polytropic gas), and with $h = \gamma p/(\gamma-1)\rho$, (3.1) gives the following:-

$$p_1 = (1 + \gamma)p_2 \tag{3.3}$$

$$p_2 = \frac{\rho_2^{1/3}}{\gamma} \cdot \left[\left(\frac{\gamma-1}{\gamma+1}\right) .2\phi\right]^{\frac{2}{3}} \tag{3.4}$$

Putting $p = \rho R_g T$, where R_g is the appropriate gas constant:-

$$T_2 = \frac{1}{\gamma R_g} \cdot \left[\left(\frac{\gamma-1}{\gamma+1}\right) . \frac{2\phi}{\rho_2}\right]^{\frac{2}{3}} \tag{3.5}$$

and since $T = T^+ + ZT^-$:-

$$T_2^- = \frac{1}{\gamma \xi Z R_g} \cdot \left[\left(\frac{\gamma-1}{\gamma+1}\right) . \frac{2\phi}{\rho_2}\right]^{\frac{2}{3}} \tag{3.6}$$

where $\xi = 1 + T^+/ZT^-$.

Similarly when v_2 is the isothermal sound speed:-

$$v_2 = \sqrt{\frac{p_2}{\rho_2}} \tag{3.7}$$

one obtains

$$p_1 = 2p_2 \tag{3.8}$$

$$p_2 = \rho_2^{\frac{1}{3}} \cdot \left[\frac{2(\gamma-1)}{(3\gamma-1)} .\phi\right]^{\frac{2}{3}} \tag{3.9}$$

$$T_2 = \frac{1}{R_g} \cdot \left[\frac{2(\gamma-1)}{(3\gamma-1)} \cdot \frac{\phi}{\rho_2} \right]^{\frac{2}{3}} \qquad (3.10)$$

$$T_2^- = \frac{1}{\xi Z R_g} \cdot \left[\frac{2(\gamma-1)}{(\beta\gamma-1)} \cdot \frac{\phi}{\rho_2} \right]^{\frac{2}{3}} \qquad (3.11)$$

(iii) The Deflagration-Wave Regime

This regime is characterised by the absorption of the majority of the laser energy at the critical density, with only a small fraction $(1 - \beta)$ absorbed in the expansion fan. The region of absorption is assumed to be a one-dimensional deflagration. Bobin (12), in a detailed study of the deflagration structure, has shown that if the temperature increases monotonically across the deflagration, the exit flow speed v_2 will be the isothermal sound speed. However Pert (14) shows that due to heat conduction, the effective deflagration will be a region around the critical density surface, with a temperature maximum at the latter. Hence Bobin's theory cannot be directly applied. A solution to this problem will be dealt with shortly; however first it is necessary to differentiate between the two modes of expansion.

Pert shows that if thermal conduction is dominant in the expansion fan, the expansion will be isothermal. Since the scale length of the expansion is of the order of magnitude of the spot radius R_o, this dominance can be formalised as:-

$$L \gtrsim R_o \qquad (3.12)$$

where L is the thermal conduction length i.e. the scale length over which the conduction energy flux is comparable with the convection flux, which Pert gives as:-

$$L = 2 \times 10^{15} A^{\frac{1}{2}} (T^-)^2 (\xi Z)^{-\frac{3}{2}} / n^- \ln \Lambda \text{ cm} \qquad (3.13)$$

If (3.12) is not true in the expansion fan, the expansion will be adiabatic.

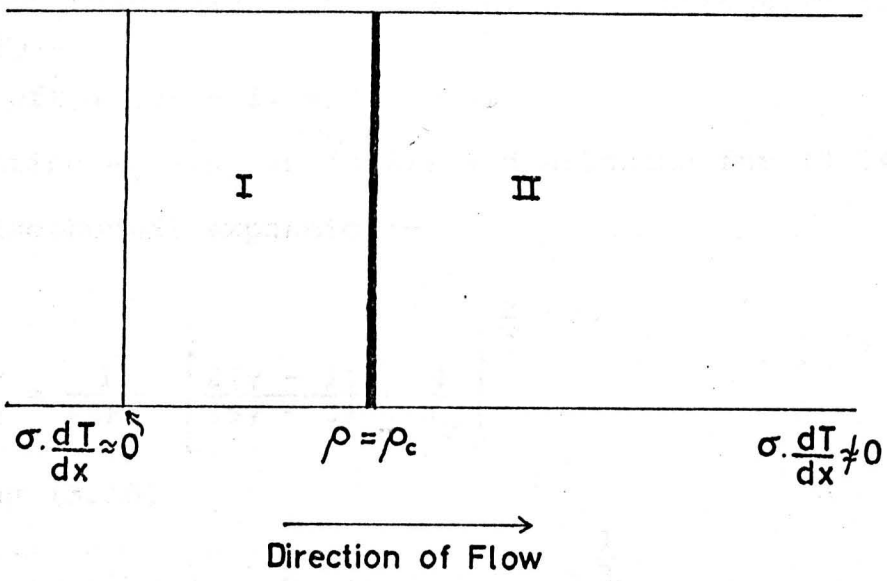

Figure 3.4

In the case of an isothermal expansion the right hand boundary of the deflagration is effectively at infinity (see Fig. 3.4). However since there is a temperature maximum at the critical density surface, this surface satisfies the end-point conditions for a deflagration, and hence regions I and II can be treated seperately. It would seem reasonable to assume that the temperature rises monotonicaley across region I, and hence applying Bobin's theory to this region shows that the velocity at $\rho = \rho_c$ is the isothermal sound speed. Equations

(3.9) - (3.11) will therefore be true for region I with the proviso that a reduced laser intensity is used, to account for energy lost by conduction into region II. Since region II represents the isothermal expansion fan, Pert shows that the absorbed energy conducted downstream from the critical density is given by $\rho v R_g (T^+ + ZT^-) = \rho_c (R_g T_2)^{\frac{3}{2}}$, and on examining (3.10) it is seen that this is equivalent to an effective laser intensity:-

$$\phi \text{ eff} = (3\gamma - 1)\,\phi/(5\gamma - 3) \qquad (3.14)$$

Putting $\rho_2 = \rho_c$ in (3.11) and allowing for (3.14) gives, for an isothermal expansion:-

$$T_2^- = \frac{1}{\xi Z R_g} \left[\frac{2(\gamma - 1)}{(5\gamma - 3)} \cdot \frac{\phi}{\rho_c} \right]^{\frac{2}{3}} \qquad (3.15)$$

and using (3.15)

$$v_2 = \sqrt{R_g T_2} = \left[\frac{2(\gamma - 1)}{(5\gamma - 3)} \cdot \frac{\phi}{\rho_c} \right]^{\frac{1}{3}} \qquad (3.16)$$

In the case of an adiabatic expansion the situation will be as shown in Fig. 3.5. Bobin's theory can again be applied to region I, and in region II the flow velocity will change from the isothermal sound speed at $\rho = \rho_c$, to the adiabatic sound speed at the downstream end of the deflagration. Hence equations (3.3) - (3.6) will apply for the whole deflagration. The appropriate value of ϕ is now the total laser intensity reduced by a small fraction $(1 - \beta)$ to account for absorption in the expansion fan. Since the deflagration is assumed to be one-dimensional the outgoing flux will equal the flux at the critical

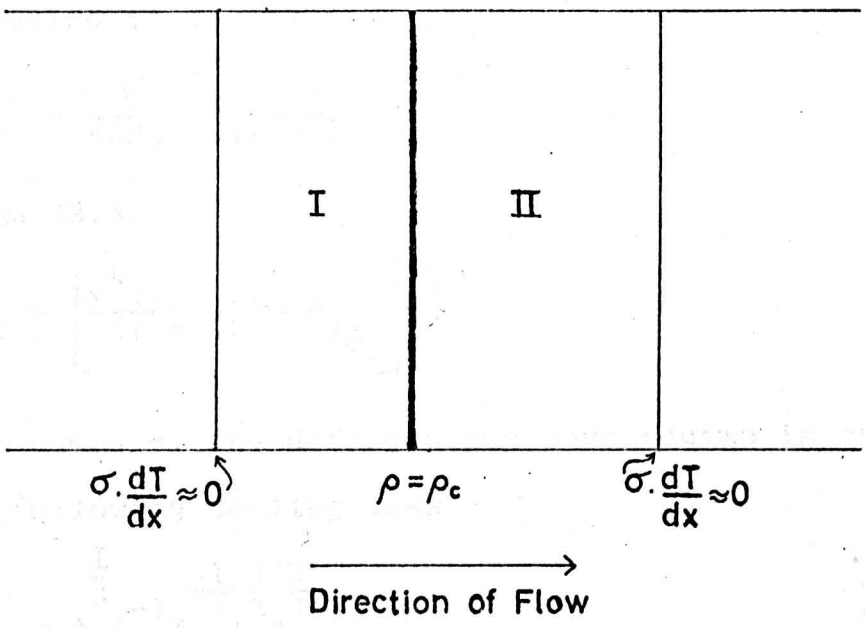

Fig. 3.5

Structure of deflagration in an adiabatic expansion

density, and hence it can be shown that the downstream density is given by:-

$$\rho_2 = \rho_c \gamma^{-\frac{1}{2}} \tag{3.17}$$

Substituting in (3.16) then gives

$$T_2^- = \frac{1}{\xi Z R_g} \left[\frac{(\gamma - 1)}{\gamma(\gamma + 1)} \cdot \frac{2\beta\phi}{\rho_c} \right]^{\frac{2}{3}} \tag{3.18}$$

and from (3.5)

$$v_2 = \left[\frac{\gamma^{\frac{1}{2}}(\gamma - 1)}{(\gamma + 1)} \cdot \frac{2\beta\phi}{\rho_c} \right]^{\frac{1}{3}} \tag{3.19}$$

In summary, the deflagration wave regime is characterised by the following scaling laws:-

$$\left.\begin{aligned} T_2^- &\alpha\ A^{\frac{1}{3}} \xi^{-1} Z^{-\frac{1}{3}} \lambda^{\frac{4}{3}} \phi^{\frac{2}{3}} \\ v_2 &\alpha\ A^{-\frac{2}{3}} Z^{\frac{2}{3}} \lambda^{\frac{2}{3}} \phi^{\frac{1}{3}} \end{aligned}\right\} \tag{3.20}$$

where λ is the laser wavelength and A is the ion mass number.

(iv) Self-Regulating Regime

As previously mentioned, this regime is characterised by the existence of a region of one dimensional flow, approximately equal in length to the spot radius, merging into a three dimensional expansion fan. Only a small fraction $(1 - \beta)$ of the laser energy is absorbed in the expansion fan, the majority being absorbed in the one-dimensional flow zone. In addition the latter region obeys the self-regulating condition i.e. its optical depth is constant and approximately equal to unity.

If the region of one-dimensional flow is now identified with the deflagration, similiar arguments to those used in section (iii) can be applied. However since the main region of absorption is no longer localised, there is no clearly defined temperature maximum in this case. However Puell (10) shows that the temperature will rise monotonically through the one-dimensional region, reaching a maximum at the downstream end. He also shows that the density at this surface is given approximately by:-

$$\rho_R = (kT_R^-)^{\frac{3}{4}} \left(\frac{2}{5CZR_o}\right)^{\frac{1}{2}} M/Z \qquad (3.21)$$

where R_o is the spot radius and:-

$$C \approx 2.5 \times 10^{-55} \left(\frac{\lambda}{0.69}\right)^2 \quad \text{c.g.s units} \qquad (3.22)$$

where λ is the laser wavelength in μm. In deriving (3.21) Puell does in fact assume an adiabatic expansion. However since the calculation is very approximate, it would seem justifiable to put $\rho_2 = \rho_R$ with $T_R^- = T_2^-$ for both modes of expansion. Hence, since the flow velocity at the temperature maximum should still be the isothermal sound speed, by substituting $\rho_2 = \rho_R$ in (3.11) and again using (3.14) to account for heat conduction to the expansion fan, we obtain, for an isothermal expansion:-

$$kT_2^- = (5CMR_o/2)^{\frac{2}{9}} \left[\frac{2(\gamma - 1)}{(5\gamma - 3)} \cdot \phi\right]^{\frac{4}{9}} \xi^{-\frac{2}{3}} \qquad (3.23)$$

Hence:-

$$V_2 = \left(\frac{kT_2}{M}\right)^{\frac{1}{2}} = \left(\frac{\xi Z k T_2^{-}}{M}\right)^{\frac{1}{2}} = (5CR_o/2)^{\frac{1}{9}} \left[\frac{2(\gamma - 1)}{(5\gamma - 3)} \cdot \phi\right]^{\frac{2}{9}} \xi^{\frac{1}{6}} M^{-\frac{7}{18}} \qquad (3.24)$$

and:-

$$\rho_2 = \left[\frac{2}{5CR_o} \cdot \frac{2(\gamma - 1)}{(5\gamma - 3)} \cdot \phi\right]^{\frac{1}{3}} \xi^{-\frac{1}{2}} Z^{-\frac{3}{2}} M^{\frac{7}{6}} \qquad (3.25)$$

In the case of an adiabatic expansion, there must be a short region downstream from the temperature maximum over which the flow velocity changes to the adiabatic sound speed. Hence, substituting $\rho_2 = \rho_R$ in (3.6), and allowing for the fraction β of energy absorbed in the expansion fan, we obtain:-

$$kT_2^{-} = (5CMR_o/2)^{\frac{2}{9}} \left[\frac{2(\gamma - 1)}{(\gamma + 1)} \cdot \beta\phi\right]^{\frac{4}{9}} (\xi\gamma)^{-\frac{2}{3}} \qquad (3.26)$$

which, on putting $\gamma = \frac{5}{3}$ and $\beta = \frac{2}{3}$ gives the expression obtained by Puell (10). Expressions for velocity and density, simila r to (3.24) and (3.25), can be derived from (3.26).

In summary, the self-regulating regime is characterised by the following scaling laws:-

$$\left.\begin{aligned} T_2^{-} &\propto A^{\frac{2}{9}} \xi^{-\frac{2}{3}} \lambda^{\frac{4}{9}} R_o^{\frac{2}{9}} \phi^{\frac{4}{9}} \\ V_2 &\propto A^{-\frac{7}{18}} \xi^{\frac{1}{6}} \lambda^{\frac{2}{9}} R_o^{\frac{1}{9}} \phi^{\frac{2}{9}} \\ \rho_2 &\propto A^{\frac{7}{6}} \xi^{-\frac{1}{2}} Z^{-\frac{3}{2}} \lambda^{-\frac{2}{3}} R_o^{-\frac{1}{3}} \phi^{\frac{1}{3}} \end{aligned}\right\} \qquad (3.27)$$

(v) D - W and S - R Regime Boundary

The results of section (iv) will normally be true for low powered laser. However equation (3.25) shows that as ϕ increases

ρ_2 will increase and will eventually be equal to ρ_c. Any further increase in ϕ must then be explained in terms of the deflagration-wave regime, using the results of section (iii). Hence, in the isothermal case, putting $\rho_2 = \rho_c$ in (3.25) gives the regime boundary:-

$$\phi = \frac{5CR_o}{2} \cdot \frac{(5\gamma - 3)}{2(\gamma - 1)} \cdot \xi^{\frac{3}{2}} Z^{\frac{9}{2}} M^{-\frac{7}{2}} \rho_c^{\,3} \qquad (3.28)$$

which can be written as:

$$\phi = DR_o \xi^{\frac{3}{2}} Z^{\frac{3}{2}} A^{-\frac{1}{2}} \lambda^{-4} \qquad (3.29)$$

where D is a constant. In c.g.s units with $\gamma = \frac{5}{3}$, D has a value 4×10^{21} (λ is measured in μm). In the adiabatic case, a simila r argument again yields (3.29), with $D = 6.5 \times 10^{21}$.

(vi) Thick Regimes

It has been seen how a dominant thermal conduction in the downstream plasma can be accounted for by a minor modification of the basic models. However, when $L >> R_o$ is also true in the upstream plasma, Pert (14) shows that the flow structure becomes markedly different, and warrants the introduction of two new regimes. These are known as the 'thick' regimes, those previously discussed being now referred to as 'thin'.

Due to rapid heat conduction, the effective heating zone will penetrate a distance $\sim L$ upstream. However, more importantly, by the same process, the heating zone will be spread radially over an area $\sim L^2$. Hence Pert proposes that when $L >> R_o$, the flow will behave as for a laser of radius L with intensity:-

$$\phi \approx P/L^2 \qquad (3.30)$$

where P is the laser power.

Substituting (3.30) in (3.15) and using (3.13) gives, for the thick deflagration regime, the following scaling laws:-

$$\bar{T}_2 \alpha A^{-\frac{1}{11}} \xi^{\frac{3}{11}} Z^{\frac{5}{11}} \lambda^{-\frac{4}{11}} P^{\frac{2}{11}} \qquad (3.31)$$

and

$$v_2 \alpha \left(\frac{Z \xi \bar{T}}{A} \right)^{\frac{1}{2}} \qquad (3.32)$$

In the case of the self-regulating regime it is to be expected that when $L >> R_o$, the plasma dimensions will be of the order L. Hence, substituting (3.30) in (3.23), and replacing R_o by L, gives, for the thick self-regulating regime:-

$$\bar{T}_2 \alpha A^{-\frac{1}{6}} \xi^{\frac{1}{2}} Z^{\frac{1}{2}} \lambda^{-\frac{1}{3}} P^{\frac{1}{6}} \qquad (3.33)$$

and from (3.25):-

$$\rho_2 \alpha A^{\frac{7}{12}} \xi^{\frac{5}{4}} Z^{-\frac{3}{4}} \lambda^{-\frac{11}{6}} P^{-\frac{1}{12}} \qquad (3.34)$$

Of particular note is the very weak scaling, with respect to laser power, implied by the above results.

(vii) Regime Diagram

The boundary between thin and thick regimes is now defined to be $L = R_o$. Hence using (3.13) and (3.15) one obtains, for the deflagration-wave thin-thick boundary:-

$$R_o = 1.13 \times 10^{-28} A^{\frac{7}{6}} \xi^{-\frac{7}{2}} Z^{-\frac{13}{6}} \lambda^{\frac{14}{3}} \phi^{\frac{14}{3}} / \ln \Lambda \qquad (3.35)$$

Similarly the self-regulating thin-thick boundary is given by:-

$$R_o^{\frac{2}{9}} = 6.6. \times 10^{-12} A^{\frac{7}{9}} \xi^{-\frac{7}{3}} Z^{-1} \lambda^{\frac{14}{9}} \phi^{\frac{5}{9}} / \ln \Lambda \qquad (3.36)$$

Both of these expressions are in c.g.s. units with λ in μm. Finally, since the total energy convection through the critical density surface is a constant, the boundary between thick self-regulating and thick deflagration-wave regimes is given by:-

$$\phi R_o^2 = \text{constant} \qquad (3.37)$$

The above equations, along with (3.28), may be plotted to obtain a regime diagram for any particular case. However, by putting

$$\left.\begin{aligned} I &= A^2\lambda^2 Z^{-2}\xi^{-6}\phi \\ \text{and} \qquad \mathcal{R} &= A^{\frac{3}{2}}\lambda^{-2} Z^{-\frac{1}{2}}\xi^{-\frac{9}{2}}R_o \end{aligned}\right\} \qquad (3.38)$$

equations (3.28), (3.35) and (3.36) become:-

$$\left.\begin{aligned} I &= \begin{Bmatrix} 6.5 \times 10^{21} \\ 4.0 \times 10^{21} \end{Bmatrix} \mathcal{R} \\ \mathcal{R} &= 1.13 \times 10^{-28} I^{\frac{4}{3}} / \ln \Lambda \\ \mathcal{R}^{\frac{2}{9}} &= 6.6 \times 10^{-12} I^{\frac{5}{9}} / \ln \Lambda \end{aligned}\right\} \qquad (3.39)$$

The above may be plotted to obtain the universal regime diagram shown in Fig. 3.6. ($\ln \Lambda$ is assumed to be constant and equal to 5).

It is interesting to note that using the transformation (3.38) and by putting:-

$$\left.\begin{aligned} \mathcal{T} &= \xi^{-3} A Z^{-1} T_2 \\ \mathcal{N} &= n_2 \lambda^2 \\ \text{and} \qquad \mathcal{P} &= I \mathcal{R}^2 \end{aligned}\right\} \qquad (3.40)$$

the scaling laws for each regime can be written in a very concise form thus:-

Thin S - R

$$\left.\begin{aligned} \mathcal{N} &\propto \mathcal{R}^{-\frac{1}{3}} I^{\frac{1}{3}} \\ \mathcal{T} &\propto \mathcal{R}^{\frac{2}{9}} I^{\frac{4}{9}} \end{aligned}\right\} \qquad (3.41)$$

$R_o = 100\,cm.$ (see fig. 4.26)

$R_o = 10^{-3}\,cm.$ (see fig. 4.23)

Ruby Laser, H- Target, $Z = 1$, $\xi = 2$.

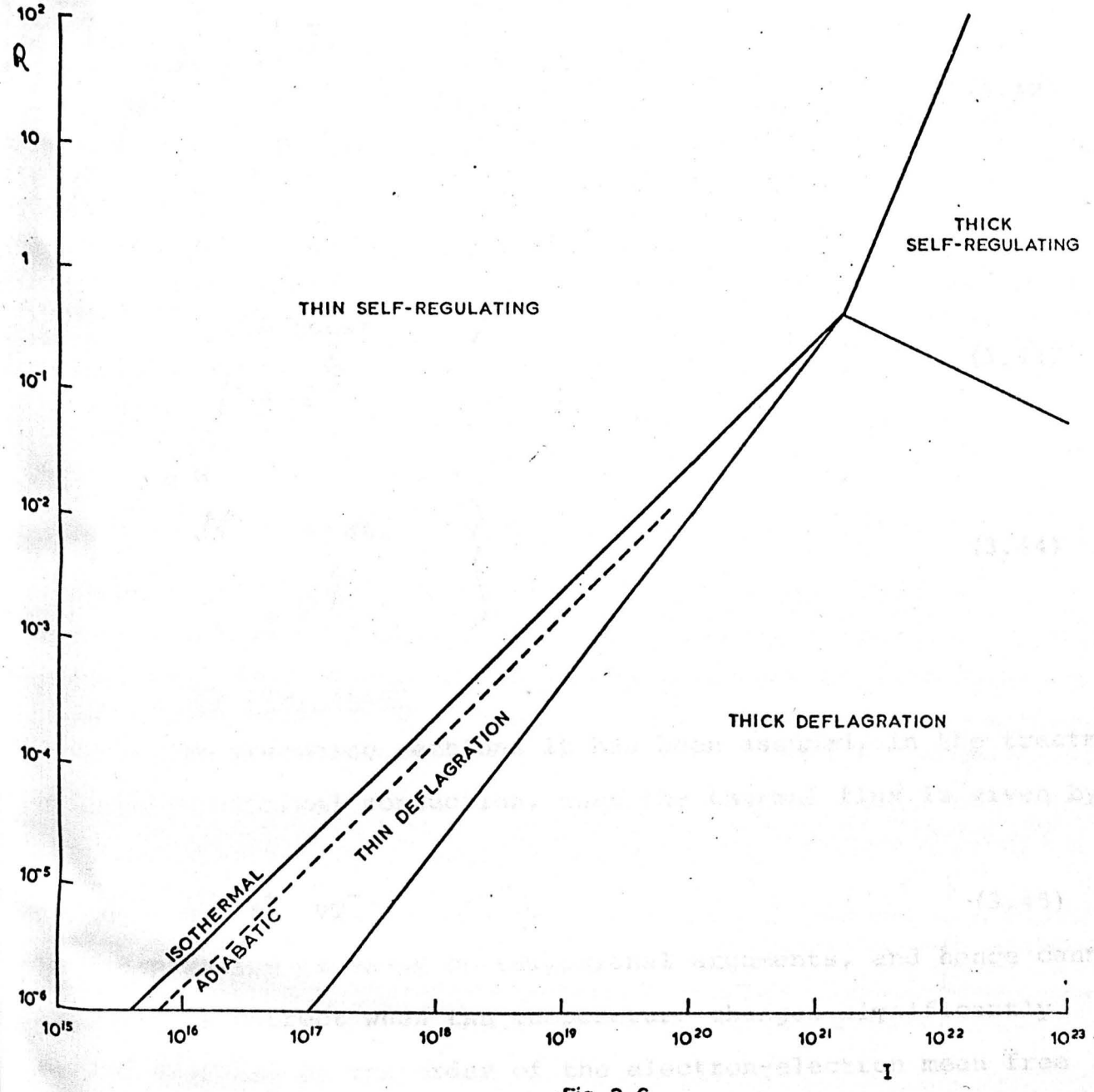

Fig. 3.6

Universal regime diagram

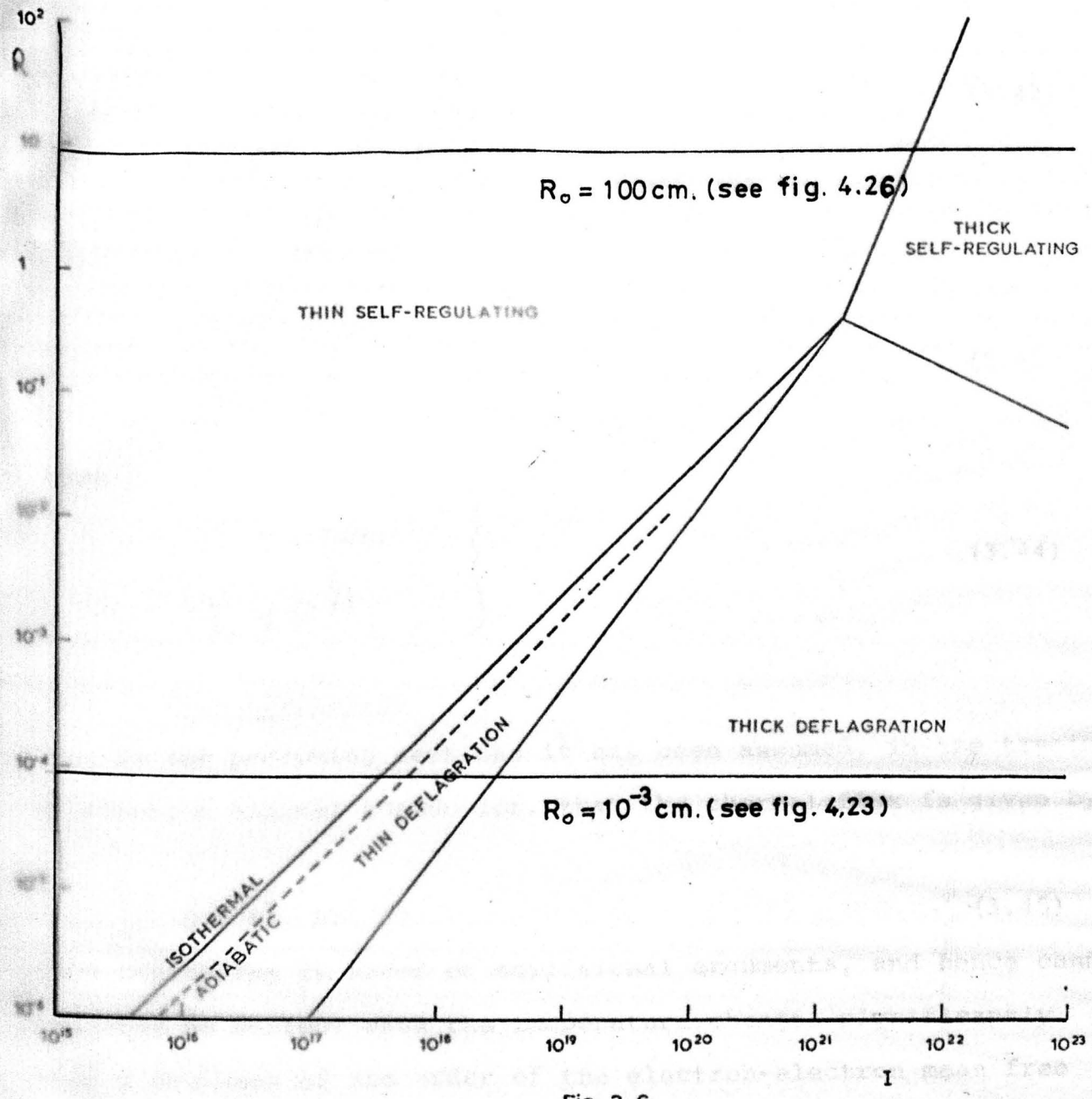

Fig. 3.6

Universal regime diagram

Ruby Laser, H- Target, Z = 1, ξ = 2.

Thick S - R

$$\left.\begin{aligned} \mathcal{N} &\propto \rho^{-\frac{1}{12}} \\ \mathcal{T} &\propto \rho^{\frac{1}{6}} \end{aligned}\right\} \qquad (3.42)$$

Thin D - W

$$\left.\begin{aligned} \mathcal{N} &= \text{const} \\ \mathcal{T} &\propto I^{\frac{2}{3}} \end{aligned}\right\} \qquad (3.43)$$

Thick D - W

$$\left.\begin{aligned} \mathcal{N} &= \text{const.} \\ \mathcal{T} &\propto \rho^{\frac{2}{11}} \end{aligned}\right\} \qquad (3.44)$$

(viii) Flux Limitation

In the preceding sections it has been assumed, in the treatment of electron thermal conduction, that the thermal flux is given by:-

$$Q = 6^{-} \quad \nabla T^{-} \qquad (3.45)$$

This expression is based on collisional arguments, and hence cannot possibly be correct when the temperature changes significantly over a distance of the order of the electron-electron mean free path i.e. when:-

$$\lambda_e \nabla T^{-} \sim T^{-} \qquad (3.46)$$

Salzmann (16) has shown that in the conditions typical of a laser-target interaction, (3.46) can be true, and hence (3.45) will predict unrealisticaly large fluxes that exceed the maximum possible flux set by the product of the random particle flux and the mean thermal energy:-

$$Q \text{ max} = \frac{n\bar{c}}{4} \left(\frac{3}{2} kT^{-}\right) \qquad (3.47)$$

Hence it is normally assumed that for large ∇T^{-} the thermal flux will be independent of ∇T^{-}, and instead will reach a limit that is some fraction of Q max, thus depending solely on n and T^{-}. The actual value of this limit is still open to question. However various possibilities have been proposed, and these will now be discussed.

From numerical simulations of a collisionless plasma, Morse and Nielson (17) show that the electron velocity distribution near the heating zone will consist of a broad flat component of hot electrons leaving the region for the main body of the plasma, together with a cold counterstreaming component that maintains quasi-neutrality. Limiting the discussion to one-dimension they show that the heat flux Q associated with this situation is limited by:-

$$Q/(\tfrac{1}{2}nmv_h^{\,3}) \leq \frac{1}{16} \qquad (3.48)$$

where v_h is the cut off velocity of the hot electrons, the departure from equality being governed by the ratio of the density of hot electrons to the total density. In terms of the temperature of the hot electrons T_h, this can be written as:-

$$\frac{3}{2} kT_h = \frac{1}{2} m \langle v_h^{\,2} \rangle = \frac{1}{6} mv_h^{\,2} \geq 1.68m^{\frac{1}{3}} \left(\frac{Q}{n}\right)^{\frac{2}{3}} \qquad (3.49)$$

Morse and Nielson point out several respects in which this simple model is inadequate. However, if (3.49) is assumed to be approximately correct, it is possible to examine the implications for the steady-state models. In the case of the thin D - W regime, it is assumed that the total laser power density is to be absorbed

at the critical density and is to be transported by heat conduction, (3.15) gives for a hydrogen target (with $\xi = Z = 1$, $\gamma = \frac{5}{3}$):-

$$\frac{3}{2} kT^{-} \approx 7.29 \, m^{\frac{1}{3}} \left(\frac{Q}{n}\right)^{\frac{2}{3}} \qquad (3.50)$$

Comparing this with (3.49) shows that thin D - W should have no trouble in conducting heat away from the absorption region, provided there are no stronger flux limits. However, due to their weak scaling of temperature, the thick regimes could be strongly flux limited, and temperatures above the predicted values are to be expected in the absorption region.

Unfortunately the situation is not as simple as that suggested by the above, since there are processes that induce even stronger flux limits. Bickerton (18) examines the case of strong electron heat conduction when $T^{-} >> T^{+}$. He shows that this situation can produce unstable ion-acoustic waves that will strongly inhibit any heat flow due to the resulting turbulence. By examining the threshold for the instability he deduces that the limiting heat flux is given by:-

$$Q \text{ max} \approx 0.07 n\bar{c} kT^{-} \left(\frac{m}{M}\right)^{\frac{1}{2}} \qquad (3.51)$$

which is a reduction of a factor $0.2 \left(\frac{m}{M}\right)^{\frac{1}{2}}$ on the natural limit (3.47).

Manheimer (19) has pointed out that the above treatment is not entirely adequate, since ion-acoustic turbulence will effect other transport coefficients, such as resistivity and the ion heating rate, which can in turn modify the effective thermal conductivity and the instability threshold. Hence in (19) he has produced an approximate but self-consistent model of ion-acoustic effects, mainly for use in numerical work.

The steady state models take no account of magnetic fields that could arise within the plasma, and, if present, could substantially effect the heat flow. This topic is not entirely relevant to the present work, and hence will only be mentioned briefly.

The dependence of thermal conductivity on magnetic field is such as to inhibit flow perpendicular to $\underset{\sim}{B}$, while conduction along $\underset{\sim}{B}$ is unhindered. The effect is significant when the product of electron collision time and electron cyclotron frequency is greater than unity. (See Braginskii (20)).

A magnetic field will be produced when density and temperature gradients are non-parallel. Using computer simulations Chase et al (21) and Winsor and Tidman (22) have shown that magnetic fields can be generated in this manner in a laser produced plasma, and they report significant effects on the plasma, in particular the hindrance of heat conduction away from the absorption region. Furthermore Tidman and Shanny (23) show that even in the case of an uniformly irradiated target, when one would expect $\nabla n \times \nabla T = 0$, magnetic fields can still arise due to instability. Any perturbation in the uniform temperature gives rise to a small $\underset{\sim}{B}$ field which then enhances the perturbation through the $\underset{\sim}{B}$ dependence of thermal conductivity.

A further possible source of magnetic field is anisotropic absorption, such as resonance absorption. Here, electrons are more strongly heated in the direction normal to the critical surface. These will stream out of the absorption region and be reflected from an electrostatic sheath at the edge of the main body of the plasma. Those electrons whose velocity is not exactly normal to the critical surface will return to the heating zone via a circular route, thus creating current loops with their accompanying solenoidal magnetic field. (see Ref. (24)).

Stamper et al have reported experimental observations of magnetic fields in a laser produced plasma (see e.g. Ref. (25)), but their existence in general is still a matter for speculation.

CHAPTER 4

(i) Introduction

The results obtained from the computer code will now be presented. Section (iv) gives a brief description of general behaviour using contour plots of the various variables for a few different cases. Section (v) takes results from a large number of runs and compares them with the theoretical results of Chapter 3, with particular reference to the predicted maximum temperatures. However it is first necessary to discuss briefly the strength of flux limitation to be included (Section (iii)), and to mention a computational problem relating to space-step size.

(ii) A Computational Consideration

Since it is the steady-state models that are of the main interest, it is necessary for the computer code to be run for a relatively long physical time (a few nanoseconds), in order to ensure that an approximate steady state has been reached. To avoid the possibility of the high absorption region moving off the back of the grid, these long physical times automatically require the use of somewhat large values of Δz. Perhaps even more critical in determining the size of Δz is the requirement that the plasma be given sufficient room to expand at the front of the target. Some justification could be given

for allowing the expanding plasma to run off the front of the grid and be ignored, since it is hot and tenuous and should absorb little of the laser energy. However this argument would not appear to be entirely valid. Puell suggests that the plasma fan can absorb up to a third of the total laser energy, and this is confirmed by the computer code, it being found that, in some cases, ignoring the expanding plasma cloud could lead to a significant rise in temperature in the high absorption region. Hence it was decided to chose ΔZ so that at least most of the expanding plasma is retained on the grid.

This use of large Δz can be criticised, since in most cases Δz is as large or larger than the spot radius R_o. Since the length of the region of one-dimensional expansion is also approximately R_o, it could be argued that the grid is too coarse to model the plasma correctly. However Fig. 4.1 shows T^- along the axis of a CO_2 laser ($R_o = 10^{-3}$cm, $\phi = 2 \times 10^{14}$ c.g.s) at time $t = 10^{-9}$ sec obtained from two runs with $\Delta z = 10^{-4}$ cm and $\Delta z = 10^{-3}$ cm. It can be seen that in the second case, although the grid is extremely coarse for the length of the region under consideration, the gross properties of the plasma are still modelled quite well; of course accuracy should improve as the plasma dimensions increase.

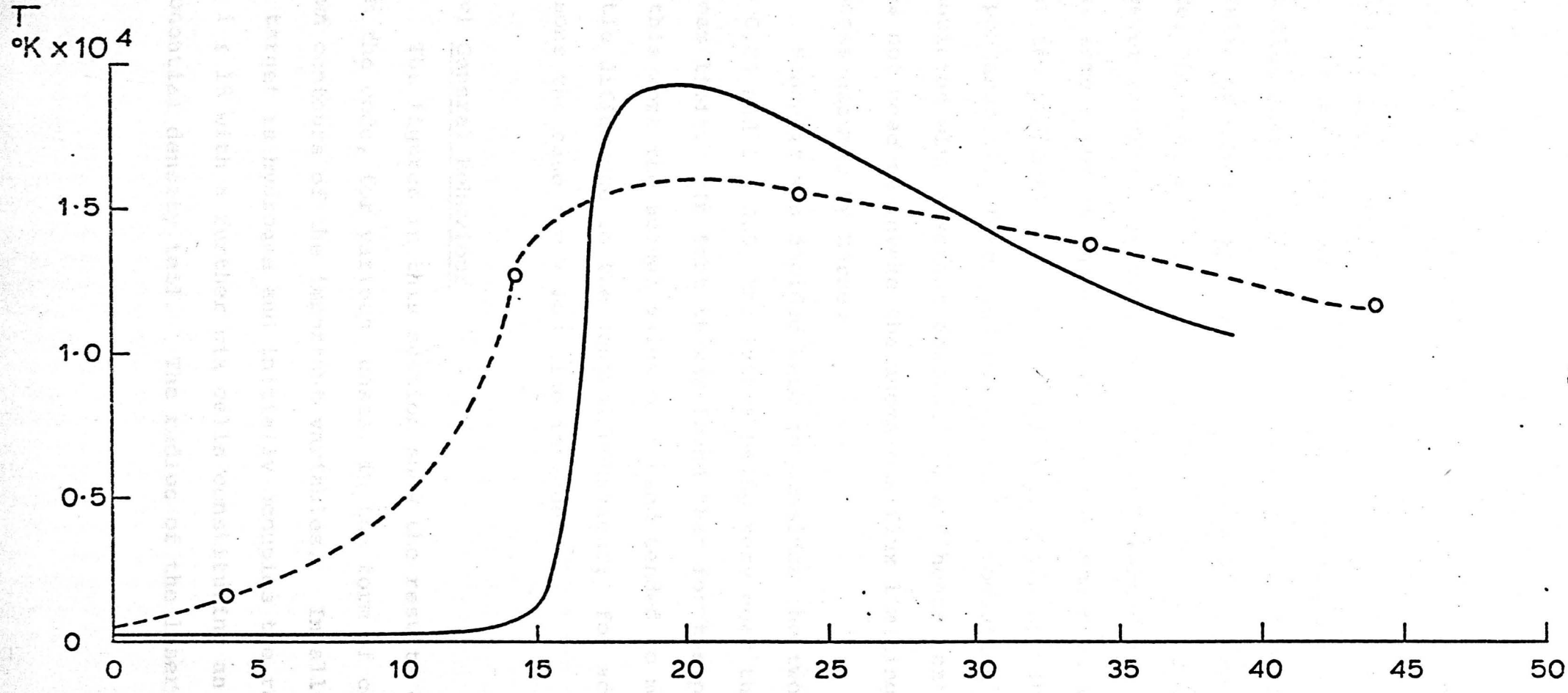

Fig. 4.1

Electron temperature along the axis of a CO_2 laser ($R_o = 10^{-3}$ cm, $\phi = 2 \times 10^{14}$ c.g.s) at $t = 10^{-9}$ sec comparing results obtained with $\Delta z = 10^{-4}$cm (——) with those for $\Delta z = 10^{-3}$ cm(- - - - -)

(iii) Flux Limitation

It was necessary to decide on a suitable value for the flux limit coefficient f. By comparing experimental results of hot ion production with those of a computer code, Morse et al (1) suggested that $0.03 \lesssim f \lesssim 0.1$. However recently Gitomer, Henderson and Remund (2) have cast some doubt on Malone's work, since they have shown that the production of hot ions can be explained in terms of ponderomotive force and hot electron production associated with resonant absorption, and hence that one does not need to invoke the anomalous flux limiting process assumed by Morse.

Hence it was decided here to consider the two cases $f = 0.05$ and $f = 0.5$, the latter being very near the free-stream limit. In fact it was found that for the purposes of this work the actual value of f used tended to make little difference to the general behaviour; for academic reasons the case $f = \infty$ was also included.

(iv) General Behaviour

The figures in this section show the results obtained from the code, for various cases, in the form of computer-drawn contours of the important variables. In all cases the target is hydrogen and initially occupies the region $1 \lesssim i \lesssim 15$ with a further six cells constituting an exponential density tail. The radius of the laser is

always 10^{-3} cm and the flux limit coefficient f is set at 0.05 unless otherwise stated. A 50 x 15 grid was used but only the eight rows of cells nearest the Z-axis are plotted; the ticks on each axis represent the cell boundaries and the size of the space steps used are indicated in each case. The velocity and temperature contour levels are expressed in units of 10^6 cm/sec and 10^6 ^oK respectively.

Figures 4.2 - 4.6 show the distributions obtained with a ruby laser with $\phi = 10^{18}$ c.g.s - well within the thin S-R regime - at two different times. On examining Fig. 4.2(a) it can be seen that a slight density well forms in the low density region but does not penetrate to the critical density ($n_c = 2.3 \times 10^{21}$ cc^{-1}). Apart from the general expansion outwards of the lower contours Fig. 4.2(b) shows little change in time. (The somewhat peculiar behaviour near the critical density with the accompanying double peak of the temperatures soon dies away and the structure of 4.2(a) is regained. It is probably caused by the over-reaction of the artificial viscosity to some discontinuous effect associated with the finite size of the grid). There is very little penetration into the target material.

The velocities show a typical expansion fan structure becoming flattened as time progresses. Of course the grid is too coarse to show the region of 1 - D expansion clearly.

cont. on p.56

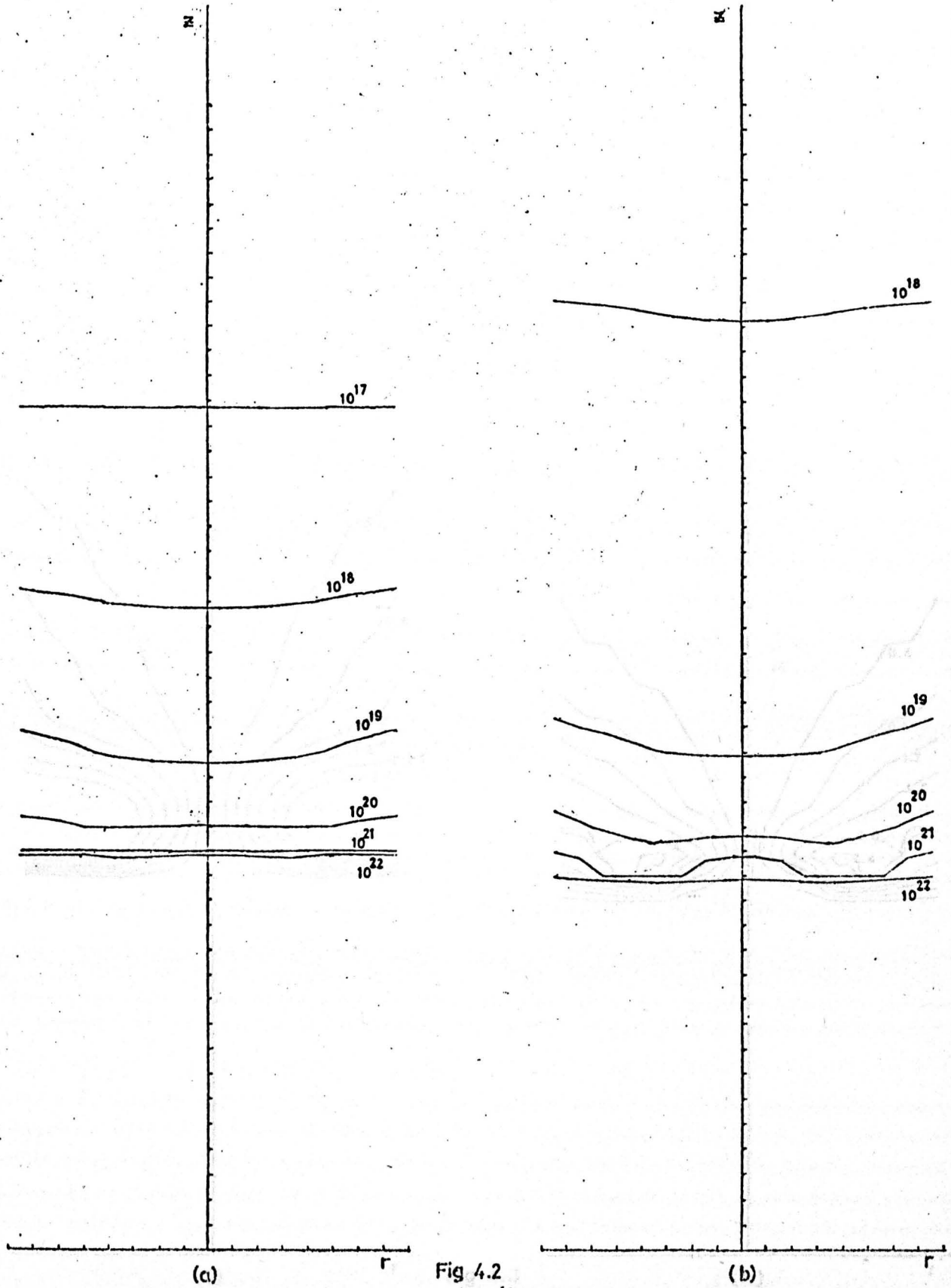

Fig 4.2
n (cc^{-1})
Ruby Laser, $\phi = 10^{18}$ c.g.s.
$\Delta r = 2.5 \times 10^{-4}$ cm, $\Delta z = 2 \times 10^{-3}$ cm.

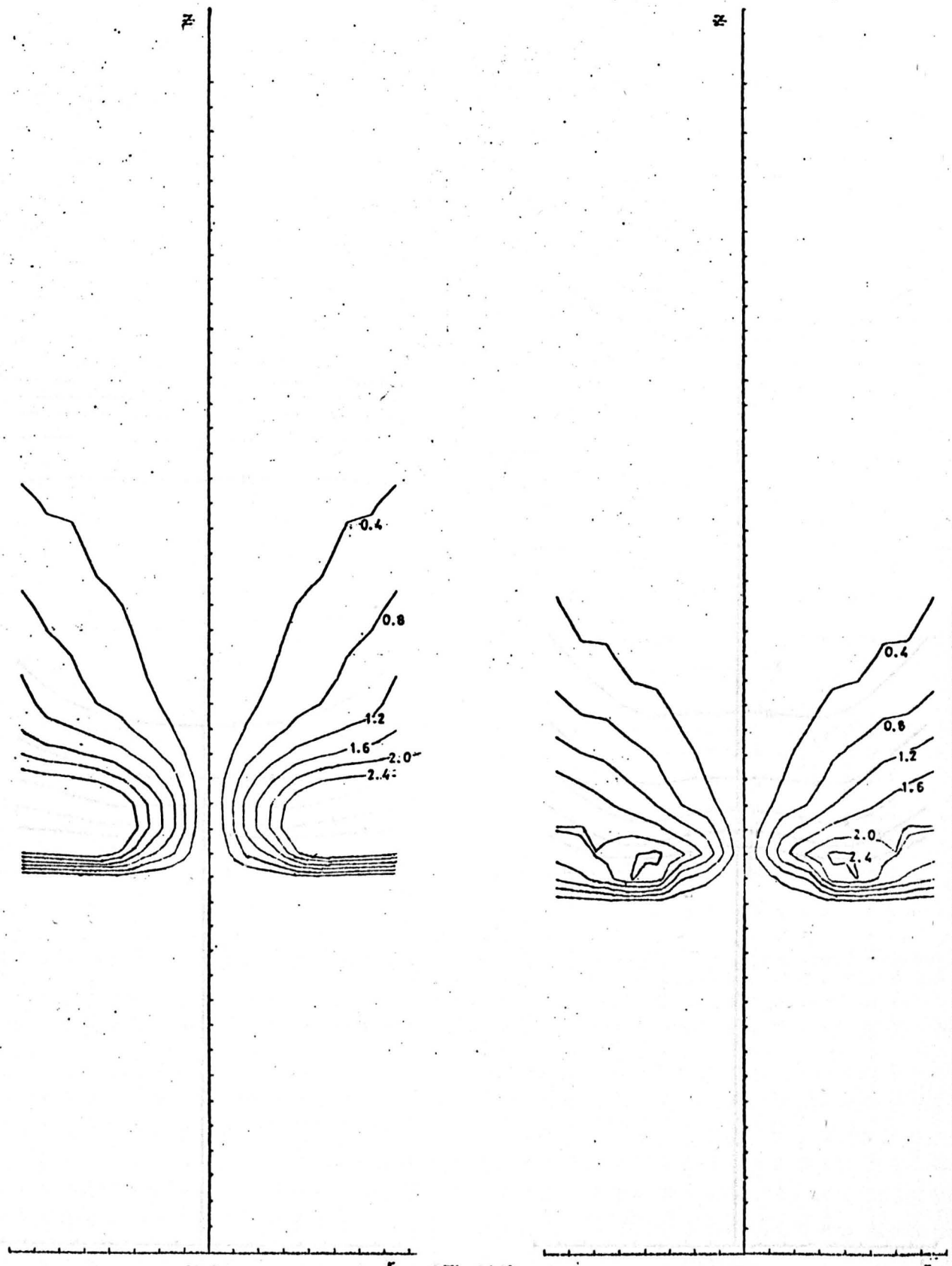

Fig 4.3
v_r (cm/sec $\times 10^6$)
Ruby Laser, $\phi = 10^{18}$ c.g.s.
$\Delta r = 2.5 \times 10^{-4}$ cm, $\Delta z = 2 \times 10^{-3}$ cm.

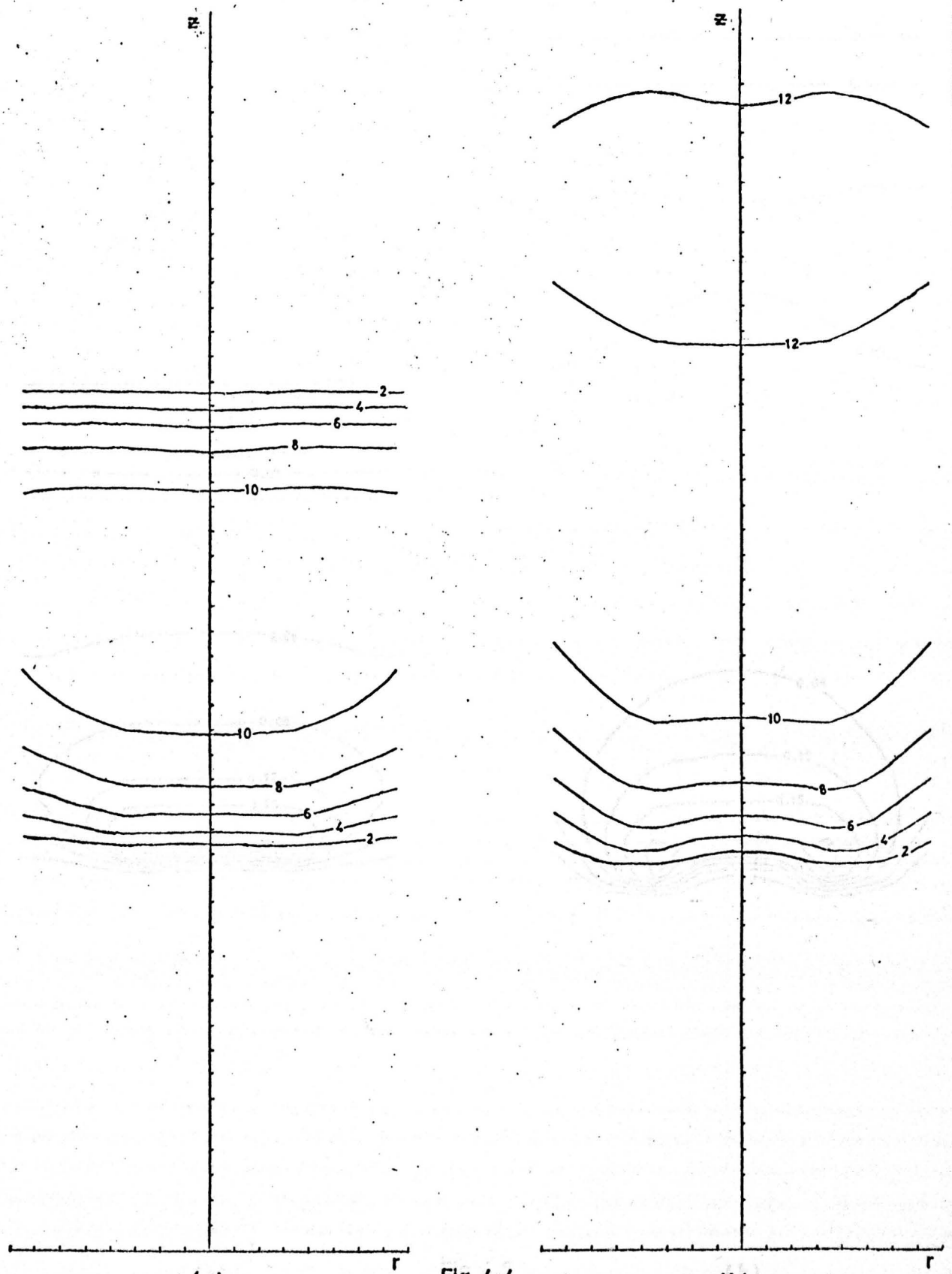

Fig 4.4
v_z (cm/sec $\times 10^6$)
Ruby Laser, $\phi = 10^{16}$ c.g.s.
$\Delta r = 2.5 \times 10^{-4}$ cm, $\Delta z = 2 \times 10^{-3}$ cm.

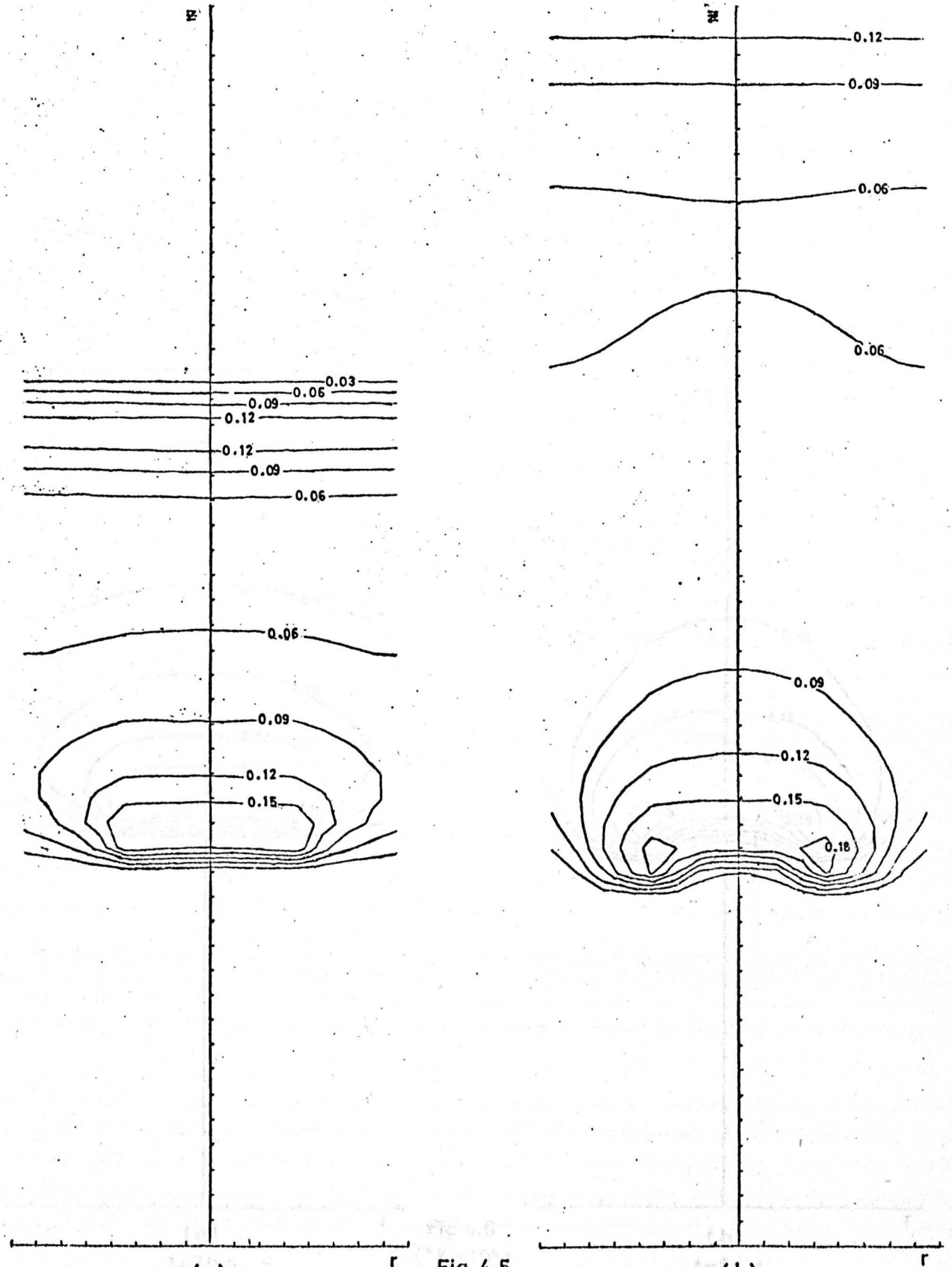

Fig 4.5
T^+ (°K × 10^6)
Ruby Laser, $\phi = 10^{18}$ c.g.s.
$\Delta r = 2.5 \times 10^{-4}$ cm, $\Delta z = 2 \times 10^{-3}$ cm.

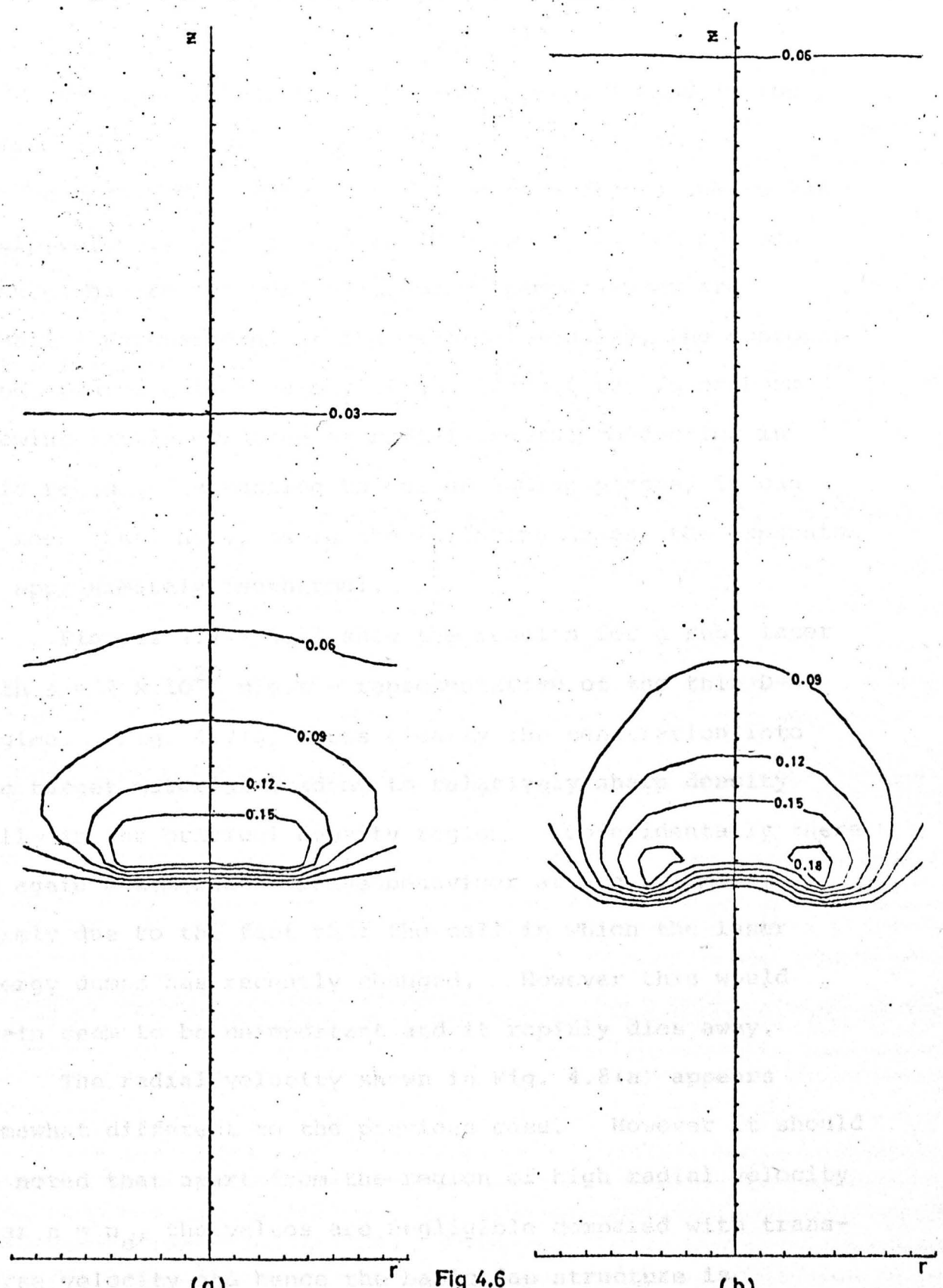

Fig 4.6
$T^{-}(^{\circ}K \times 10^{6})$
Ruby Laser, $\phi = 10^{18}$ c.g.s.
$\Delta r = 2.5 \times 10^{-4}$ cm, $\Delta z = 2 \times 10^{-3}$ cm.

Here, as in all the following cases, a rise in ion temperature towards the edge of the expanding plasma can be observed. This is a compressive effect due to the sharp velocity gradient in this region. It can be seen that elsewhere the ion and electron temperatures are equal. Furthermore, at the critical density, the contours bend upwards quite sharply at the edge of the laser beam showing little evidence of radial thermal conduction in this region. Returning to the expanding plasma, it can be seen that here, as in the following cases, the expansion is approximately isothermal.

Figures 4.7 - 4.11 show the results for a ruby laser with $\phi = 2 \times 10^{20}$ c.g.s - representative of the thin D-W regime. Fig. 4.7(a) shows clearly the penetration into the target material leading to relatively sharp density well in the critical density region. Coincidentally there is again a somewhat strange behaviour at 5 n.s., most likely due to the fact that the cell in which the laser energy dumps has recently changed. However this would again seem to be unimportant and it rapidly dies away.

The radial velocity shown in Fig. 4.8(a) appears somewhat different to the previous case. However it should be noted that apart from the region of high radial velocity near $n = n_c$, the values are negligible compared with transverse velocity and hence the basic fan structure is retained. It can be seen that the ions are now somewhat cooler than the electrons in the high absorption region. There is still very little evidence of radial thermal conduction at $n = n_c$.

cont. on p.62

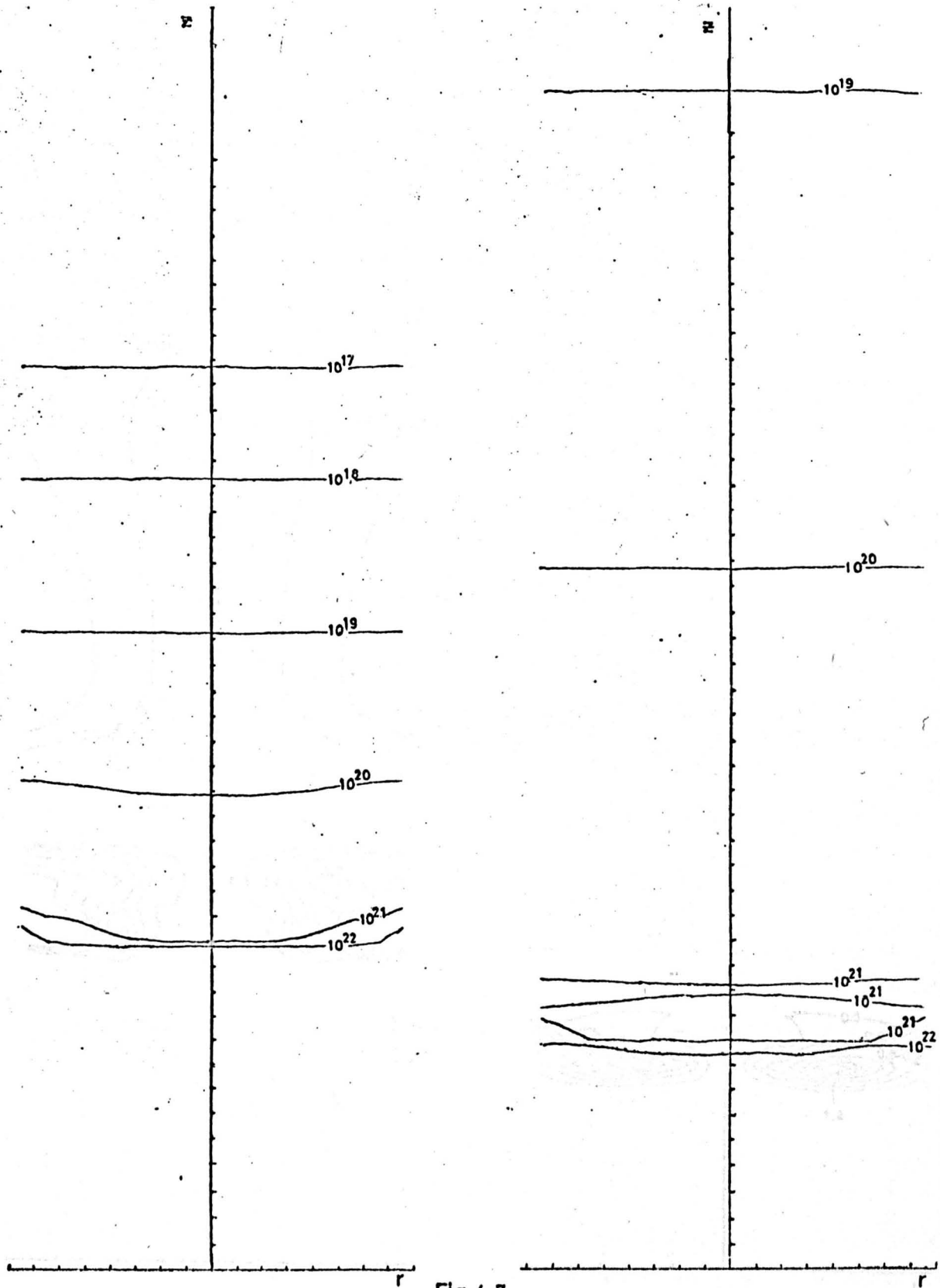

Fig 4.7

n (cc^{-1})

Ruby Laser, $\phi = 2\times10^{20}$ c.g.s.

$\Delta r = 2.5\times10^{-4}$ cm, $\Delta z = 5\times10^{-3}$ cm.

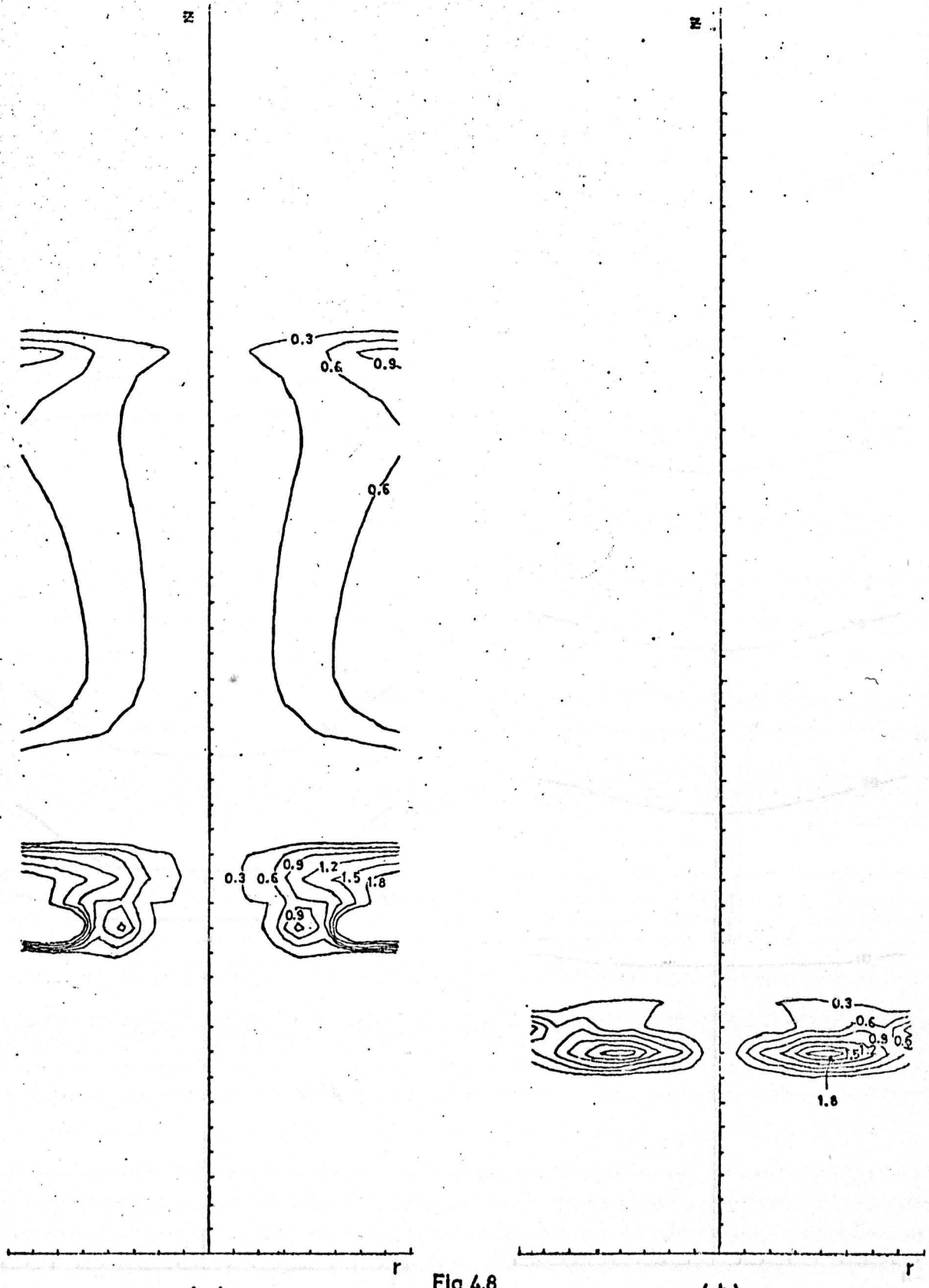

Fig 4.8
v_r (cm/sec $\times 10^6$)
Ruby Laser, $\phi = 2 \times 10^{20}$ c.g.s.
$\Delta r = 2.5 \times 10^{-4}$ cm, $\Delta z = 5 \times 10^{-3}$ cm.

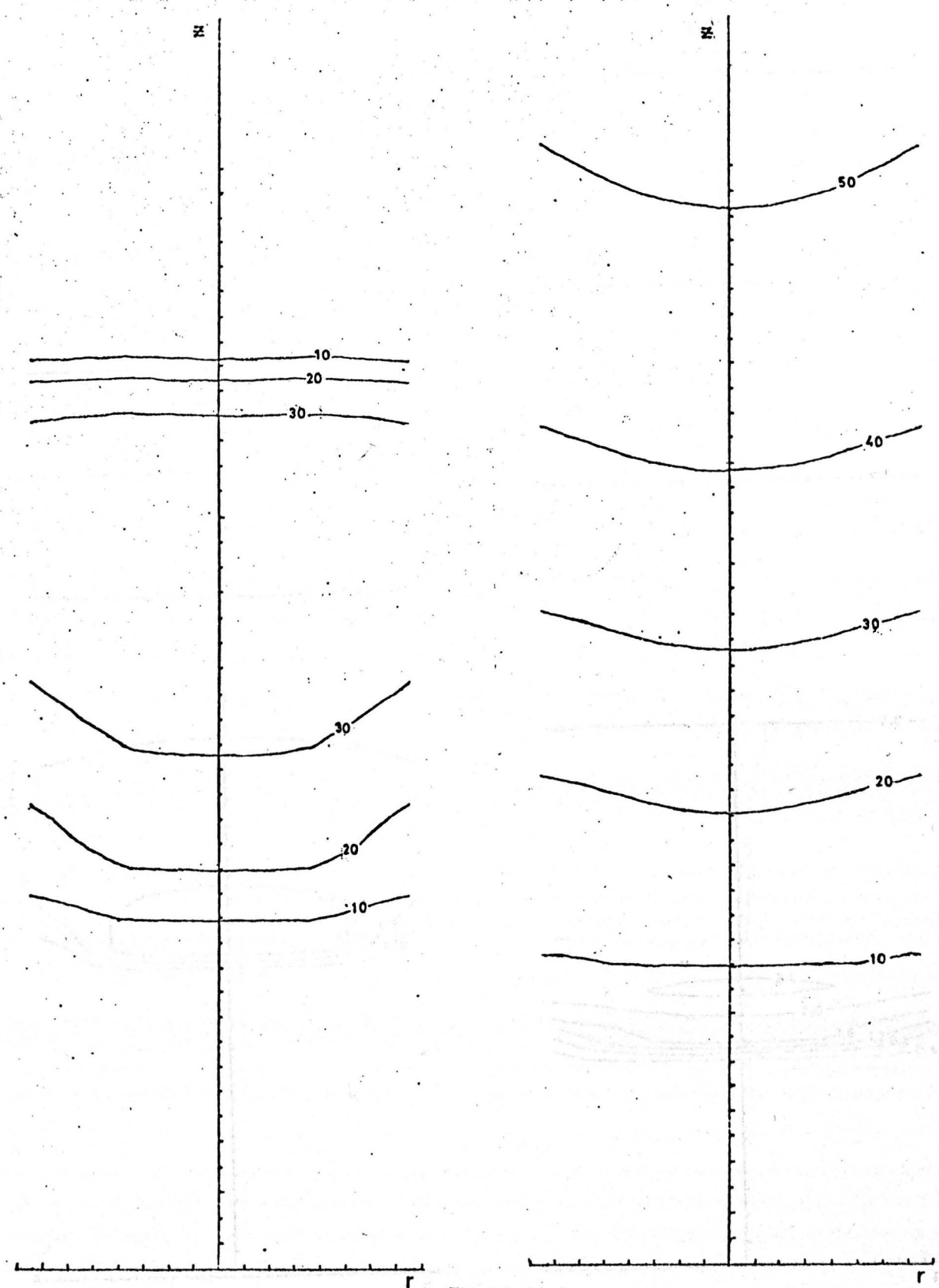

(a)
t = 2 n.s.

Fig 4.9
v_z (cm/sec × 10^6)
Ruby Laser, $\phi = 2 \times 10^{20}$ c.g.s.
$\Delta r = 2.5 \times 10^{-4}$ cm, $\Delta z = 5 \times 10^{-3}$ cm.

(b)
t = 5 n.s.

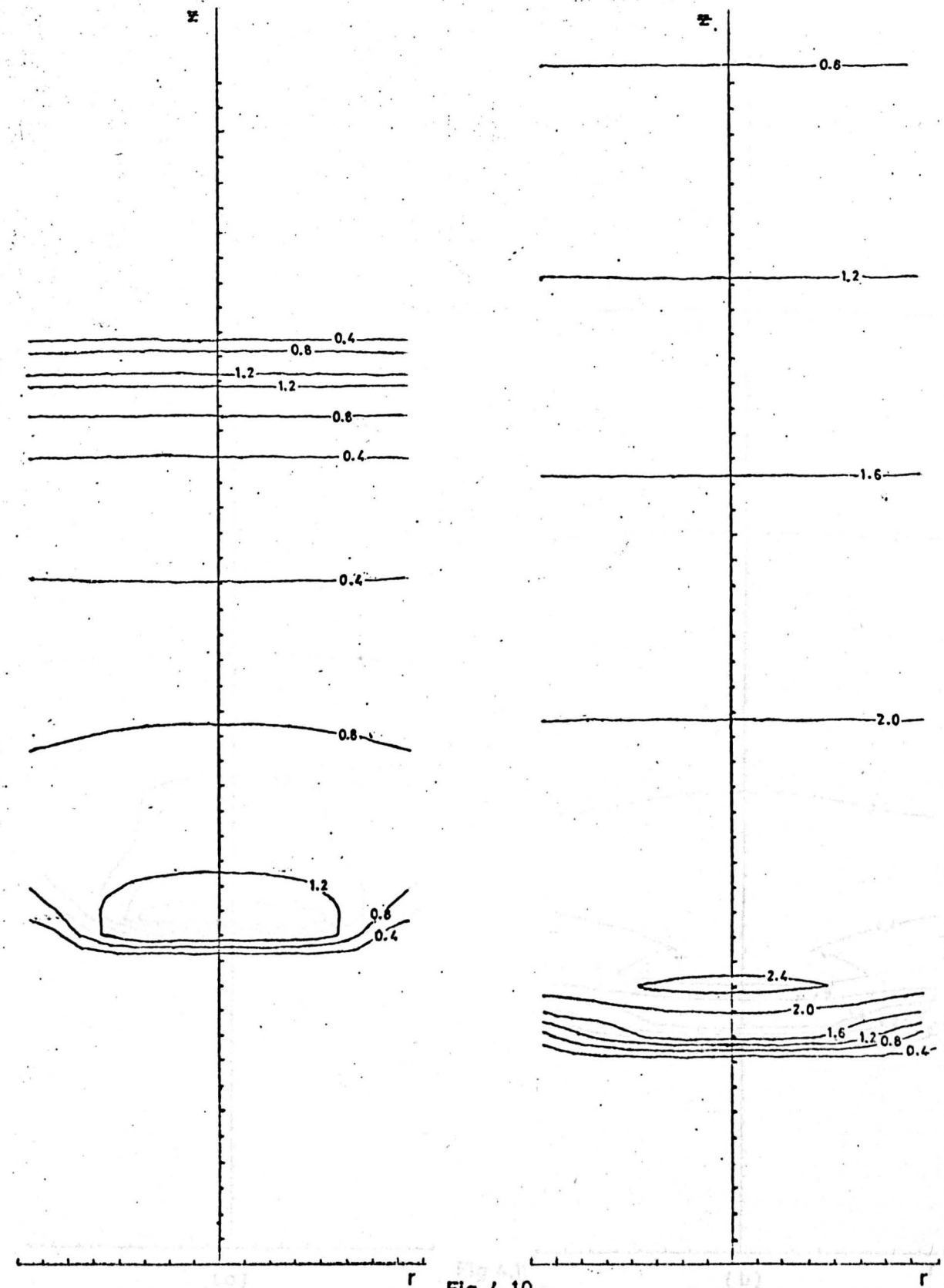

Fig 4.10

T^* ($°K \times 10^6$)

Ruby Laser, $\phi = 2 \times 10^{20}$ c.g.s.

$\Delta r = 2.5 \times 10^{-4}$ cm, $\Delta z = 5 \times 10^{-3}$ cm.

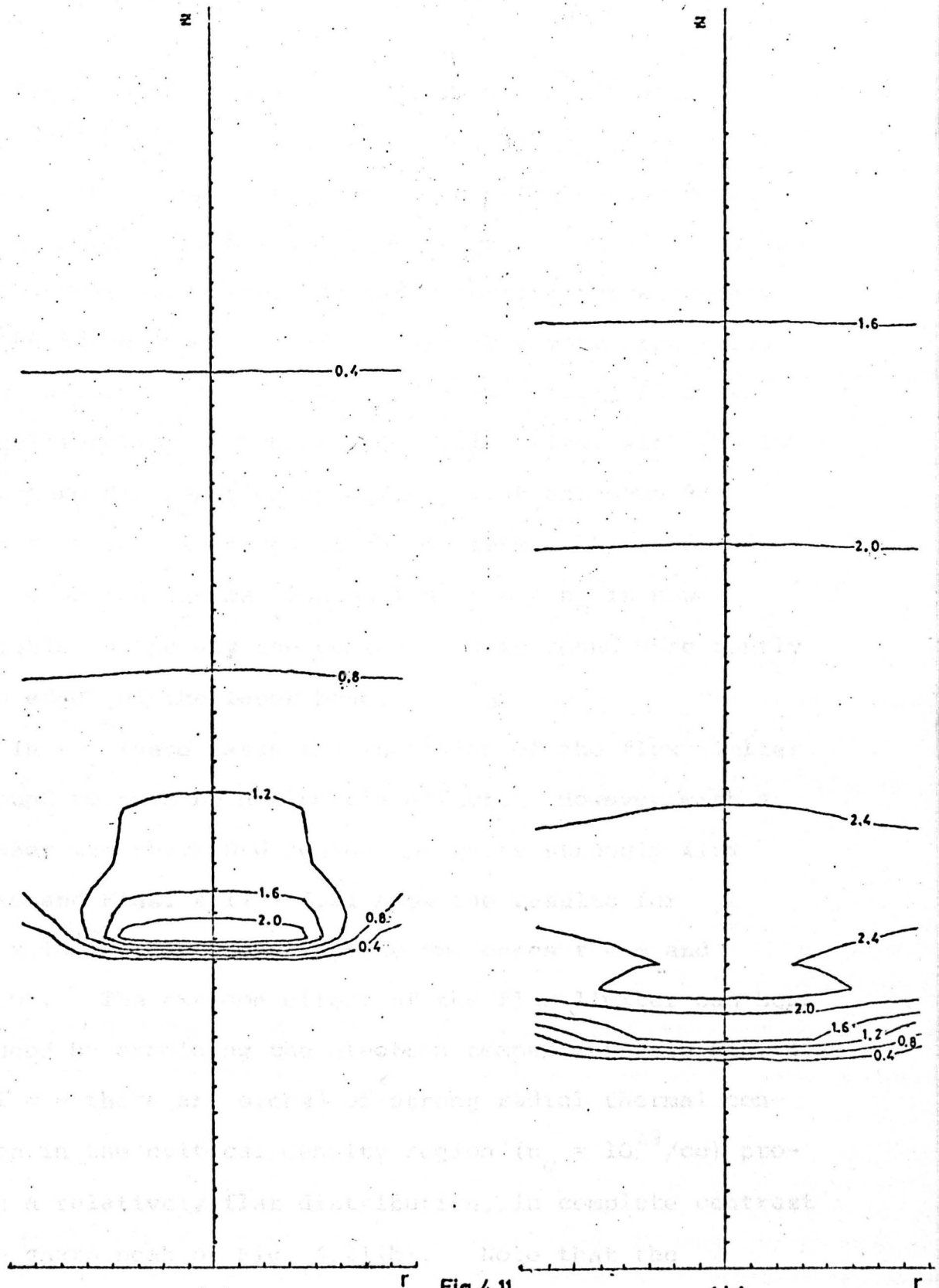

Fig 4.11
T^{-} (°K × 10^6)
Ruby Laser, $\phi = 2 \times 10^{20}$ c.g.s.
$\Delta r = 2.5 \times 10^{-4}$ cm, $\Delta z = 5 \times 10^{-3}$ cm.

Figures 4.12 - 4.16 are for a ruby laser with $\phi = 5 \times 10^{21}$ c.g.s - representative of the thick D-W regime. It is important to note that Δr has now been doubled in size and hence the laser radius only covers two cells. Fig. 4.12 shows the laser burning quite rapidly into the target material and producing a very pronounced density well. Comparing Fig. 4.15 and Fig. 4.16 shows the equilibration is nowhere near completion, with the ion temperature distribution relatively flat and some 67% cooler than the electrons at the maximum. As expected radial electron thermal conduction at $n = n_c$ is now detectable in the way the contours curve round more gently at the edge of the laser beam.

In all these cases the inclusion of the flux limiter was found to have no noticeable effect. However with a CO_2 laser the thick D-W regime is quite strongly flux limited and Figs. 4.17 - 4.21 show the results for $\phi = 5 \times 10^{18}$ c.g.s comparing the two cases $f = \infty$ and $f = 0.05$. The extreme effect of the flux limiter can best be judged by examining the electron temperatures in Fig. 4.21. With $f = \infty$ there are signs of strong radial thermal conduction in the critical density region ($n_c = 10^{19}$/cc) producing a relatively flat distribution, in complete contrast to the sharp peak of Fig. 4.21(b). Note that the disparity in temperature is so great (approximately a factor 4) that different contour levels have had to be used for the two cases. The large temperature gradients produced

cont. on p.73

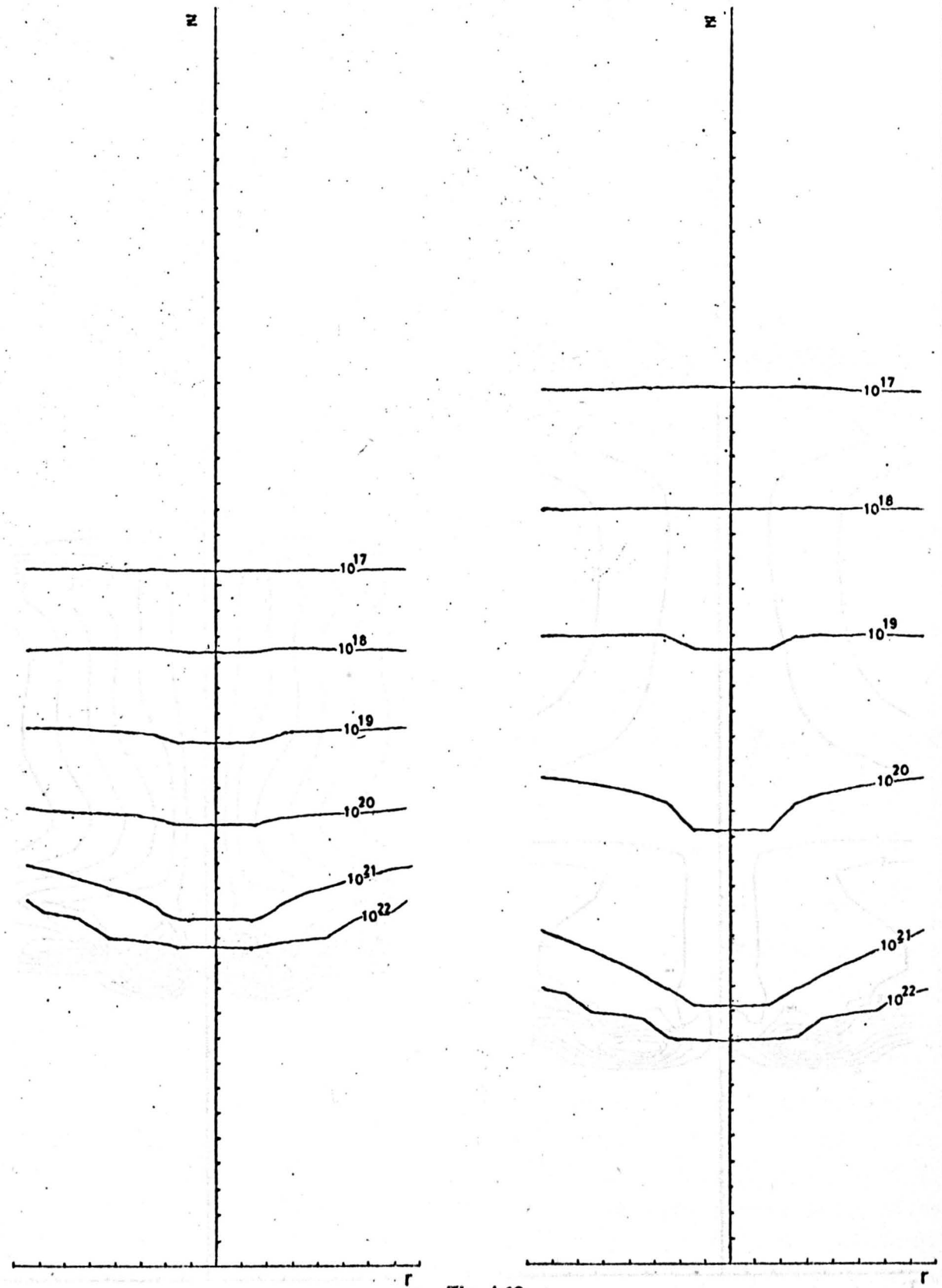

(a) t = 1 n.s.

Fig 4.12
n (cc^{-1})
Ruby Laser, $\phi = 5 \times 10^{21}$ c.g.s.
$\Delta r = 5 \times 10^{-4}$ cm, $\Delta z = 8 \times 10^{-3}$ cm.

(b) t = 2 n.s.

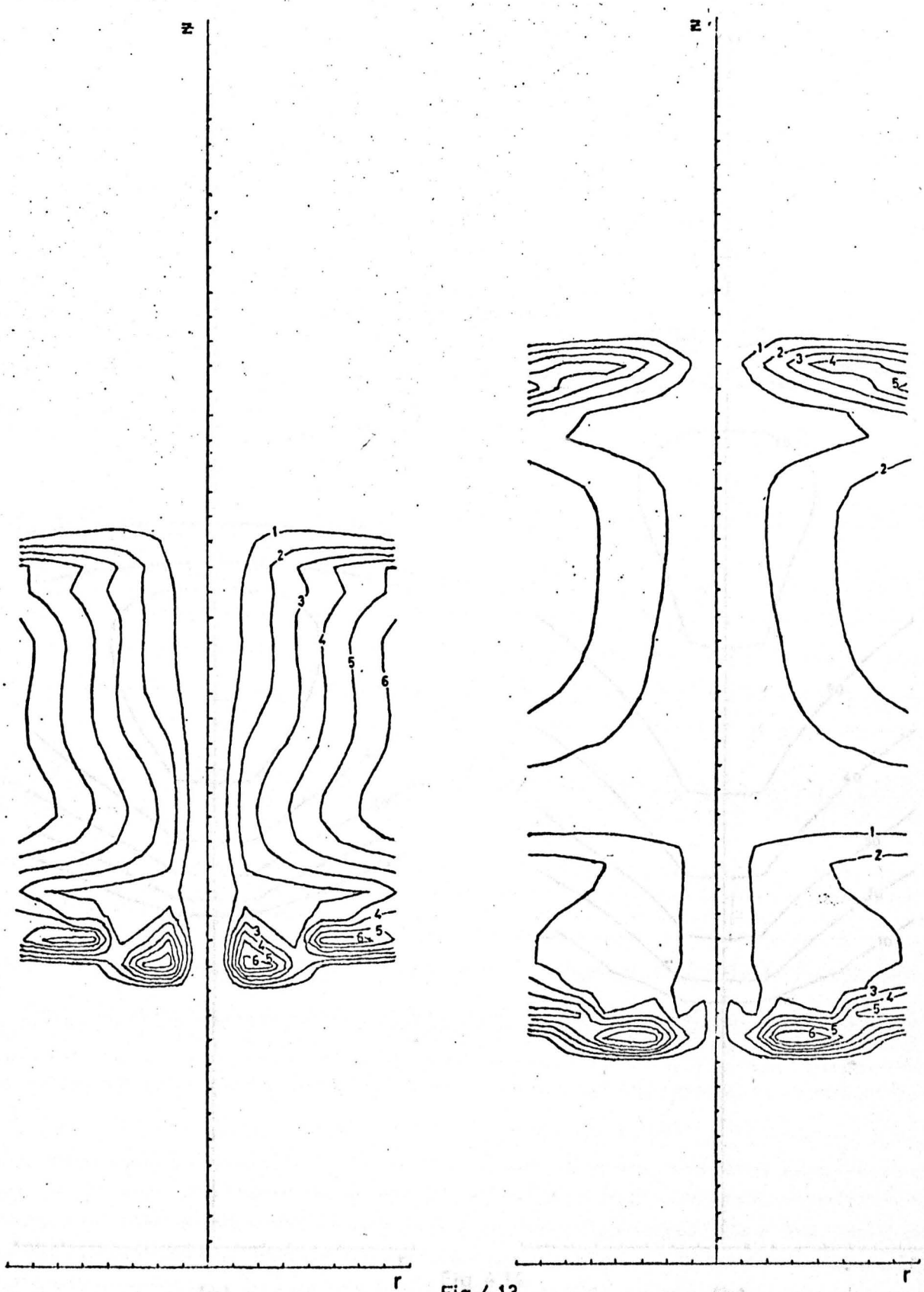

(a) t=1 n.s.

Fig 4.13
v_r (cm/sec × 10^6)
Ruby Laser, $\phi = 5 \times 10^{21}$ c.g.s.
$\Delta r = 5 \times 10^{-4}$ cm, $\Delta z = 8 \times 10^{-3}$ cm.

(b) t=2 n.s.

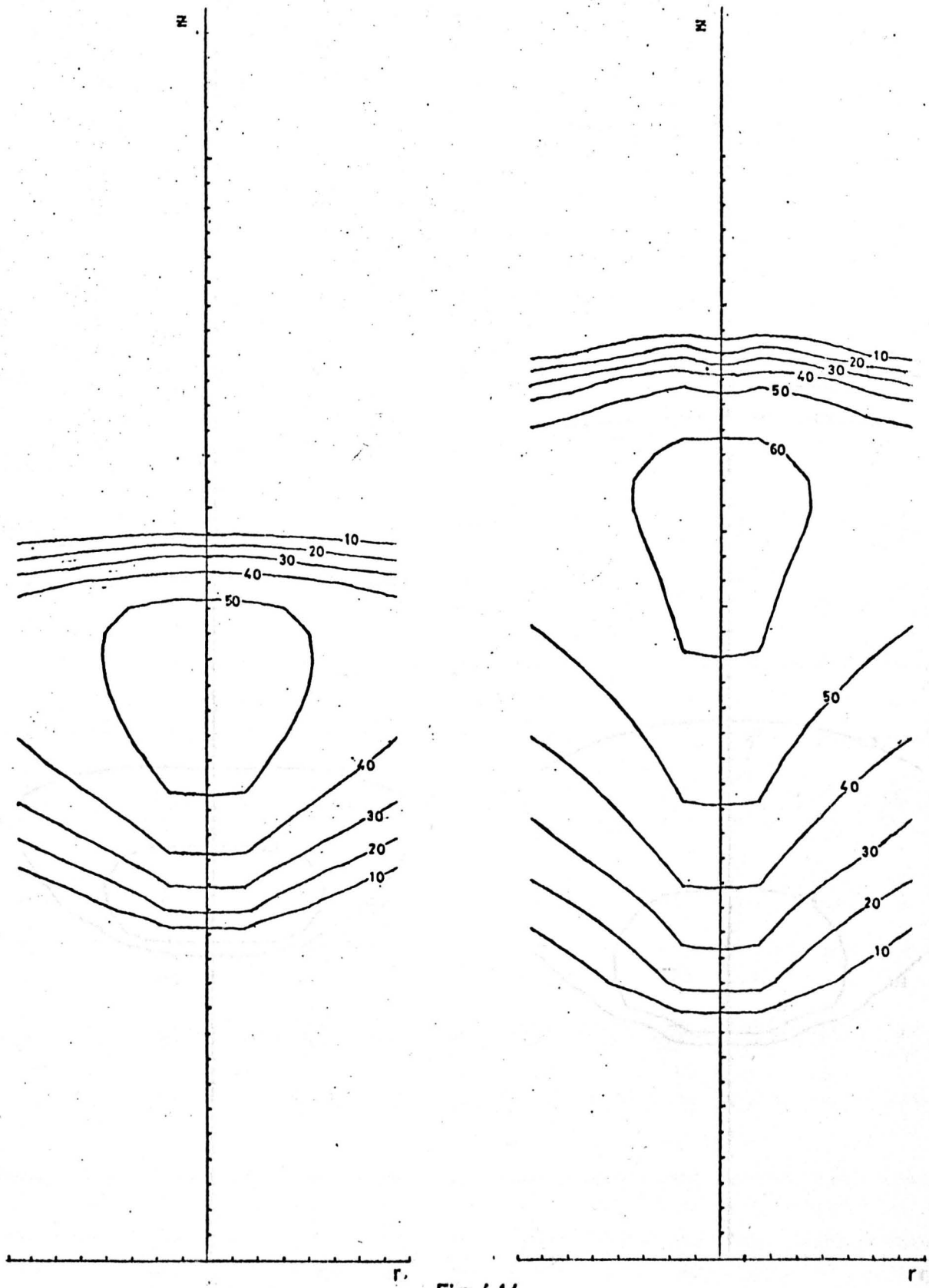

(a)
t = 1 n.s.

Fig 4.14
v_z (cm/sec $\times 10^6$)
Ruby Laser, $\phi = 5 \times 10^{21}$ c.g.s.
$\Delta r = 5 \times 10^{-4}$ cm, $\Delta z = 8 \times 10^{-3}$ cm.

(b)
t = 2 n.s.

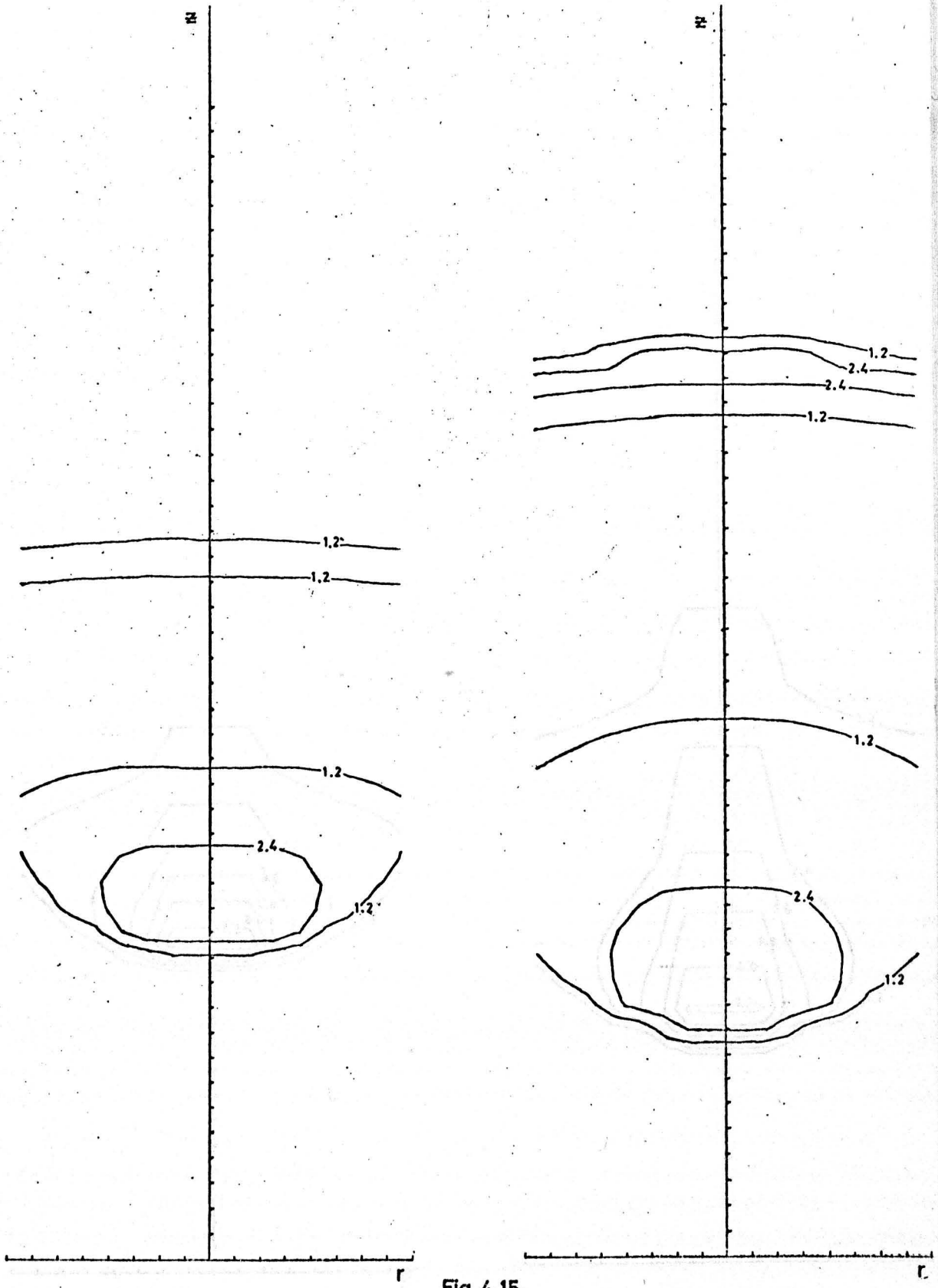

(a) t = 1 n.s.

Fig 4.15
T^* ($^\circ K \times 10^6$)
Ruby Laser, $\phi = 5 \times 10^{21}$ c.g.s.
$\Delta r = 5 \times 10^{-4}$ cm, $\Delta z = 8 \times 10^{-3}$ cm.

(b) t = 2 n.s.

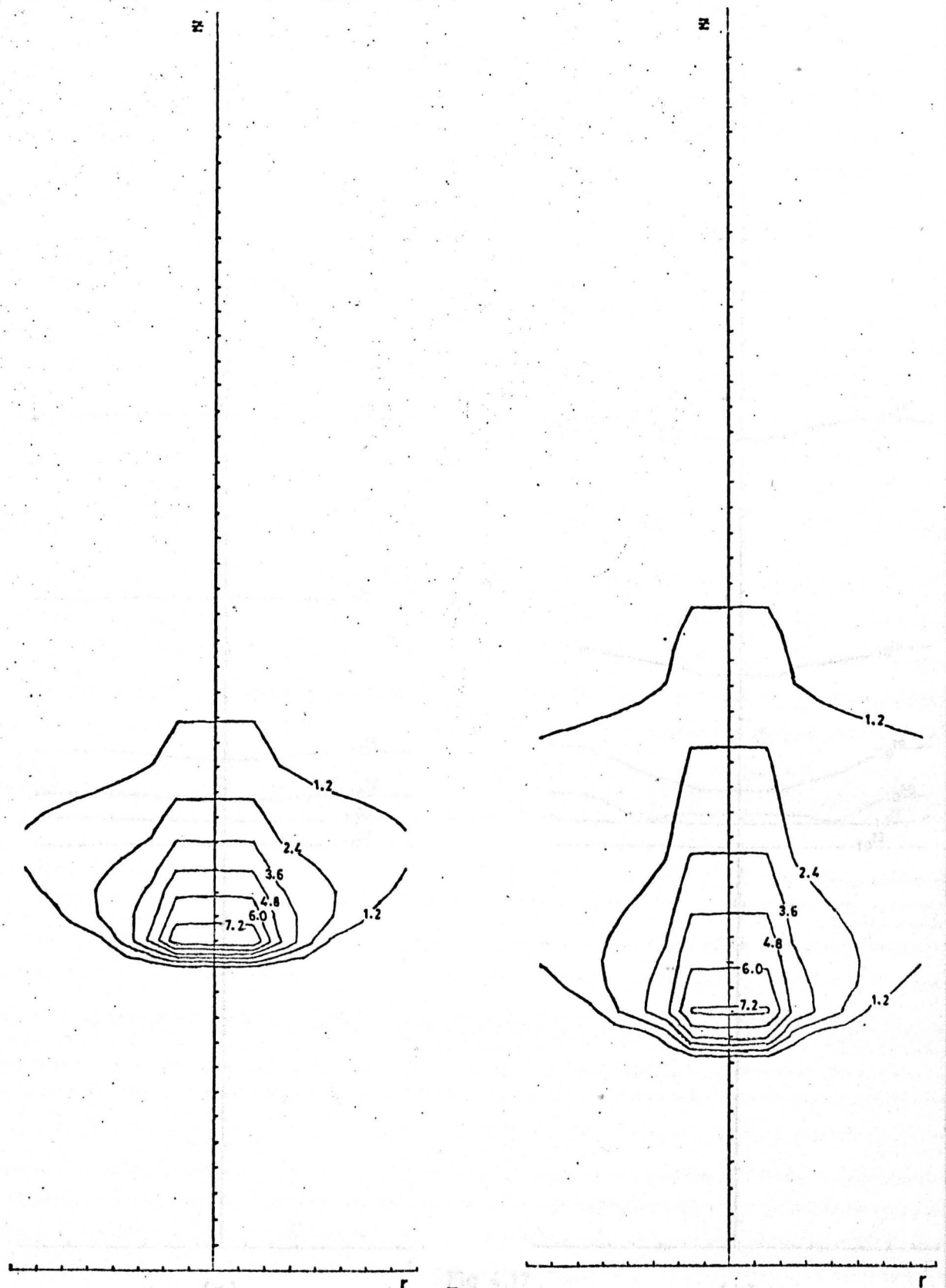

Fig 4.16
T^- ($^\circ K \times 10^6$)

(a) t = 1 n.s.

(b) t = 2 n.s.

Ruby Laser, $\phi = 5 \times 10^{21}$ c.g.s.
$\Delta r = 5 \times 10^{-4}$ cm, $\Delta z = 8 \times 10^{-3}$ cm.

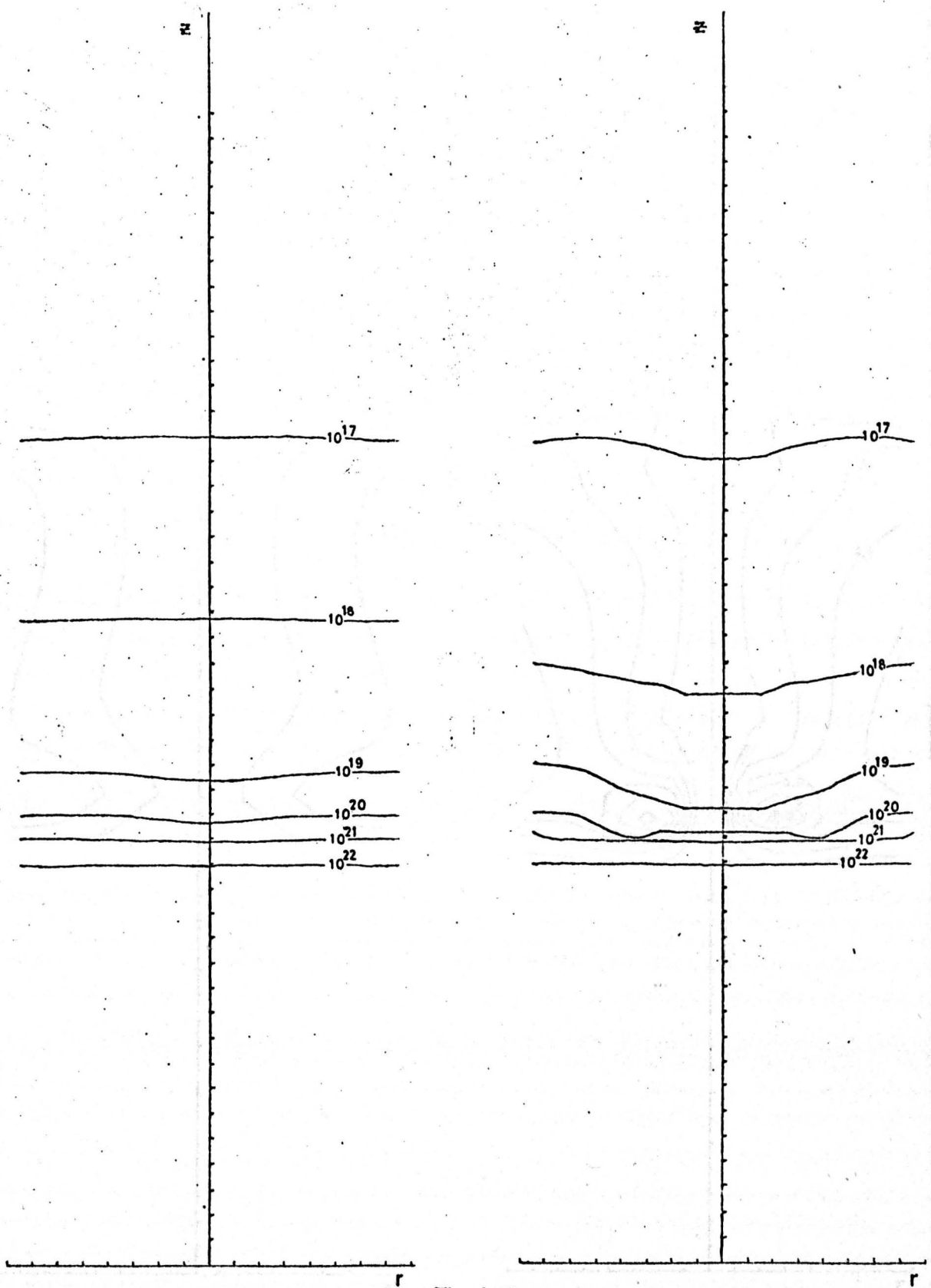

(a)
$f = \infty$

Fig 4.17
n (cc^{-1})
CO_2 Laser, $\phi = 5 \times 10^{18}$ c.g.s.
$\Delta r = 5 \times 10^{-4}$cm, $\Delta z = 2 \times 10^{-3}$cm.
t = 1 n.s.

(b)
$f = 0.05$

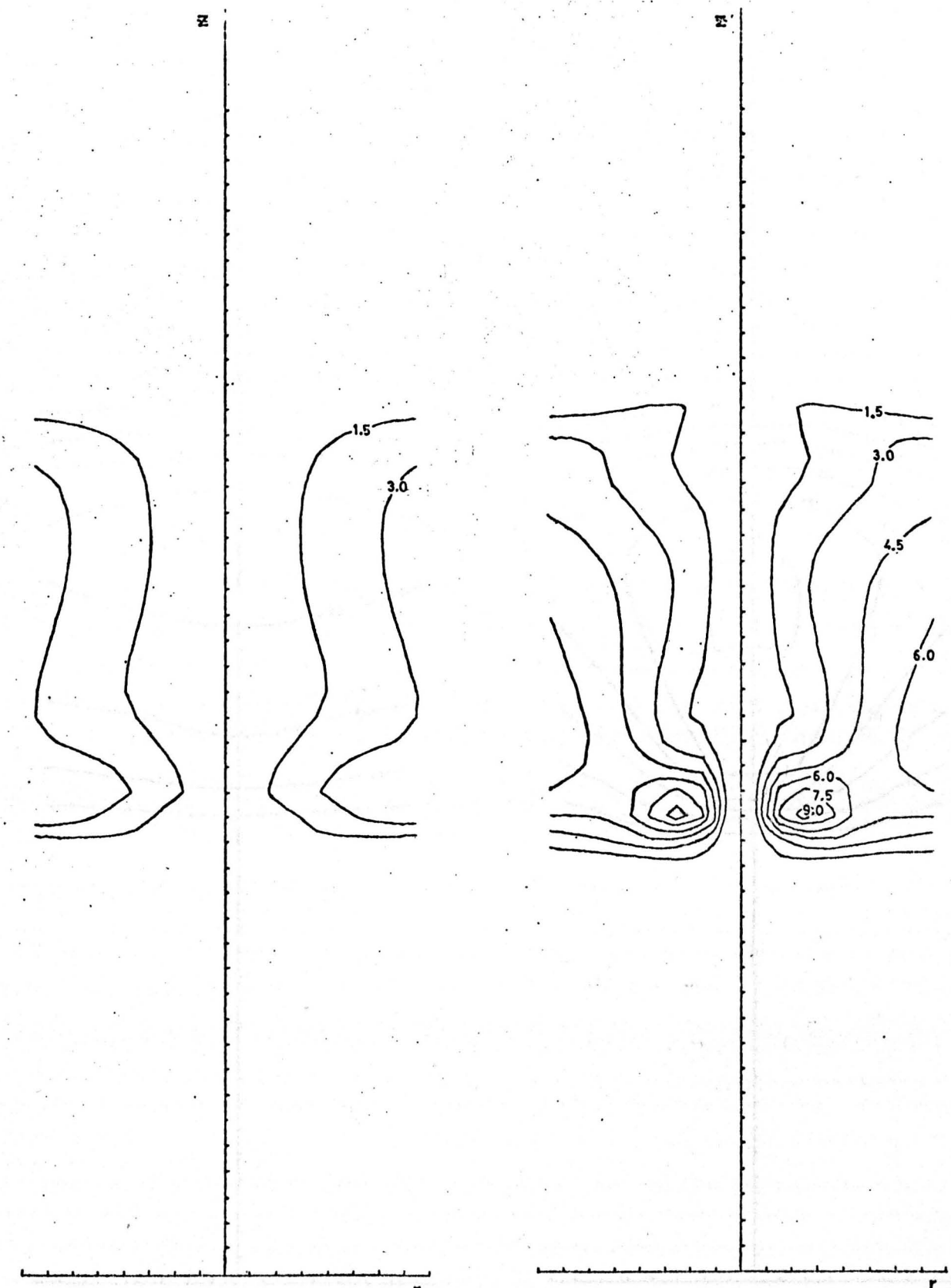

Fig 4.18
v_r (cm/sec $\times 10^6$)
CO_2 Laser, $\phi = 5 \times 10^{18}$ c.g.s.
$\Delta r = 5 \times 10^{-4}$ cm, $\Delta z = 2 \times 10^{-3}$ cm.
t = 1 n.s.

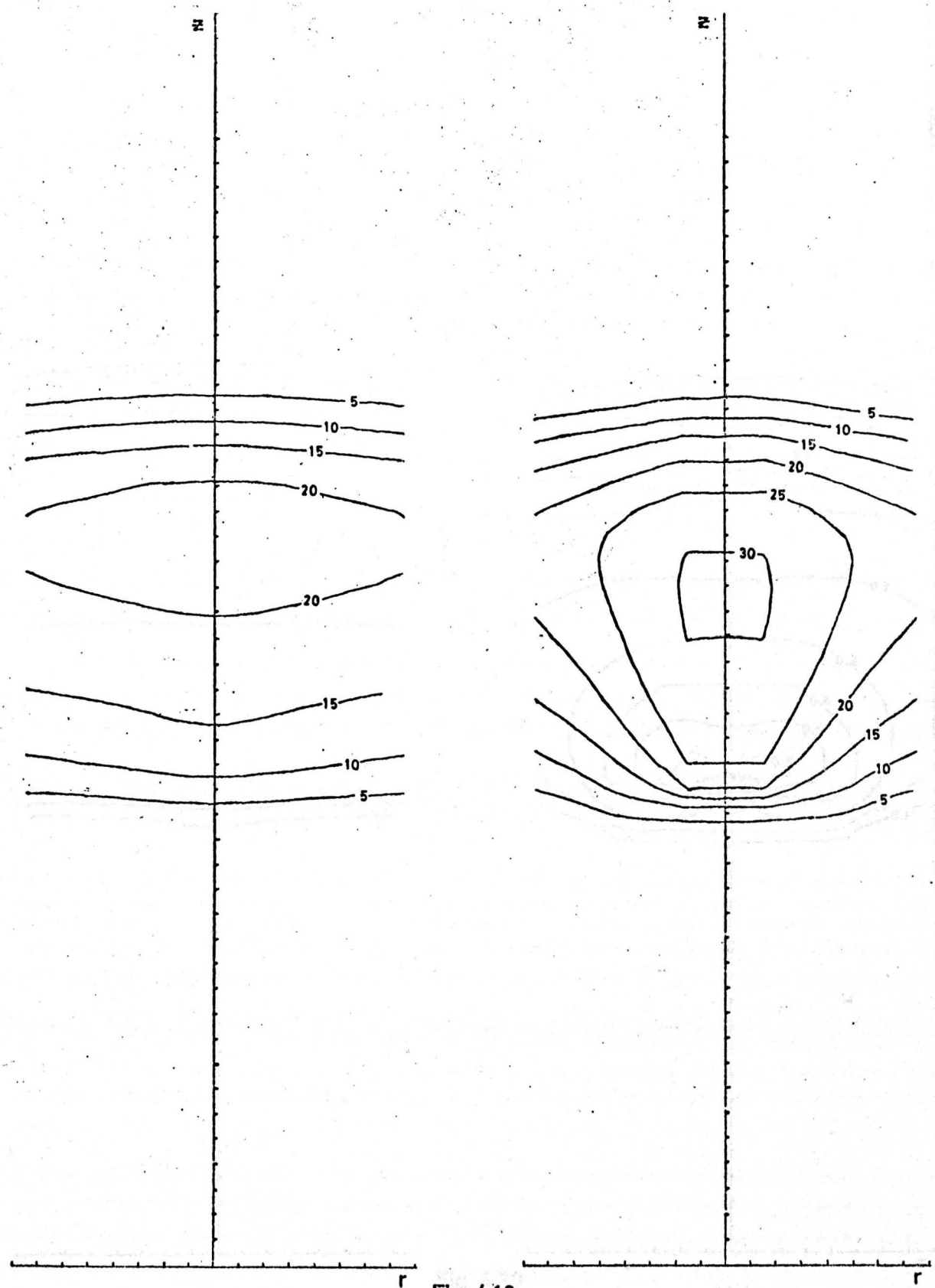

Fig 4.19
v_z (cm/sec $\times 10^6$)
CO_2 Laser, $\phi = 5 \times 10^{18}$ c.g.s.
$\Delta r = 5 \times 10^{-4}$ cm, $\Delta z = 2 \times 10^{-3}$ cm.
t = 1 n.s.

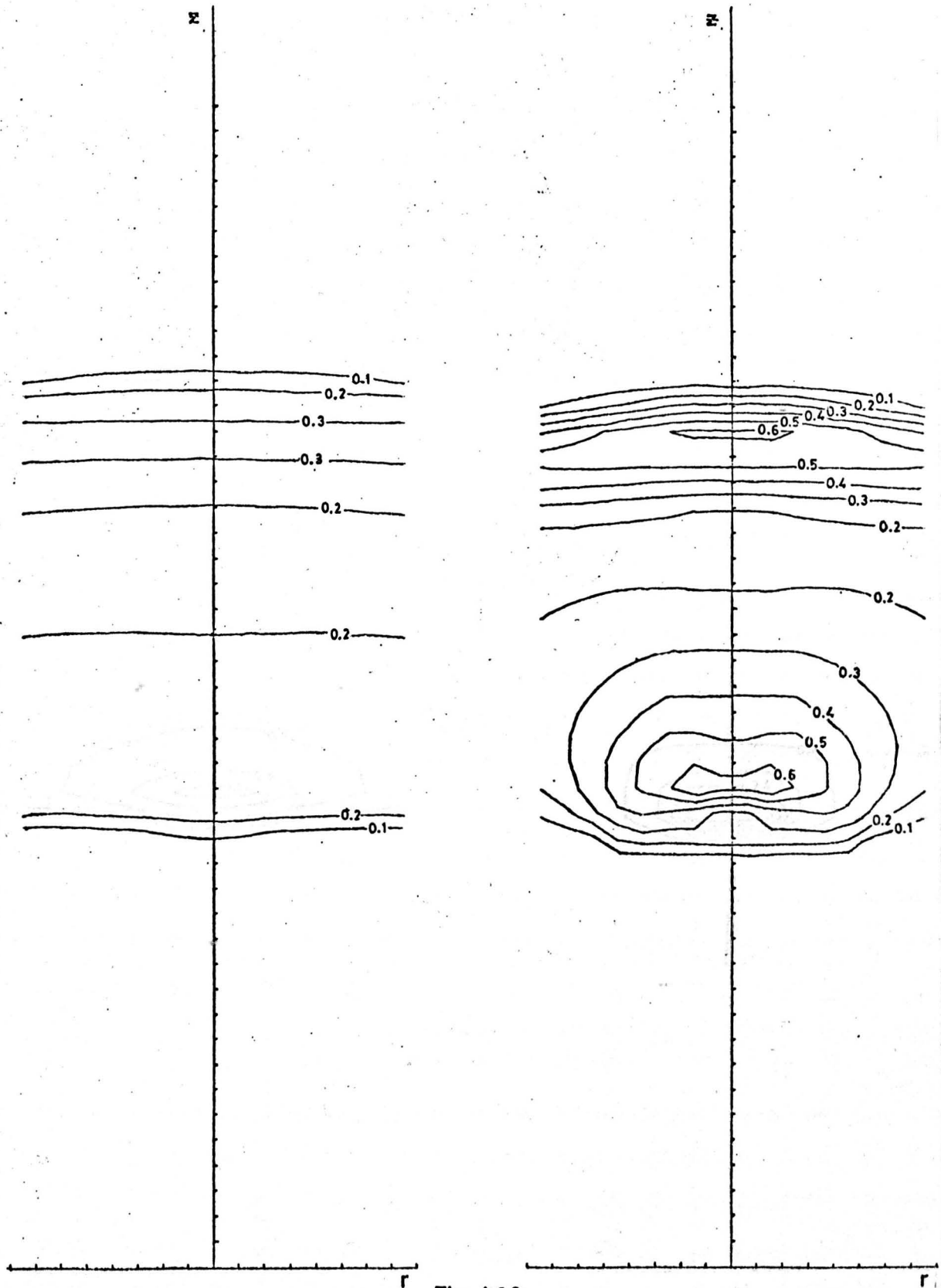

Fig 4.20

T^+ (°K × 10^6)

CO_2 Laser, $\phi = 5 \times 10^{18}$ c.g.s.

$\Delta r = 5 \times 10^{-4}$ cm, $\Delta z = 2 \times 10^{-3}$ cm.

t = 1 n.s.

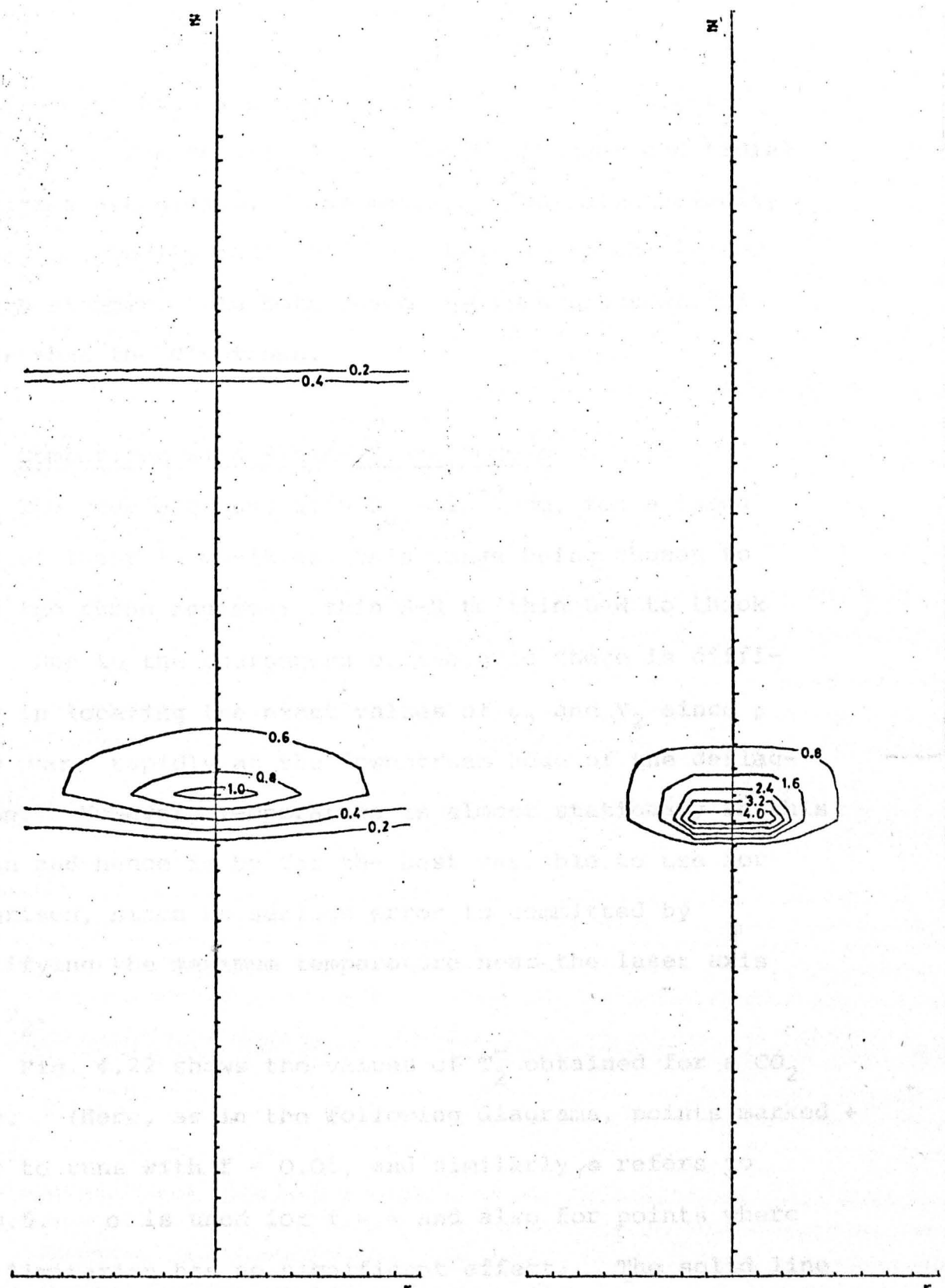

Fig 4.21
T^- ($°K \times 10^6$)
CO_2 Laser, $\phi = 5 \times 10^{18}$ c.g.s.
$\Delta r = 5 \times 10^{-4}$ cm, $\Delta z = 2 \times 10^{-3}$ cm.
t = 1 n.s.

with f = 0.05 have a predictable effect on the other variables. The density well is much stronger and radial velocities are higher. The maximum transverse velocity is only marginally increased but the rise to the latter is much steeper. In both cases the ions are some 80% cooler than the electrons.

(v) Comparison with Steady-State Models

The code was run, with $R_o = 10^{-3}$ cm, for a large range of laser intensities, this range being chosen to cover the three regimes: thin S-R to thin D-W to thick D-W. Due to the coarseness of the grid there is difficulty in locating the exact values of ρ_2 and v_2 since ρ and v vary rapidly at the downstream edge of the deflagration. However, temperature is almost stationary in this region and hence is by far the best variable to use for comparison, since no serious error is committed by identifying the maximum temperature near the laser axis with T_2.

Fig. 4.22 shows the values of T_2 obtained for a CO_2 laser. (Here, as in the following diagrams, points marked + refer to runs with f = 0.05, and similarly ⊕ refers to f = 0.5.. o is used for f = ∞ and also for points where flux limitation has no significant effect. The solid line indicates the theoretical result of the steady-state model). It can be seen that as expected, the thin S-R regime is followed closely at the lower laser intensities and the

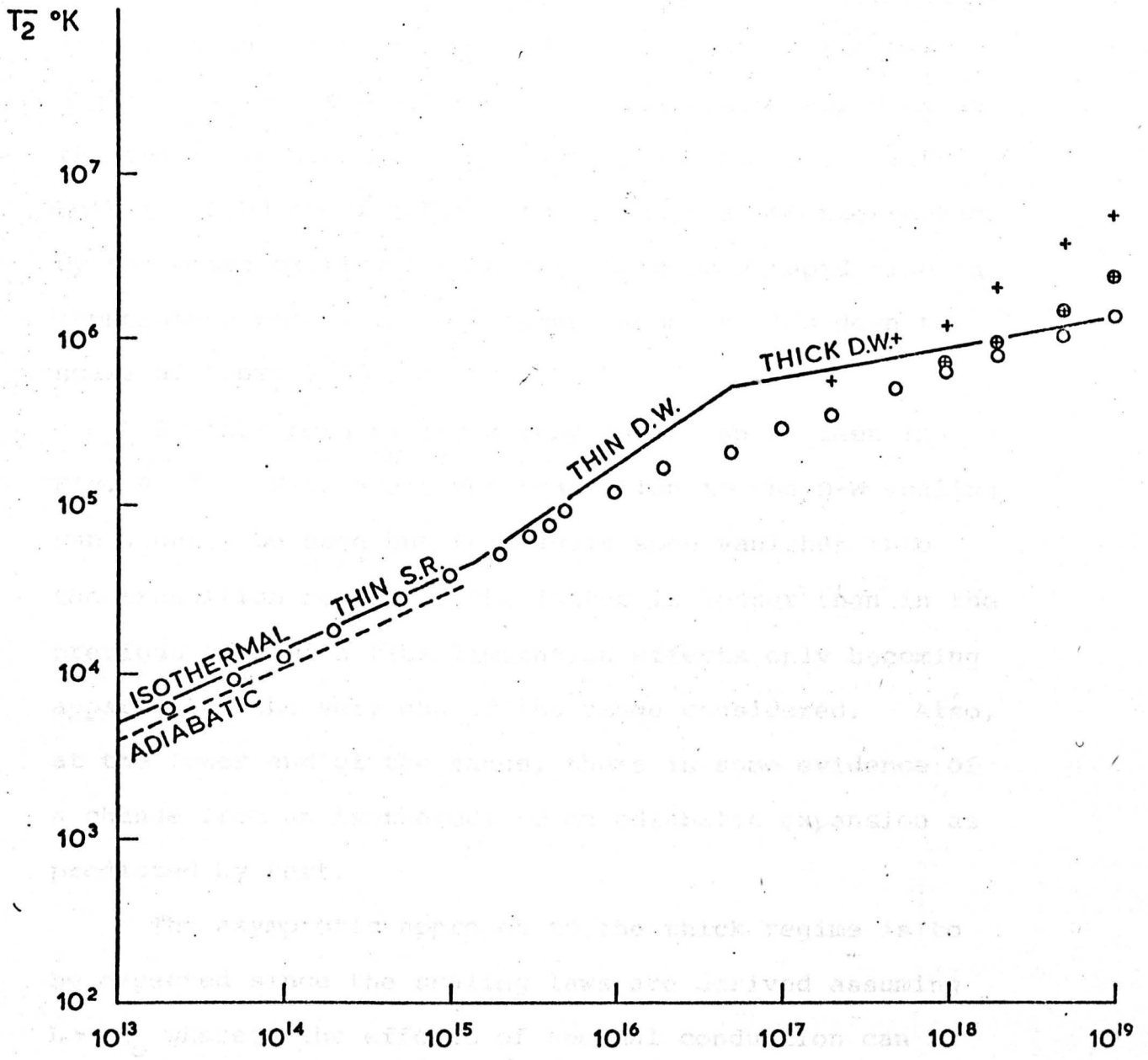

Fig. 4.22

Values of T_2^- obtained with a CO_2 laser ($R_o = 10^{-3}$ cm) compared with analytic result (solid line)
+ - f = 0.05, ⊕ - f = 0.5, O - f = ∞.

transition to thin D-W can be discerned. However with less than an order of magnitude increase in ϕ the D-W scaling is lost and a long transition region approaching the thick D-W regime asymptotically is entered. With both f = 0.05 and f = 0.5 this is again soon interrupted by the onset of flux limitation, causing a rapid rise in temperature which, in both cases, soon settles down to scale as about $\phi^{0.6}$.

Similar results for a ruby laser can be seen in Fig. 4.23. Here again the transition to the D-W scaling can clearly be seen but this again soon vanishes into the transition region. The latter is longer than in the previous case with flux limitation effects only becoming apparent at the very end of the range considered. Also, at the lower end of the range, there is some evidence of a change from an isothermal to an adiabatic expansion as predicted by Pert.

The asymptotic approach to the thick regime is to be expected since the scaling laws are derived assuming $L >> R_o$ whereas the effects of thermal conduction can be expected to appear gradually as L approaches and exceeds R_o. Hence it would appear that the above results confirm Pert's treatment of thermal conduction effects. It can also be seen that, due to flux limitation, it is unlikely that the true scaling laws of the thick regimes will be attained. However the transition region, with a scaling intermediate to the thin S-R and thick D-W should be

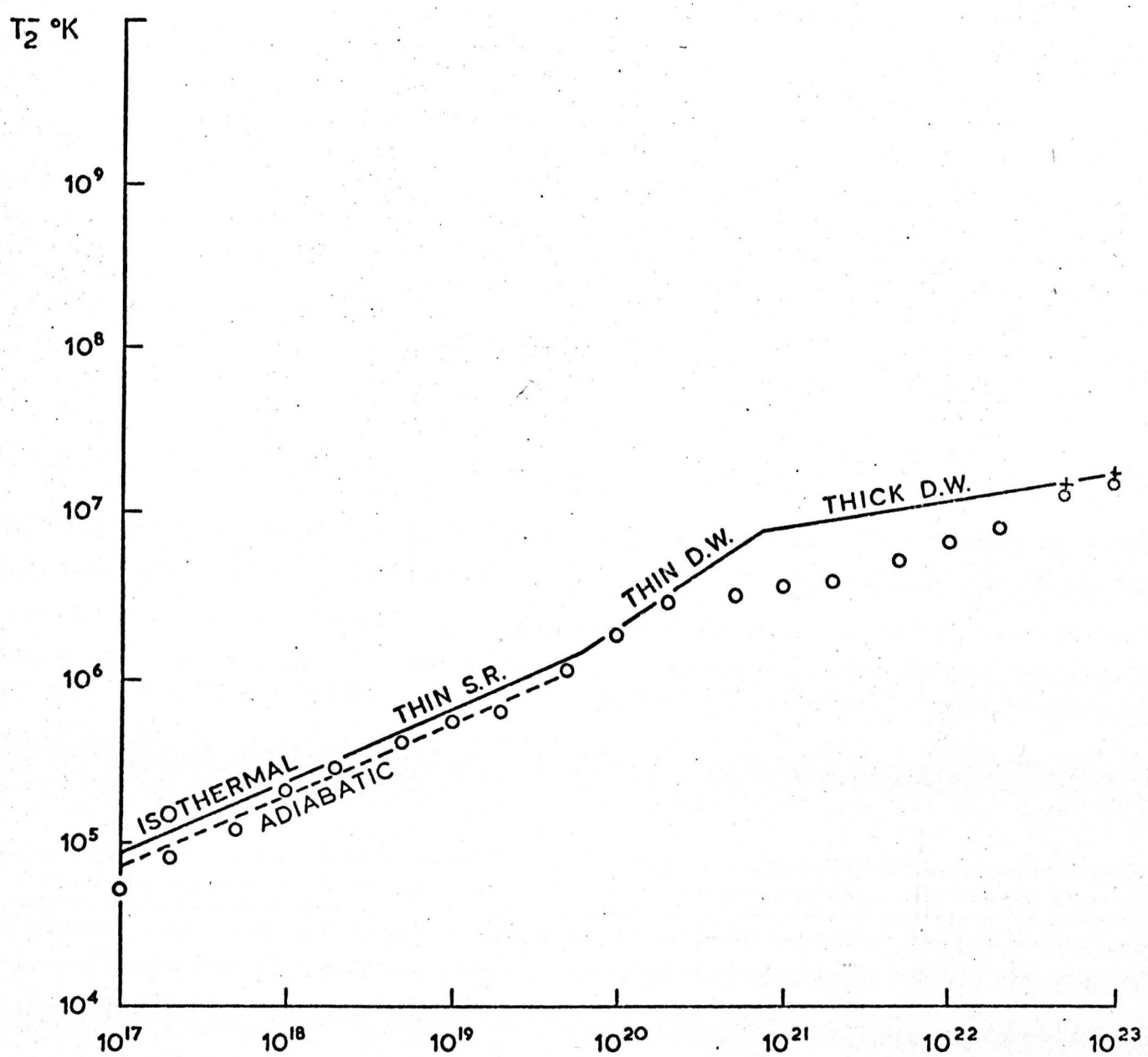

Fig. 4.23

Values of T_2^- obtained with a ruby laser ($R_o = 10^{-3}$cm) compared with analytic result (solid line)

+ - f = 0.05, o - f = ∞.

observable, and the encroachment of this region well into the thin D-W could explain why the scaling laws of the latter have not been observed experimentally. Such intermediate scaling laws have been observed by Dyer et al (3) using carbon and aluminium targets; however it should be noted that these were found over the whole range of powers considered and hence no transition from thin S-R was observed. Alternatively it should be noted that Rabeau et al (4), using a deuterium target have observed a transition from thin S-R to a region with a velocity scaling of 3/7 - even stronger than thin D-W. This, of course, could be due to the onset of flux limitation.

Although it is not possible to determine v_2 exactly, a rough idea of behaviour can be obtained by assuming velocity varies linearly across the maximum temperature cell. Values at the cell boundaries can then be calculated and give upper and lower limits for v_2. Fig. 4.24 shows the results obtained for the CO_2 laser with f = 0.05. In the thin S-R regime the values are again very near the theoretical line and there is even some evidence of change from isothermal to adiabatic expansion as the intensity decreases. As the transition to thick D-W is entered the behaviour becomes somewhat irregular and the $T^{\frac{1}{2}}$ scaling appears to be lost. However the general trend would seem to be as expected. As the flux limiter starts to have effect at higher intensities the $T^{\frac{1}{2}}$ scaling

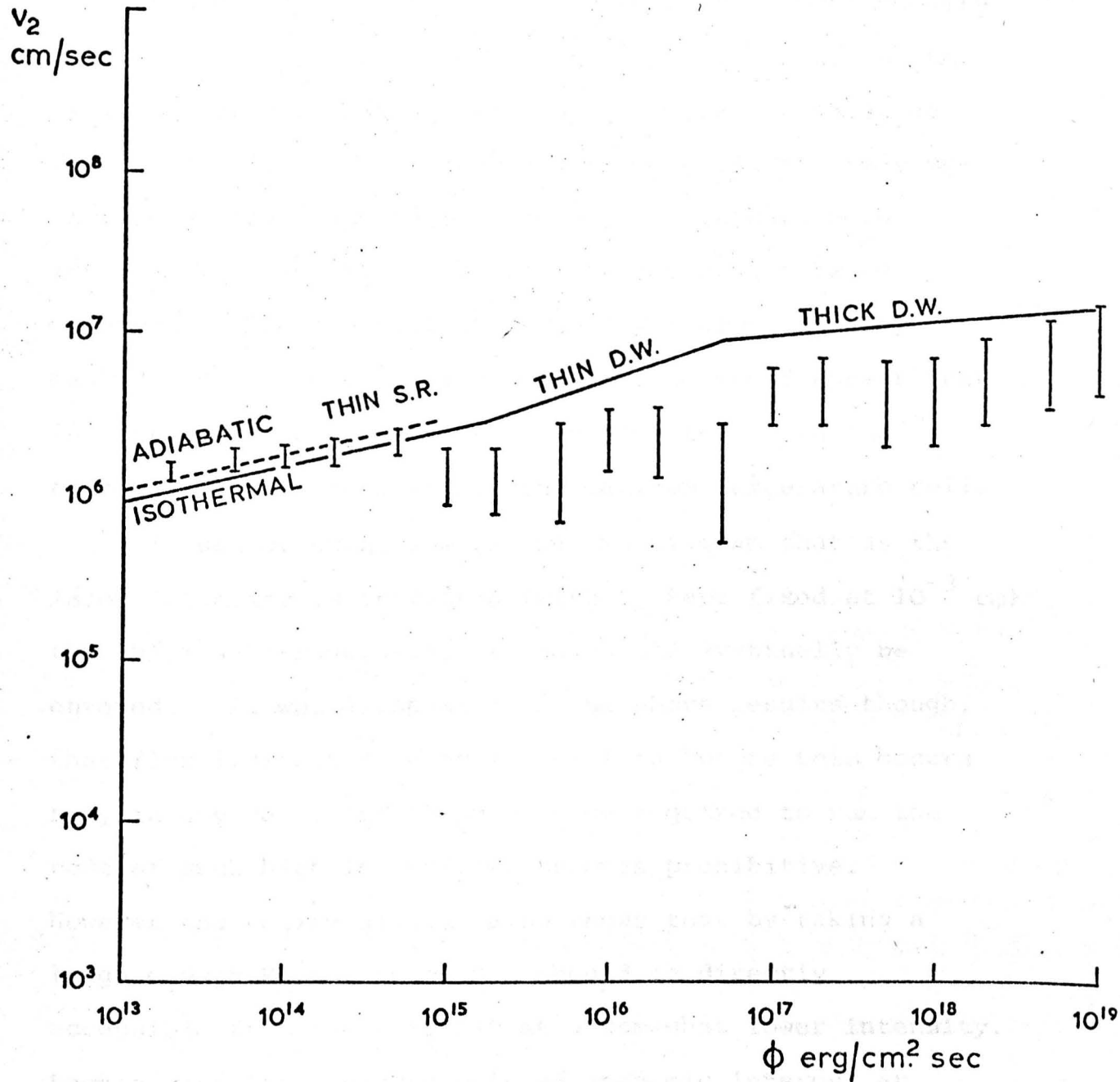

Fig. 4.24

Range of velocity obtained across the maximum temperature cell compared with analytic values of v_2 (solid line). CO_2 laser ($R_o = 10^{-3}$ cm), f = 0.05.

appears to be recovered.

A similar procedure can be applied to number density with the harmonic mean being used to obtain values at the cell boundaries. Fig. 4.25 shows the results obtained for the CO_2 laser. In the thin S-R the values are somewhat lower than expected; however, and perhaps more importantly, the correct scaling is apparently being observed. The transition to the D-W regimes is very marked and as the intensity increases it would appear that in most cases the behaviour is as expected, with the critical density well within the maximum temperature cell.

It can be seen from the regime diagram that as the laser intensity is increased (with R_o kept fixed at 10^{-3} cm) the thick self-regulating regime should eventually be entered. It would appear from the above results though, that flux limitation takes effect long before this occurs and, in any case, the computer time required to run the code at such high intensities becomes prohibitive. However the regime diagram also shows that by taking a large enough R_o the thick S-R should be directly accessible from the thin S-R at a somewhat lower intensity. Such a case is of course only of academic interest at present but it does serve to test the theory. Fig. 4.26 shows the electron temperatures obtained with a ruby laser with R_o = 100 cm. It can be seen that in the absence of flux limitation the correct scaling laws are followed,

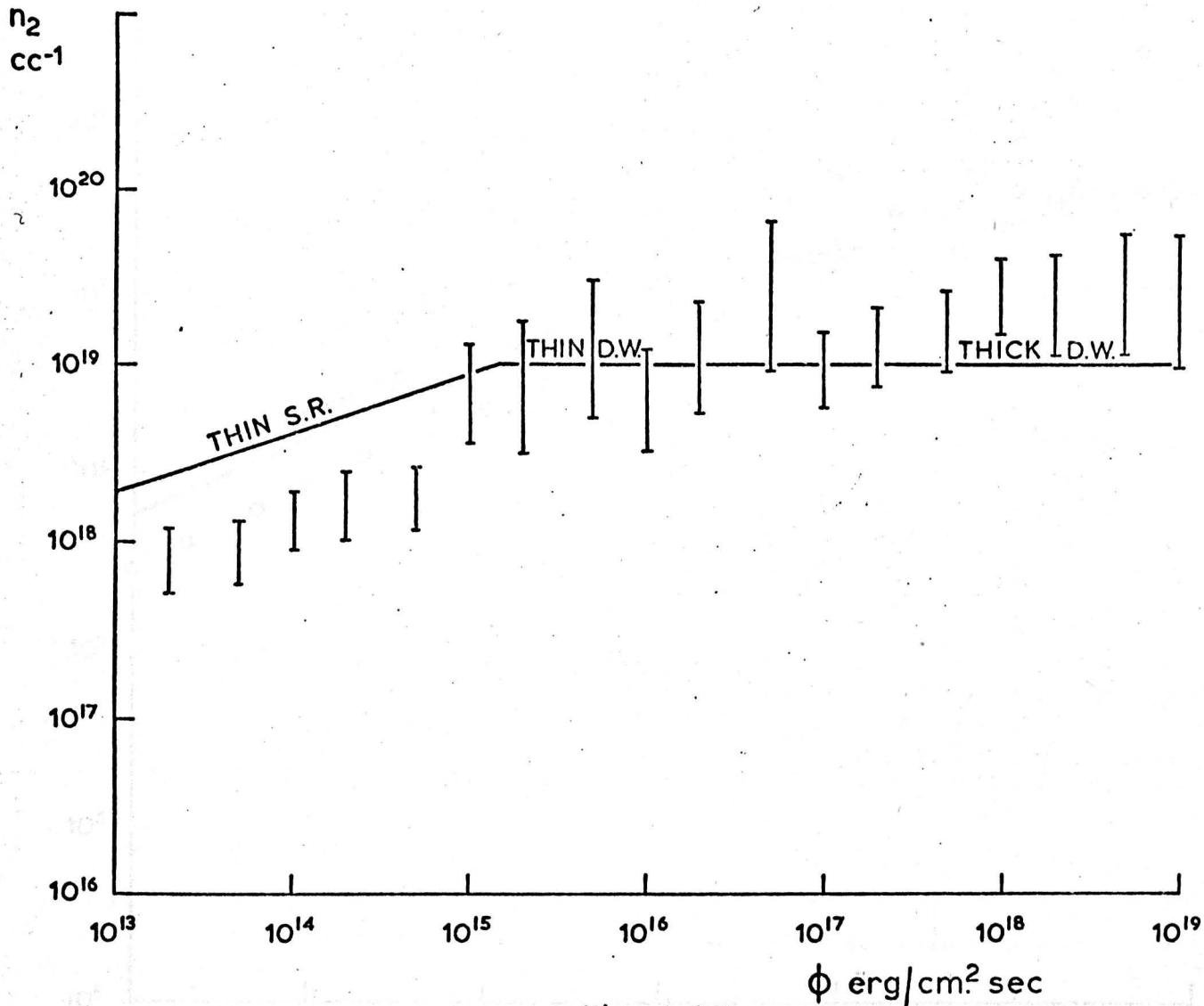

Fig. 4.25

Range of density obtained across the maximum temperature cell compared with analytic values of n_2 (solid line). CO_2 laser ($R_o = 10^{-3}$ cm).

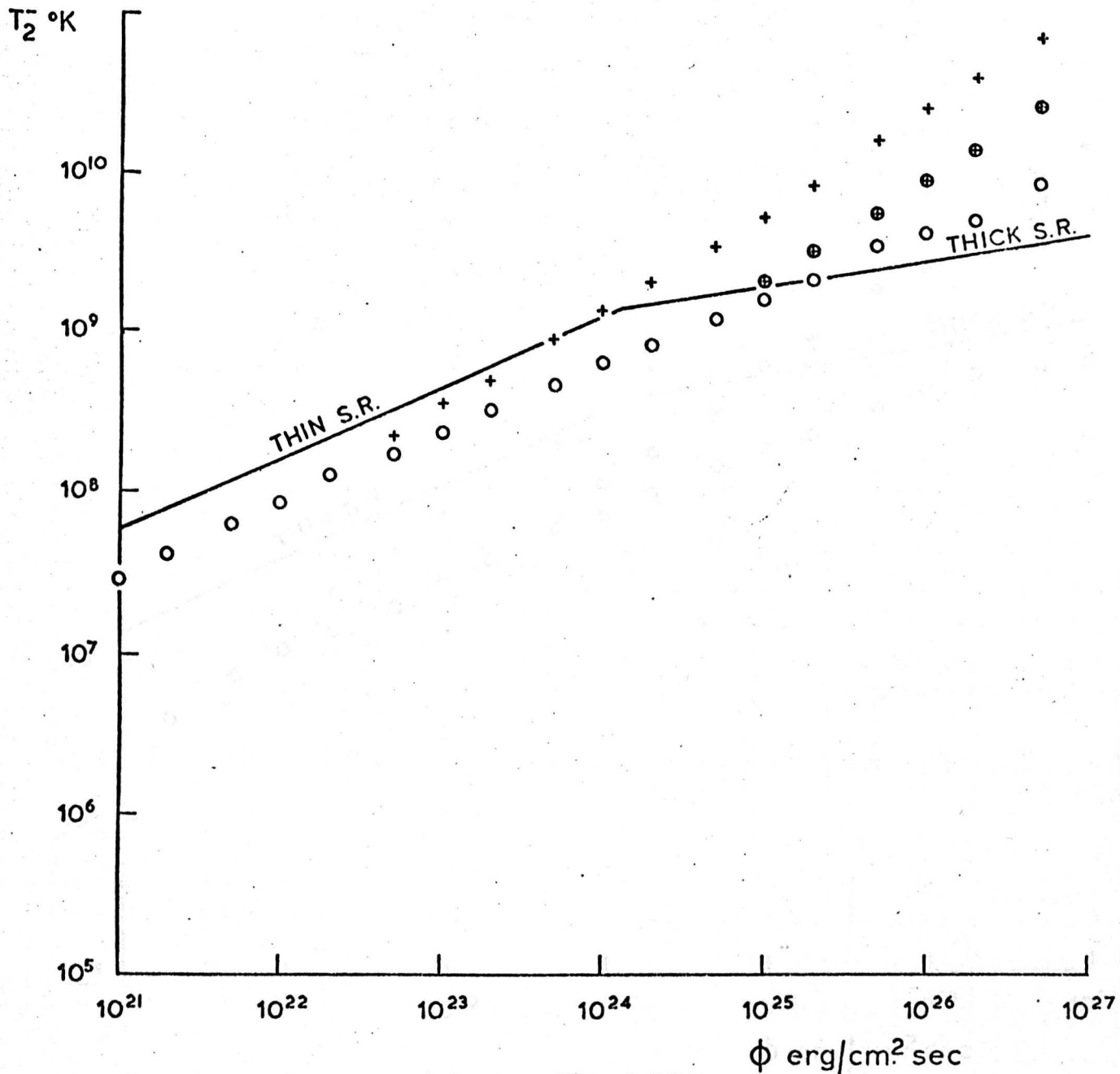

Fig. 4.26

Values of T_2^- obtained with a ruby laser (R_o = 100 cm) compared with analytic result (solid line).

+ - f = 0.05, ⊕ - f = 0.5, o - f = ∞.

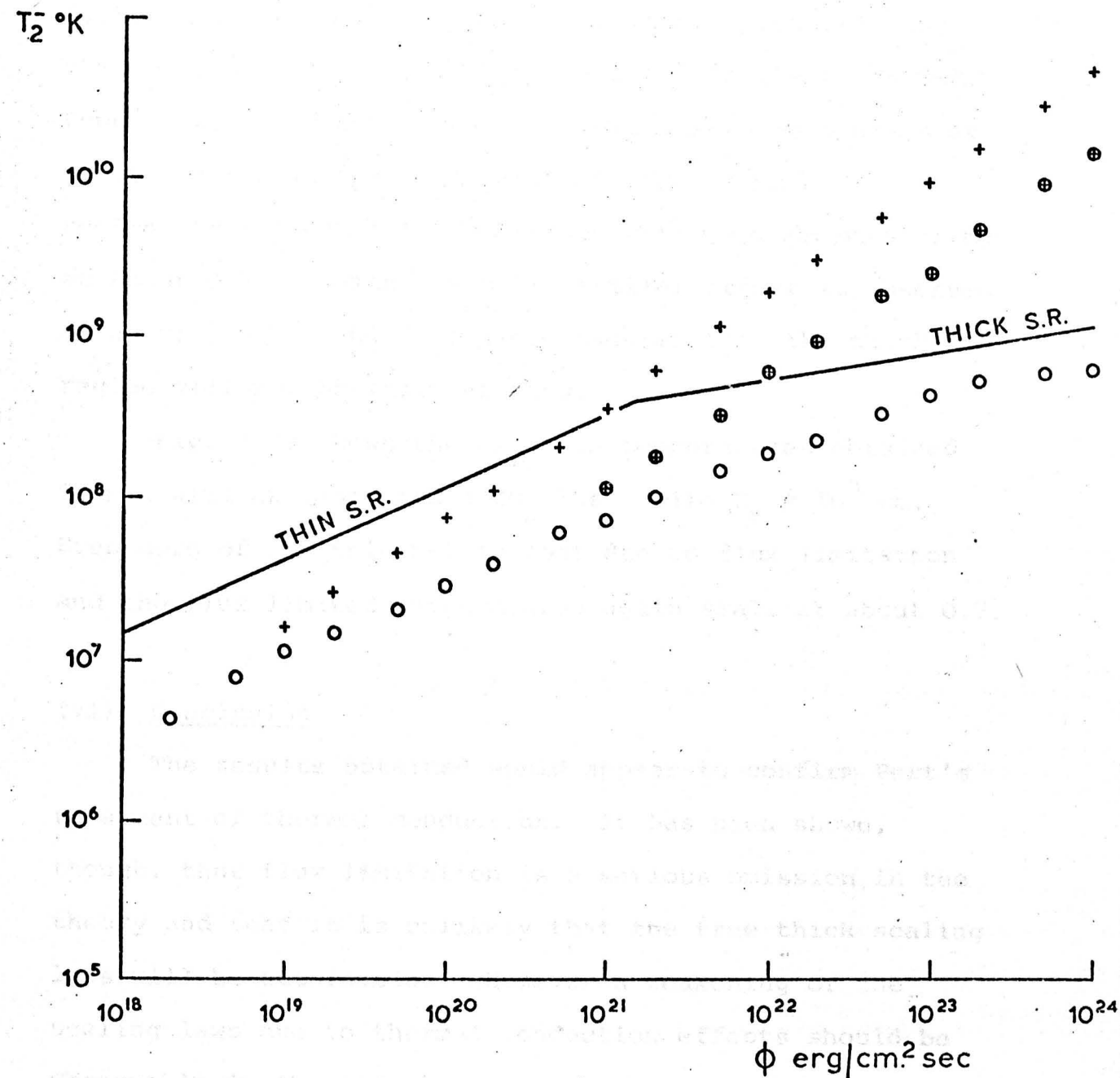

Fig. 4.27

Values of T_2^- obtained with a CO_2 laser ($R_o = 10^3$ cm) compared with analytic result (solid line). + - f = 0.05, ⊕ - f = 0.5, o - f = ∞.

although values are somewhat lower than expected in the thin S-R, and similarly somewhat higher in the thick S-R. However with f = 0.05 the flux limit starts to operate at about $\phi = 5 \times 10^{22}$ - still well within the thin S-R regime - and leads into a region with temperature scaling at about 0.7. With f = 0.5 a similar effect is observed at about $\phi = 5 \times 10^{24}$ and hence ensures that the thick S-R regime will not be fully entered.

Fig. 4.27 shows the electron temperatures obtained from a similar case with a CO_2 laser with $R_o = 10^3$ cm. Even more of the thin S-R is lost due to flux limitation and the flux limited temperatures again scale at about 0.7.

(vi) Conclusion

The results obtained would appear to confirm Pert's treatment of thermal conduction; it has been shown, though, that flux limitation is a serious omission in the theory and that it is unlikely that the true thick scaling laws will be attainable. However a weakening of the scaling laws due to thermal conduction effects should be observable in the asymptotic approach to thick D-W, and, due to this transition region, the thin D-W scaling is restricted to a very short range of intensity. It would appear that effects associated with thick S-R are completely lost due to flux limitation. Some evidence has been found that Pert's modification of thin S-R is correct.

CHAPTER 5

The effects due to refraction of the laser beam are now examined, using a geometrical optics approximation. A computer code is developed that traces ray paths, and calculates energy absorption, for any given density and temperature distribution. Calculations are restricted to two dimensions since, in the cylindrically symmetric situation, the ray path will be in a single plane. A number of test cases, with known analytical solutions, are used to demonstrate the accuracy of the code.

(i) Ray Tracing

The density and temperature distributions are defined on a rectangular grid, and the ray tracing calculations are then performed using a superimposed triangular mesh. The relationship between these is shown in Fig. 5.1. As can be seen, the tracing cells taken in pairs (i,j,I) and (i,j,II) form the complementary cells of the original grid. The density gradient within a tracing cell is assumed to be constant. The use of triangular cells allows this density gradient to be defined simply and uniquely, and also provides continuity along the cell boundaries.

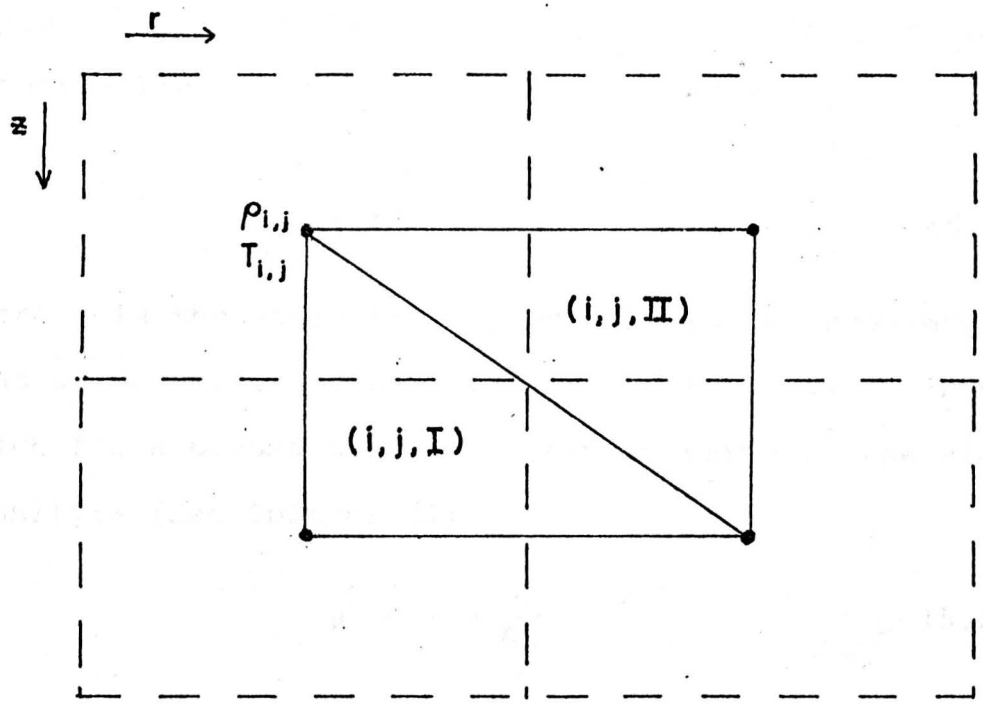

Fig. 5.1

Relationship between ray-tracing cells and the cells of the original grid.

The ray path in a constant density gradient is a parabola, as will now be demonstrated. Along the ray path Snell's law gives:

$$\mu \sin \lambda = \mu_o \qquad (5.1)$$

where λ is the angle the ray makes with the x direction - that of decreasing density, μ is the refractive index, which for a plasma can be written in terms of the electron density:- (See Spitzer (1))

$$\mu^2 = 1 - \frac{n}{n_c} \qquad (5.2)$$

and μ_o is the refractive index at $\lambda = \frac{\pi}{2}$. Taking the x-axis in the direction of decreasing density, the density is given by:-

$$n = n_o - gx \qquad (5.3)$$

where g is the magnitude of the density gradient, and n_o is the density at $\mu = \mu_o$. Hence from (5.2) and (5.3):-

$$\mu^2 = \mu_o^2 + \mu_1^2 x \qquad (5.4)$$

where

$$\mu_1^2 = \frac{g}{n_c} \qquad (5.5)$$

The equation of the ray path is given by:-

$$\frac{dy}{dx} = \tan \lambda = \left(\frac{\mu_o^2}{\mu^2 - \mu_o^2} \right)^{\frac{1}{2}} = \frac{\mu_o}{\mu_1} \left(\frac{1}{x} \right)^{\frac{1}{2}} \qquad (5.6)$$

Taking the origin at $\mu = \mu_o$ and integrating, gives the parabola:-

$$y^2 = 4\left(\frac{\mu_o}{\mu_1}\right)^2 x \qquad (5.7)$$

Since this has a particularly simple form, the ray tracing calculations are performed relative to the local x and y axes, even though these will in general vary from cell to cell.

As the ray enters a cell, the point of entry relative to the z and r axes will be known, together with the angle ϕ_I that the ray makes with the z-axis.* The magnitude of the density gradient within the cell, and the angle Ψ that the x-axis makes with the z-axis, can be calculated, and for (i,j,I) are given by:-

$$g = \left[\left(\frac{n_{i+1,j+1} - n_{i+1,j}}{\Delta r}\right)^2 + \left(\frac{n_{i+1,j} - n_{ij}}{\Delta z}\right)^2\right]^{\frac{1}{2}} \qquad (5.8)$$

and

$$\tan \Psi = - \frac{(n_{i+1,j+1} - n_{i+1,j})\Delta z}{(n_{i+1,j} - n_{i,j})\Delta r} \qquad (5.9)$$

and similarly for (i,j,II). A knowledge of ϕ_I and Ψ provides a value for λ_I, the angle that the ray makes with the x axis, at the point of entry. Again values of λ are taken between $-\pi$ and π, values with modulus greater than

---

* Values of ϕ are taken between $-\pi$ and π. Angles with modulus greater than $\frac{\pi}{2}$ represent a ray travelling in the negative z direction.

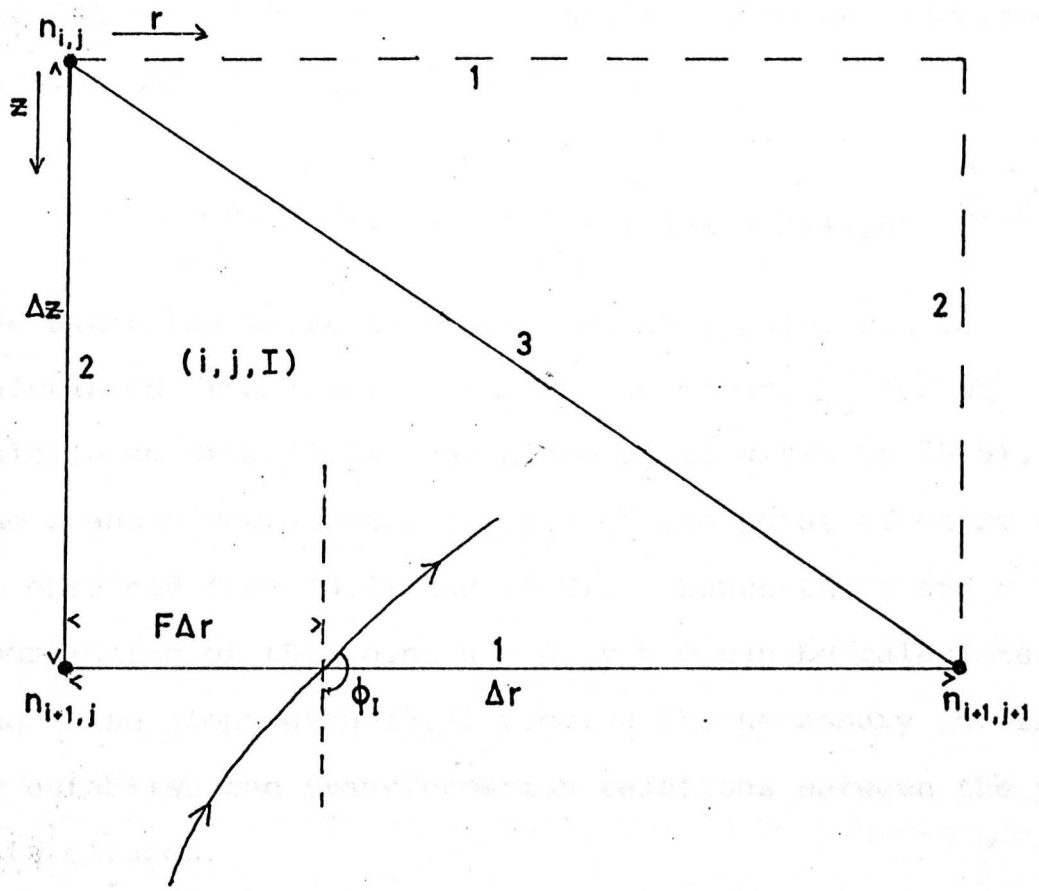

Fig. 5.2

See text

$\frac{\pi}{2}$ representing rays moving towards their turning point. The density at the point of entry can also be calculated, and for the case shown in Fig. 5.2 is: -

$$n_I = n_{i+1,j} + F.(n_{i+1,j+1} - n_{i+1,j}) \quad (5.10)$$

and hence the refractive index at this point can be calculated from (5.2). This being known, μ_o can be calculated from (5.1), and since μ_1 is given by (5.5), the x and y coordinates (x_I, y_I) of the point of entry can be obtained from (5.4) and (5.7). Hence the z and r coordinates of the point x = 0, y = 0 can be calculated, and these along with (5.9) provide the necessary information to establish the transformation relations between the two sets of axes.

The tangent to the ray path at the entry point P_I is now constructed across the cell to locate the point P_S (see Fig. 5.3). It is established whether the ray will turn in a clockwise or anticlockwise direction (if $\lambda_I > 0$ the turning is clockwise, and is anticlockwise if $\lambda_I < 0$. The case when $\lambda_I = 0$ will be dealt with later) and then the cell boundary is transversed in the same direction, from P_S to P_I, searching for intersections with the ray path. The first such intersection to be encountered is the true exit point of the ray. Hence in Fig. 5.3, if the ray is known to be turning anticlockwise, the section $P_S P_A$ would be first tested for intersections. If none are found then $P_A P_B$ would be similarly tested, and

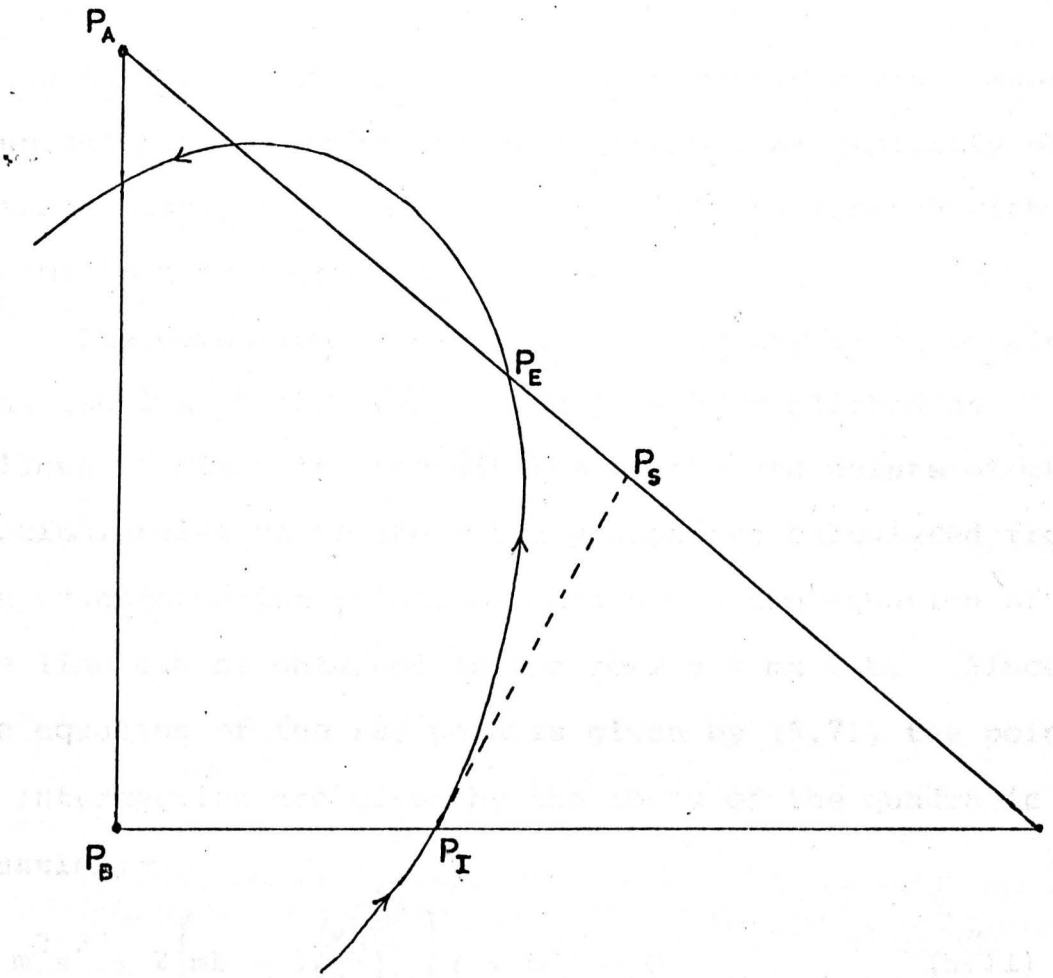

Fig. 5.3

See text

so on to $P_B P_I$. The above procedure provides that, even when the ray re-enters the cell giving a multiplicity of intersections, the true exit point will be located with the minimum of computation.

The detection of intersections on any given straight line section of the cell boundary is accomplished as follows. First the coordinates of the end points of the section, relative to the x and y axes are calculated from the transformation relations, and hence the equation of the line can be obtained in the form $y = mx + b$. Since the equation of the ray path is given by (5.7), the points of intersection are given by the roots of the quadratic equation:-

$$m^2x^2 + 2\left[mb - 2\left(\frac{\mu_o}{\mu_1}\right)^2\right]x + b^2 = 0 \qquad (5.11)$$

If one of the roots of (5.11) lies between the x coordinates of the end points of the section being tested, then an intersection point has been located and if the correct procedure has been followed this will be the exit point of the ray. If both roots of (5.11) are within the required range then the true exit point will be the one first encountered when tracing the cell boundary from P_S to P_I in the appropriate direction. If (5.11) has equal roots then the point of intersection is ignored, since the ray has not left the cell and the true exit point will be found further round the boundary. (The one exception

to this is when the section being tested is the cell face through which the ray entered. Due to rounding errors in the computation it is possible that a ray might enter a cell through a face that is almost tangential to the ray path, and then when the calculations are performed in this new cell that same face is found to be exactly tangential, i.e. (5.11) has equal roots. In this case the point of intersection must be considered valid, and the ray leaves the cell through the point of entry). If the exit point is found to lie on a cell corner then it is moved fractionally along one of the adjacent faces. Also, to avoid trouble from rounding errors, it is necessary to allow exit points lying just outside the end points of each face, these again being moved fractionally to place them within the required range.

The above procedure uses solely the x-coordinate for testing purposes. However, in practice, to keep the accuracy as high as possible, the y-coordinate is used in an analogous fashion for cases when $m > 1$. Also, of course, special allowance must be made for the cases when m is zero or infinite.

There are a number of cases when the ray path will approximate closely to a straight line. These are:-

a) x_I or y_I $>> \overline{P_I P_S}$

b) $g \simeq 0$

c) $\lambda_I \simeq 0$ or $|\lambda_I| \simeq \pi$

If any of these are true then P_S can be immediately taken to be the exit point, the one exception being when the density at P_S is found to be greater than n_c - in this case the ray is reflected from the point P_I (i.e. P_I is the exit point).

The exit point having been located, the value of λ_E, the angle the ray makes with the x-axis on leaving the cell, can be calculated using (5.1) and (5.4). However this only gives a value in the first quadrant, and the true angle must be obtained by examining the value of λ_I. If the ray has passed through the point $x = 0$, $y = 0$ while within the cell then λ must have moved from the quadrant $\frac{\pi}{2} < \lambda < \pi$ to $-\pi < \lambda < -\frac{\pi}{2}$ or vice-versa. In all other cases (apart from the reflection mentioned above) λ_E and λ_I must lie in the same quadrant. The angle that the ray makes with the z-axis can now be calculated, and, with the fractional distance of the exit point along the cell face, provides the necessary information for the computation to proceed into the next cell.

(ii) Absorption

The electron density and temperature at the entrance and exit points of a ray can be calculated as in (5.10), and hence the absorption coefficients α_I and α_E, at these points can be obtained from (2.8). The absorption coefficient along the ray path within the cell is then

assumed to be constant, having the value:-

$$\alpha = (\alpha_I + \alpha_E)/2 \qquad (5.12)$$

The absorption integral for that section of ray is then given by:-

$$Q = \int \alpha \, ds = \alpha \left[\sqrt{x\left(x + \left(\frac{\mu_o}{\mu_1}\right)^2\right)} + \left(\frac{\mu_o}{\mu_1}\right)^2 . \sinh^{-1}\left(\frac{\mu_1}{\mu_o} . \sqrt{x}\right) \right]_{x_I}^{x_E}$$

(5.13)

where x_I and x_E are the x-coordinates of the entrance and exit points. The power e_I of the ray on entering the cell and the power e_E on leaving are then related by:-

$$e_E = e_I \exp(-Q) \qquad (5.14)$$

and the energy per unit time absorbed from the ray as it crosses the cell is:-

$$e = e_I - e_E \qquad (5.15)$$

Since e_E for the cell being traversed becomes e_I for the next cell entered, once the initial power of the ray has been assigned, absorption along the whole ray path can be calculated using (5.14) and (5.15).

The ray model of a laser beam used in a cylindrical geometry is shown in Fig. 5.4. Here, ray n = 1 is taken to be on the axis r = 0 and hence is assumed to suffer no refraction, being reflected at the critical density. The other rays are initially spaced at a constant distance d

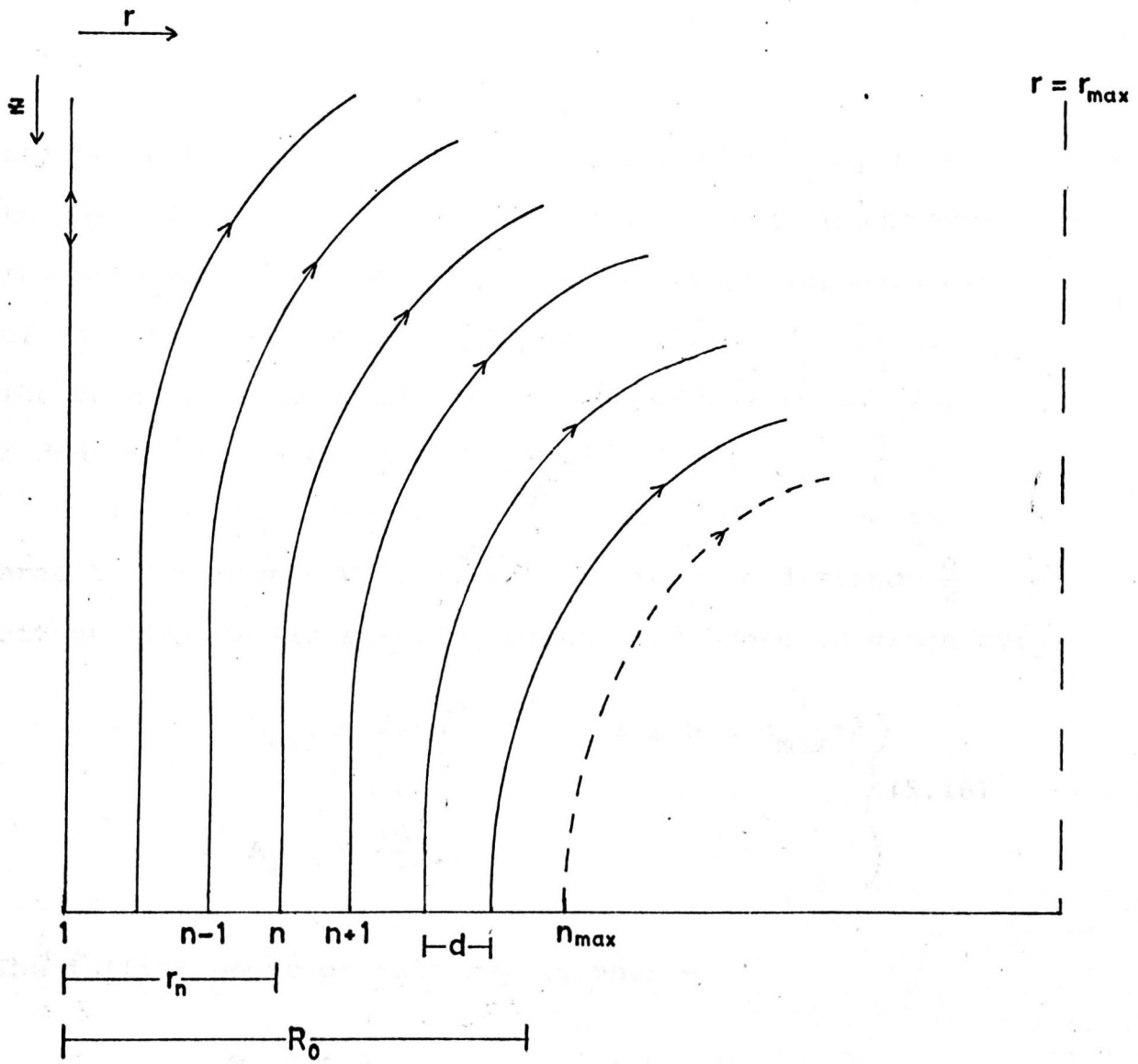

Fig. 5.4

Ray model of a laser beam

and hence the initial radial distance of n^{th} ray from the axis is (n-1)d. The ray $n = n_{max}$ is an imaginary ray with zero power which serves to define the boundary of the laser beam during the absorption calculation. The value of d is chosen so that the required initial radius of the laser beam R_o is given by $(n_{max} - \frac{3}{2})d$.

Initially, each real ray is assumed to have an area A_n associated with it which extends a distance $\frac{d}{2}$ either side of its starting point, and hence is given by:-

$$\left.\begin{aligned} A_{n+1} &= 2\pi n d^2 \qquad 1 \leq n < n_{max}-2 \\ A_1 &= \frac{\pi d^2}{4} \end{aligned}\right\} \quad (5.16)$$

The initial power of each ray is then:-

$$\left.\begin{aligned} e_n &= \phi_o A_n \qquad 1 \leq n < n_{max} \\ e_{n_{max}} &= 0 \end{aligned}\right\} \quad (5.17)$$

where ϕ_o is the intensity of the laser. The equations (5.17) supply the necessary initial conditions for (5.14) and (5.15) to be applied.

(iii) Energy Assignment

A system of assigning absorbed energy to the cells of the original rectangular grid must now be devised. The problem is made more complex by the fact that, unless an extremely large number of rays are employed, there will be some tracing cells that, although they are within the refracted laser beam, do not have rays passing through them. In addition rays can cross, and hence the initial ordering of the rays will be lost, and initially adjacent rays can become widely separated. Hence it is not correct to simply assign the energy lost by a ray in traversing a tracing cell to that cell, and then interpolate onto the original grid; the system must include some method of spreading the absorbed energy over the cells lying between each initially adjacent pair of rays.

The method proposed here is in two stages. Firstly, energy is assigned to the intersections $C_{i,n}$ and $C_{i,n+1}$ of the nth and (n+1)th rays with each line of cell centres of the original grid. Secondly, half of the total energy assigned to $C_{i,n}$ and $C_{i,n+1}$ is spread along the section of the ith row contained between these points, such that each cell or part of a cell within this region receives the same energy per unit volume. (This is the principle of the second stage. However the real situation is not quite as simple, as will become clear later.) It is clear that each ray intersection, with the exception of those

of the first ray, will enter the computation twice, since $C_{i,n}$ will also be paired with $C_{i,n-1}$. After a ray has crossed the ith row it may turn with respect to the z-axis and hence cross the ith row again. When this distinction is important the intersections of the incoming and outgoing sections of the ray will be referred to as $C_{i,n}^{(IN)}$ and $C_{i,n}^{(OUT)}$ respectively; where the meaning is obvious the suffices (IN) and (OUT) will be omitted. Other variables will be treated in the same fashion.

Stage I (see Fig. 5.5)

The power $W_{i+\frac{1}{2},n}$ lost by the incoming nth ray crossing between the i+1th and ith row can be calculated. The energy per unit time assigned to $C_{i,n}$ is then:-

$$E_{i,n} = \tfrac{1}{2}(W_{i+\frac{1}{2},n} + W_{i-\frac{1}{2},n}) \qquad (5.18)$$

If the ray, having crossed the ith row, does not reach the i-1th row, but turns and recrosses the former, then the power lost by the ray in this region is equally divided between the points $C_{i,n}^{(IN)}$ and $C_{i,n}^{(OUT)}$. The calculation for the outgoing ray can then proceed in an analogous fashion to the above.

If an incoming ray crosses the ith row and then leaves the grid via the boundary $r = r_{max}$ before reaching the i-1th row, half of the power absorbed in this region is assigned to the point $C_{i,n}^{(IN)}$. The remaining half is assigned to either the point $(i-1,j_{max})$ or the point (i,j_{max}) whichever is the closest to the exit point of the ray, the chosen point then being designated as either $C_{i-1,n}^{(IN)}$

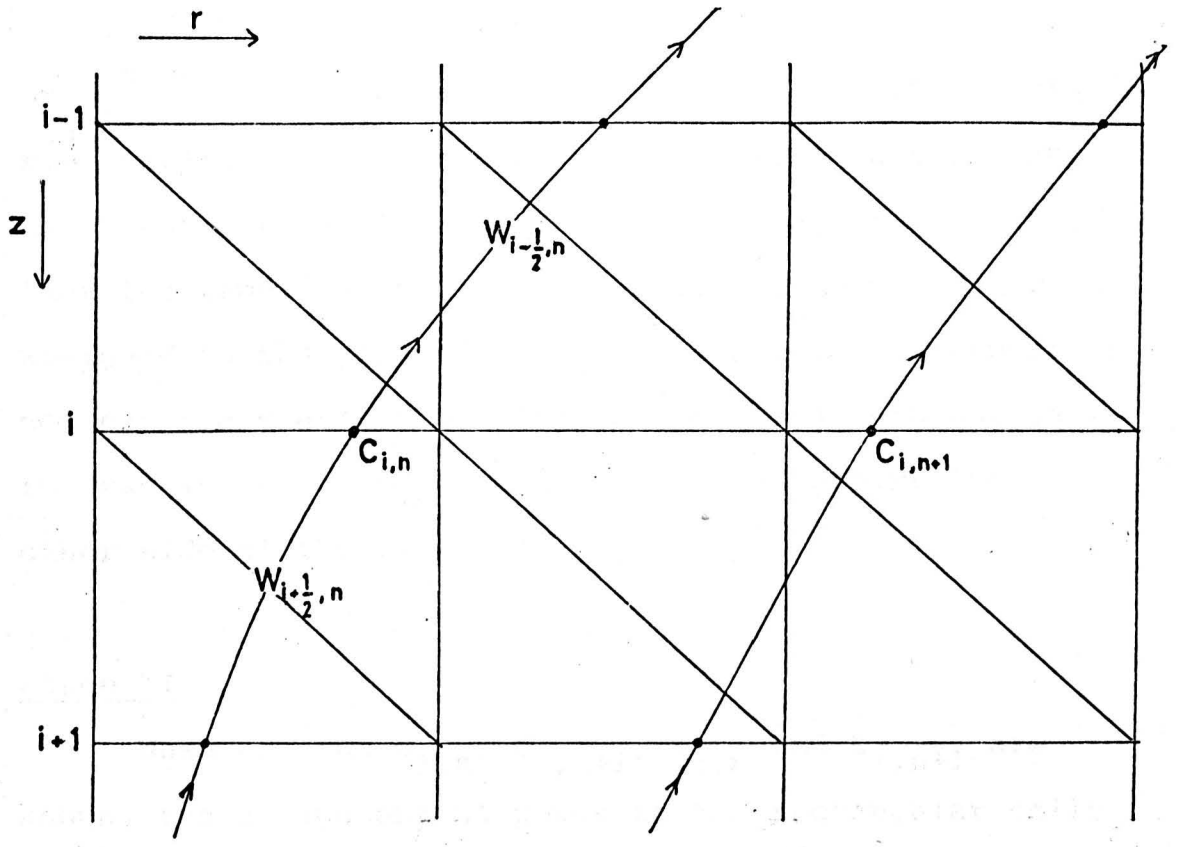

Fig. 5.5

Assignment of absorbed energy in stage I.

or $C_{i,n}^{(OUT)}$ as is appropriate. In the case of an outgoing ray leaving the grid via $r = r_{max}$ between rows i-1 and i the treatment is the same as above, with the exception that the remaining half of the absorbed power is always assigned to the point (i,j_{max}). A similar treatment is not necessary at r = 0, since on reaching this boundary the ray is reflected, becoming its counterpart from the other side of the axis.

Stage II

When all the $C_{i,n}$, $C_{i,n+1}$, $E_{i,n}$ and $E_{i,n+1}$ are known, the assignment of power to the rectangular cells between the rays n and n+1 can proceed. First it is necessary to establish a pairing of the intersections on each row. Complications arise here because one of the rays may turn before the other, or one or both rays may leave the grid via $r = r_{max}$, and hence the following procedure is suggested. First the $C_{i,n}^{(IN)}$ are paired with the $C_{i,n+1}^{(IN)}$ wherever they exist, and similarly the $C_{i,n}^{(OUT)}$ are paired with the $C_{i,n+1}^{(OUT)}$. The remaining $C_{i,n}^{(IN)}$, if any, are paired with the $C_{i,n}^{(OUT)}$ where they exist and are still unpaired, or similarly the $C_{i,n+1}^{(IN)}$ are paired with the $C_{i,n+1}^{(OUT)}$. Finally any remaining unpaired intersections are paired with points on $r = r_{max}$ which are assumed to have zero assigned power. To make the above clear Fig. 5.6 shows a number of typical configurations; the arrowed

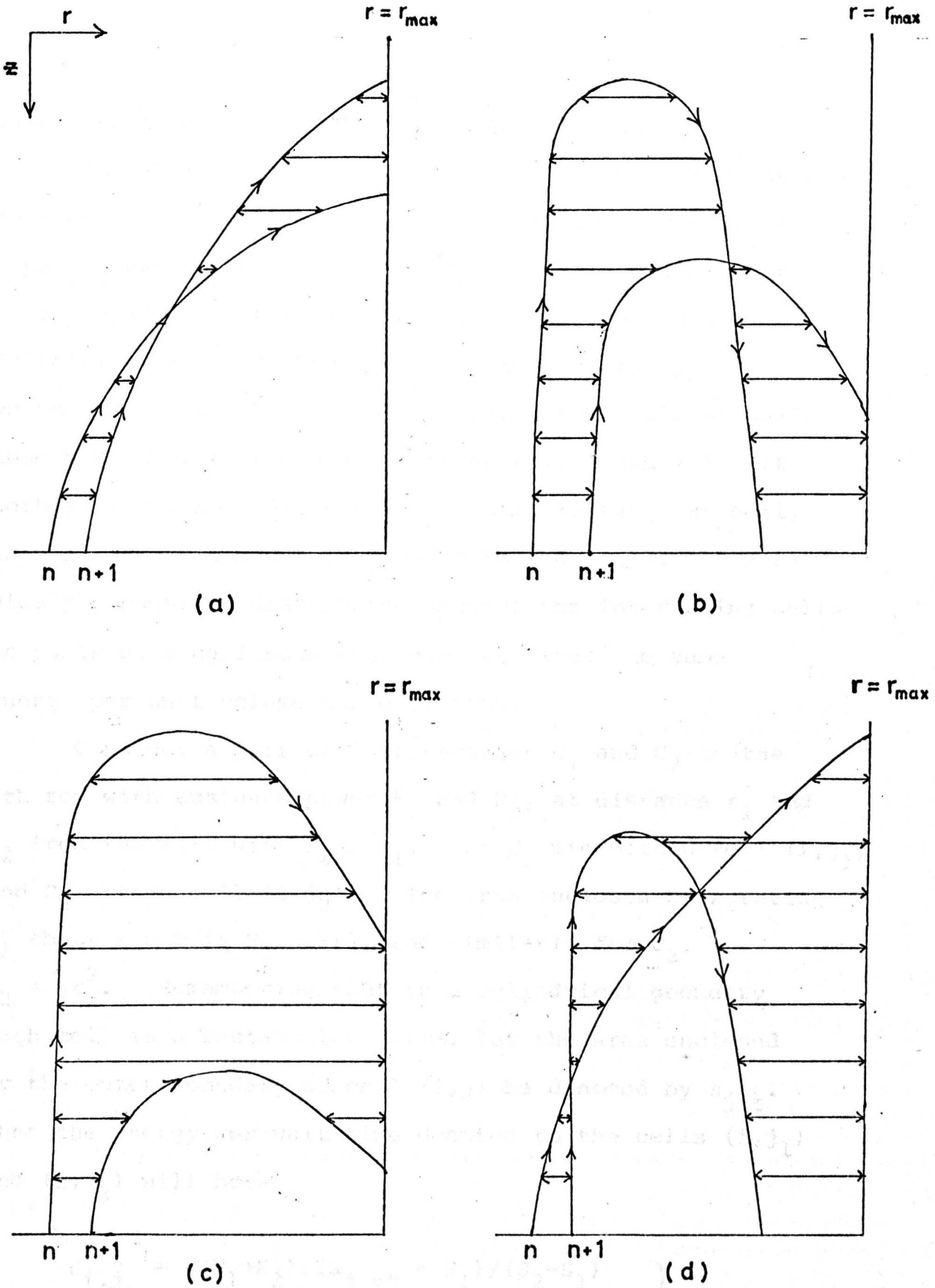

Fig. 5.6

Pairing of intersections for stage II of energy assignment

lines indicate intersections that are paired.

The above having being completed, each pair of intersections can be treated separately, with each member of a pair donating half of its absorbed power to the intervening space. (There is one exception. Due to the cylindrical geometry, the intersections of ray n = 1, which will always lie on r = 0, donate the whole of their absorbed power to the space between rays 1 and 2.) If both intersections lie within the same rectangular cell, then all of this power is donated to that cell. Otherwise the power is distributed amongst the intervening cells or parts of a cell such that each receives the same energy per unit volume per unit time.

Consider a pair of intersections C_1 and C_2 on the ith row with assigned power E_1 and E_2, at distance r_1 and r_2 from the axis with $r_2 > r_1$. Let C_1 lie within cell (i,j_1) and C_2 within cell (i,j_2). The area enclosed by rotating C_1 about r = 0 is $S_1 = \pi r_1^2$, and similarly for C_2, $S_2 = \pi r_2^2$. Remembering that in a cylindrical geometry each cell is a rectangular torus, let the area enclosed by the outer boundary of cell (i,j) be denoted by $a_{j+\frac{1}{2}}$. Then the energy per unit time donated to the cells (i,j_1) and (i,j_2) will be:-

$$\left.\begin{aligned} \varepsilon_{i,j_1} &= \tfrac{1}{2}(E_1+E_2).(a_{j_1+\frac{1}{2}} - S_1)/(S_2-S_1) \\ \varepsilon_{i,j_2} &= \tfrac{1}{2}(E_1+E_2).(S_2 - a_{j_2-\frac{1}{2}})/(S_2-S_1) \end{aligned}\right\} \quad (5.19)$$

and for the cells (i,j) such that $j_1 < j < j_2$ (if any):-

$$\epsilon_{i,j} = \tfrac{1}{2}(E_1+E_2).(a_{j+\frac{1}{2}}-a_{j-\frac{1}{2}})/(S_2-S_1) \qquad (5.20)$$

Performing the above for the intersections of each pair of initially adjacent rays completes the energy assignment. Note that a running total must be kept, since each cell (i,j) may receive energy from a number of sources.

Resonant Absorption

Resonant absorption is included in the code by letting:-

$$\phi \rightarrow \left[1 - A(q)\right] \phi$$

as each ray passes through its turning point with respect to the density gradient (i.e. at x = 0, y = 0). Here A(q) is the effective coefficient of resonant absorption and $q = (ka)^{2/3} \sin^2\theta_o$ where k is the wave number of the laser light, a is the density scale length at the turning point, and θ_o is the angle the ray initially makes with the density gradient . For computational purposes it is assumed that a ray is not significantly refracted before entering the cell containing the turning point, and hence that θ_o is simply the angle that the density gradient in the turning point cell makes with the z-axis. Values for A(q) are obtained from the analytic expression derived by

Pert (2); these can be seen in tabular form in Appendix I. The code evaluates A(q) by linear interpolation of this table.

It should be noted that by putting A(q) equal to a constant β, the above mechanism can alternatively be used to simply initiate a 'dumping' of laser energy.

(iv) Test Cases

There are a number of density distributions for which the ray paths can be obtained analytically. Hence it is possible to check the accuracy of the ray-tracing code thoroughly. All of the following tests are performed with ruby laser light ($w = 2.73 \times 10^{15}$/sec, $n_c = 2.3 \times 10^{21}$/cc).

a) Linear Refractive Index Gradient

Taking the refractive index to be:-

$$\mu = \mu_o + \mu_g x \tag{5.21}$$

and assuming that the ray turns at x = 0, y = 0, gives a ray path of the form:-

$$y = \frac{2\mu_o}{\mu_g} \cdot \ln\left[\left(\frac{\mu_g x}{2\mu_o} + 1\right)^{\frac{1}{2}} + \left(\frac{\mu_g x}{2\mu_o}\right)^{\frac{1}{2}}\right] \tag{5.22}$$

In addition, if the ray starts from the zero density line at an angle $\lambda = \lambda_I$, (5.1) and (5.2) give the number density at the turning point to be:-

$$n_o = n_c \cos^2\lambda_I \tag{5.23}$$

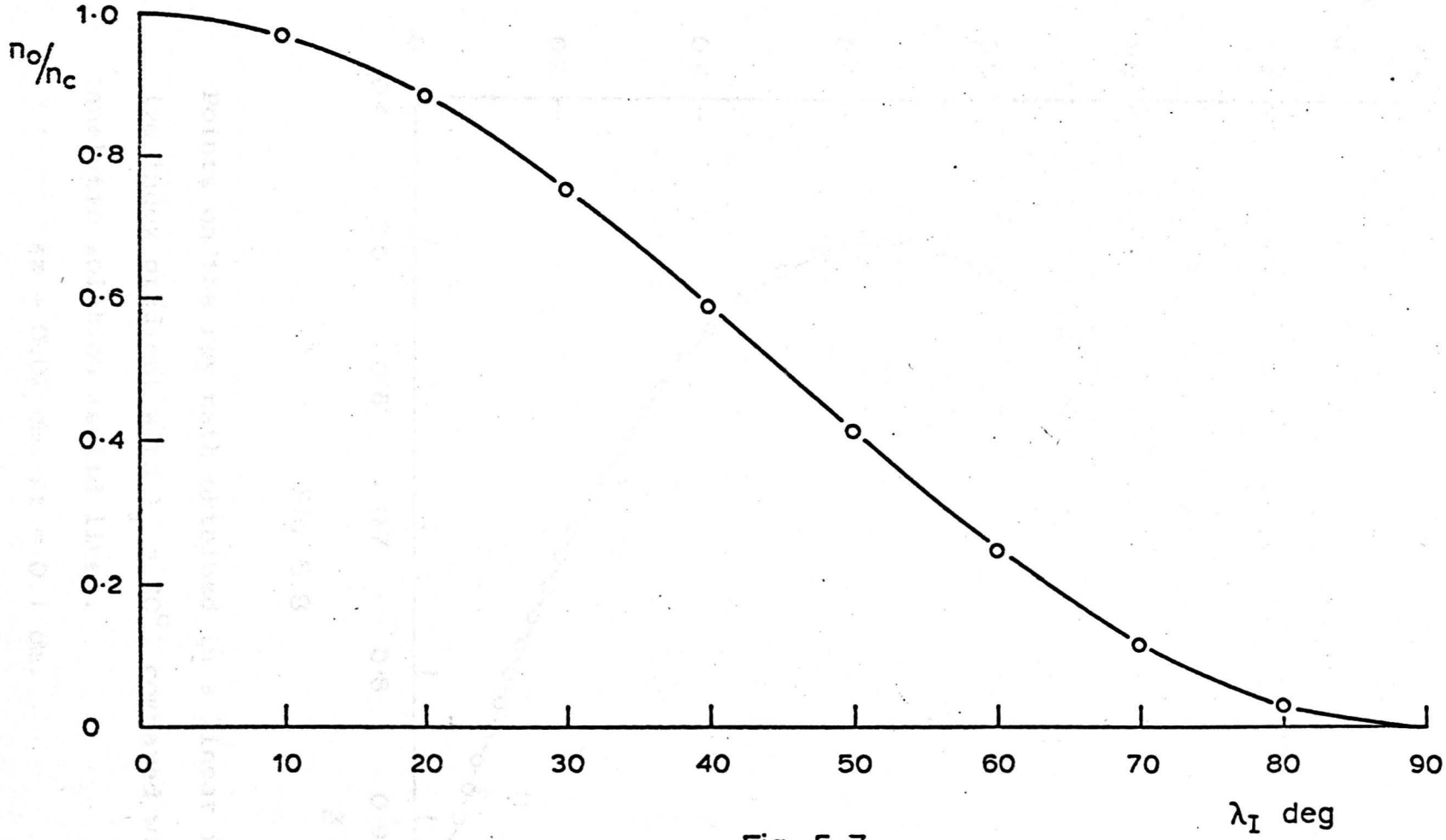

Fig. 5.7

Values obtained for density at the turning point in a linear refractive index gradient for various angles of incidence λ_I, compared with the analytic solution $n_o = n_c \cos^2 \lambda_I$ (solid line).

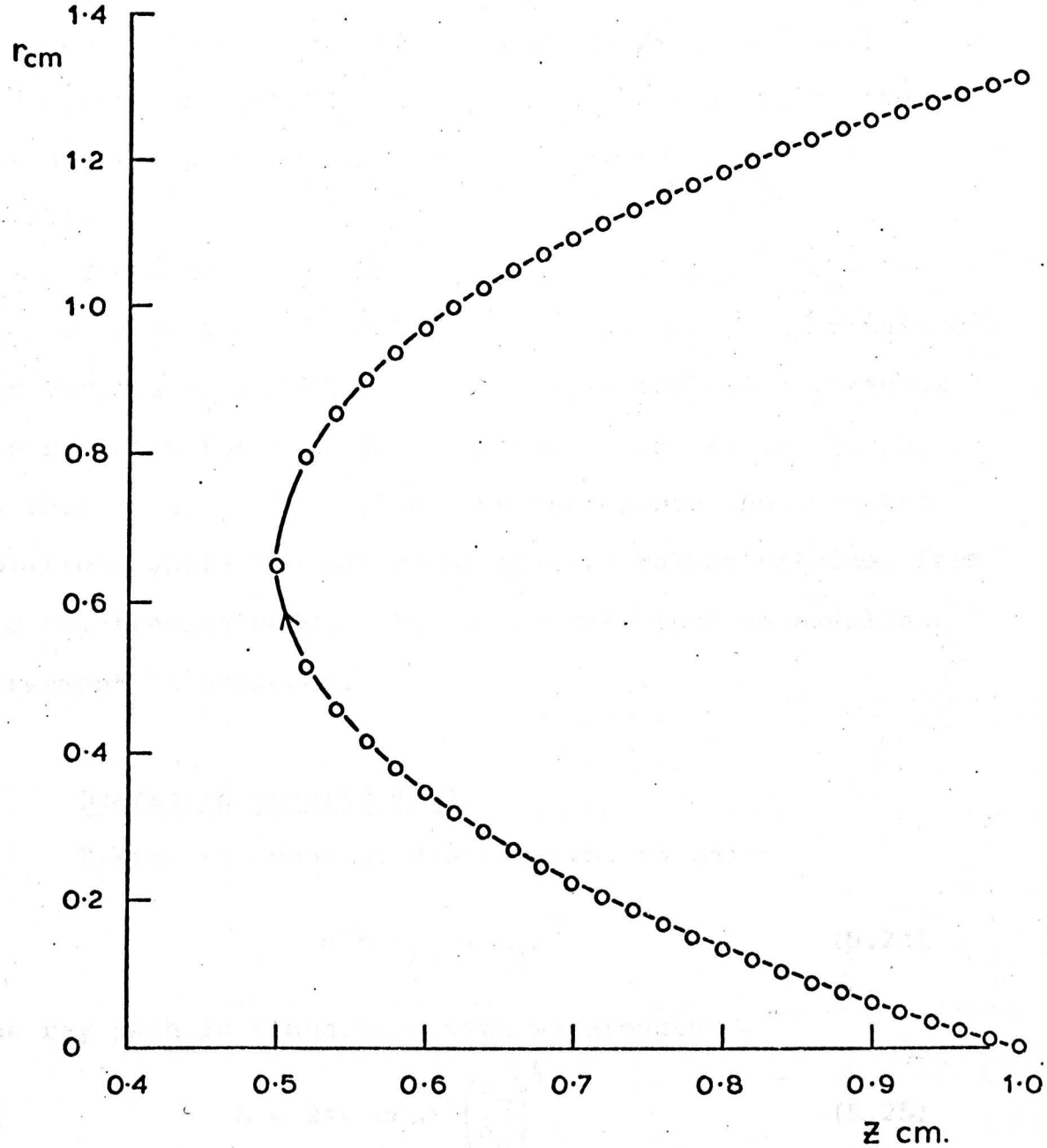

Fig. 5.8

Points on the ray path obtained in a linear refractive index gradient with $\lambda_I = 30^o$, compared with the analytic solution (solid line).

Δz = 0.02 cm. Δr = 0.1 cm.

The x-y coordinates of the starting point in terms of λ_I can easily be obtained from (5.1), (5.21) and (5.22) and hence the equation of the ray path relative to the z-r axes is given by the appropriate substitution in (5.22).

The code was run with $\mu = z$ using space steps $\Delta z = 0.02$ cm and $\Delta r = 0.1$ cm. The values of n_o obtained for various λ_I are shown in Fig. 5.7, and Fig. 5.8 shows the ray path for $\lambda_I = 30^o$. Here, as in all the graphs in this section, the solid line represents the analytic solution, while the marked points are values obtained from the ray-tracing code. It can be seen that an excellent agreement is achieved.

b) Quadratic Density Well

Taking the density distribution to be:-

$$n = n_A + n_g r^2 \tag{5.24}$$

the ray path is sinusoidal with wavelength:-

$$L = 2\pi\mu' \cos\lambda' \left(\frac{n_c}{n_g}\right)^{\frac{1}{2}} \tag{5.25}$$

and amplitude:-

$$A = \frac{L \tan\lambda'}{2\pi} \tag{5.26}$$

where λ' is the angle at which the ray crosses the z-axis and $\mu' = (1-n_A/n_C)^{\frac{1}{2}}$ is the refractive index on the z-axis.

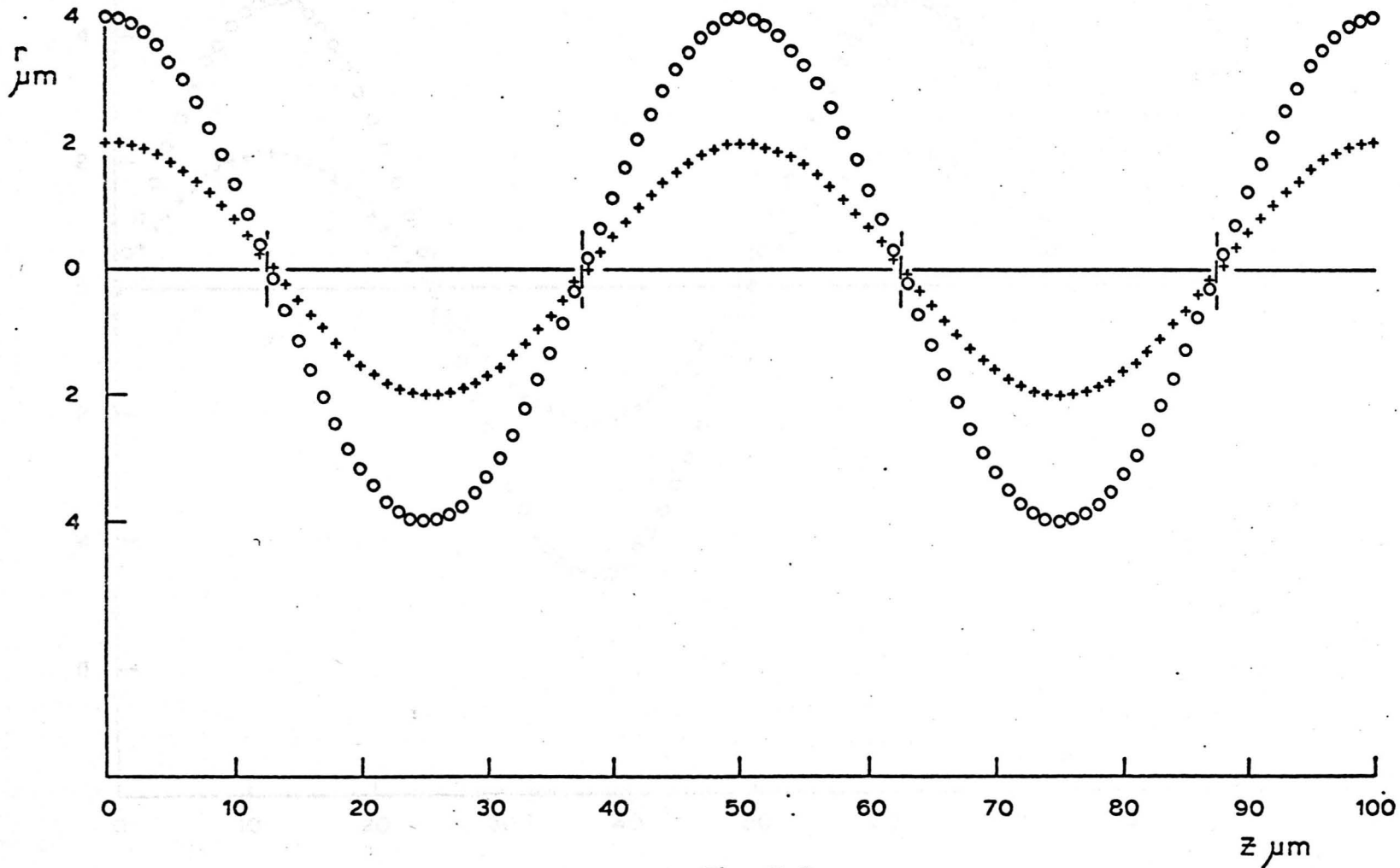

Fig. 5.9

Points on the ray path obtained in a quadratic density well for two different initial amplitudes. The analytic axis crossings are marked by short vertical lines.

$\Delta z = 10^{-4}$ cm, $\Delta r = 5 \times 10^{-5}$ cm.

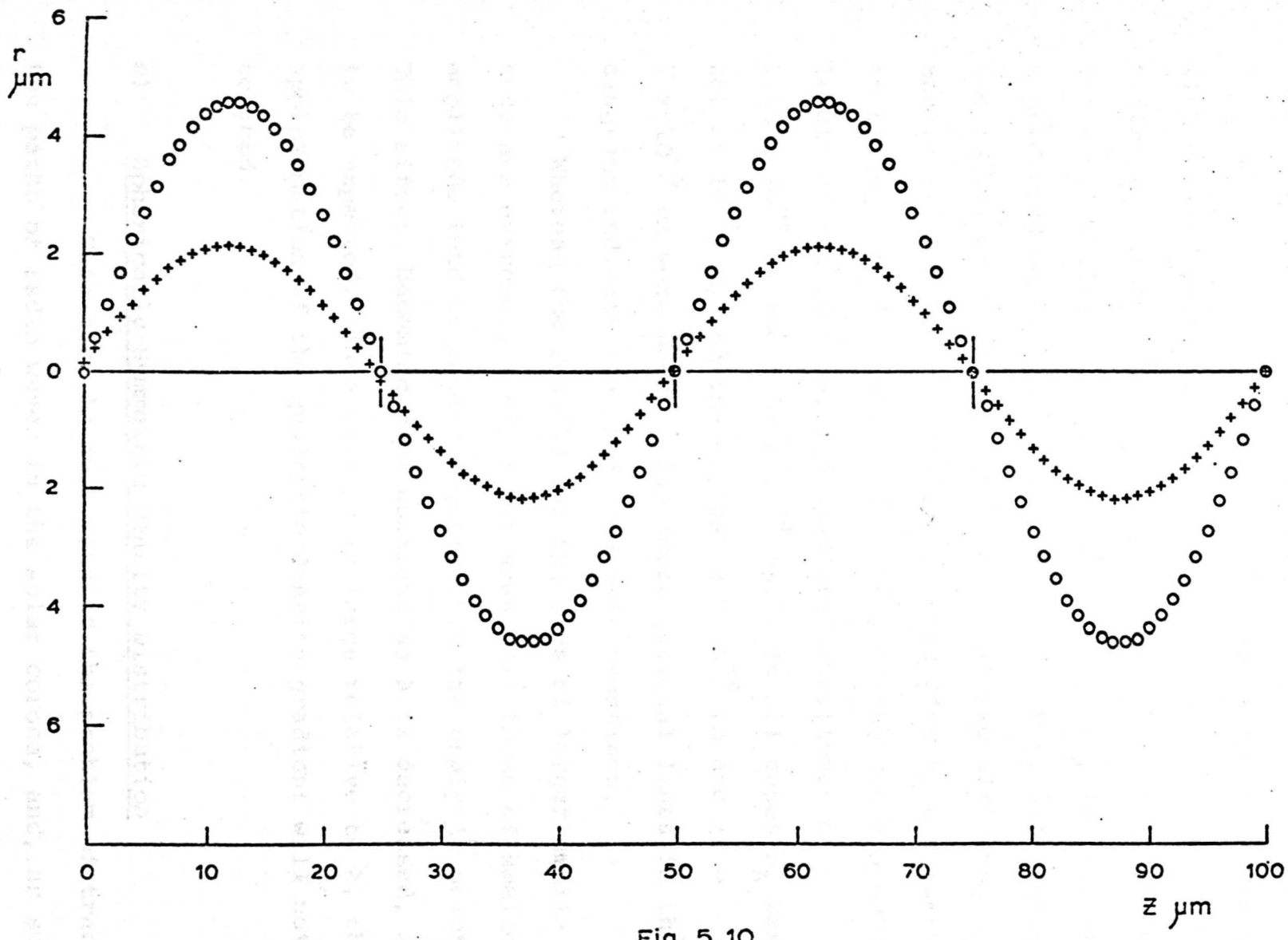

Fig. 5.10

Points on the ray path obtained in a quadratic density well for two different initial angles ($\lambda' = 15^{\circ}, \lambda' = 30^{\circ}$). The analytic axis crossings are marked by short vertical lines. $\Delta z = 10^{-4}$ cm, $\Delta r = 5 \times 10^{-5}$ cm.

(A full analysis of this case can be seen in appendix 2.)

Fig. 5.9 shows the results obtained for rays started with maximum r-displacement at $z = 10^{-2}$ cm, for two different values of A. For both runs n_g was taken to be $(n_c - n_A)/(2.5 \times 10^{-5}/4\pi^2 + A^2)$, thus giving, in each case, a predicted wavelength of 5×10^{-3} cm. Fig. 5.10 shows the result of starting rays on r = 0 at two different angles ($\lambda' = 15^o$, $\lambda' = 30^o$). In this case n_g was taken to be $(n_c - n_A)4\pi^2\cos^2\lambda'/2.5 \times 10^{-5}$, giving again a wavelength of 5×10^{-3} cm, and predicted amplitudes of 2.13×10^{-4} cm and 4.59×10^{-4} cm. In all cases n_A was set at 10^{21}/cc, and spacesteps $\Delta z = 10^{-4}$ cm and $\Delta r = 5 \times 10^{-5}$ cm were used. The short vertical lines in the diagrams indicate the predicted axis crossings.

Whereas the results for the rays of larger amplitude are extremely good, it is seen that those of smaller amplitude tend to wander slightly from the analytic solution. This effect, becoming more apparent as A is decreased, is to be expected, since when Δr is large relative to A, the approximation of the quadratic density gradient will not be good.

c) Spherically Symmetric Density Distribution

This case is analogous to the problem of tracing the paths of radio waves in the solar corona, and, as such, has been examined in some detail by Smerd (2) and Jaeger

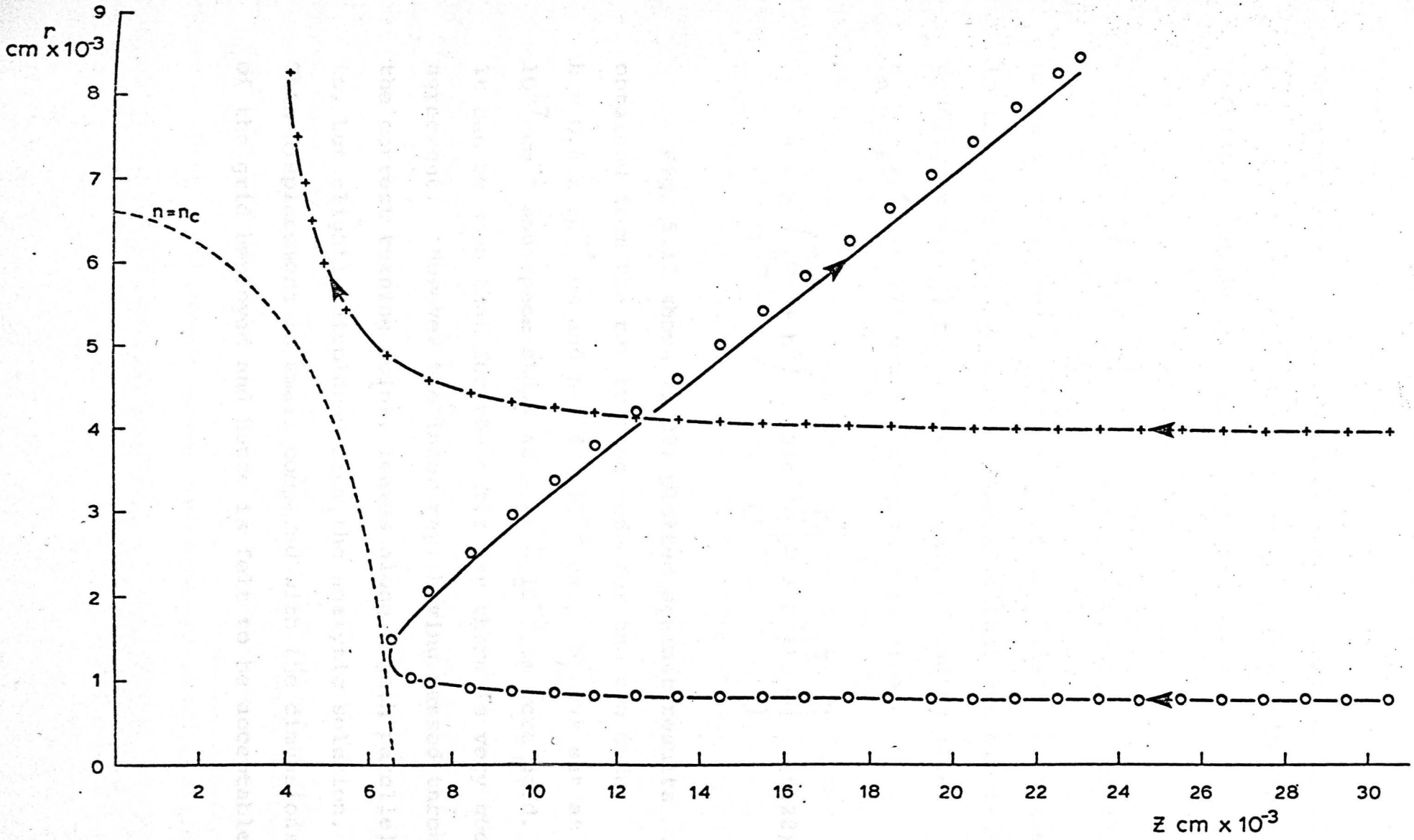

Fig. 5.11

Points on the ray path obtained in a spherically symmetric plasma for the two cases h = 0.8 x 10^{-3} cm and h = 4 x 10^{-3} cm, compared with the analtyic solution (solid line).

$\Delta z = \Delta r = 10^{-3}$ cm

and Westfold (3). Assuming that at infinity a ray is parallel to, and at a distance h from, the z-axis, then ref.(3) gives the ray trajectory as:-

$$\theta = h \cdot \int_{\rho}^{\infty} \frac{d\rho}{\rho\left(\mu^2\rho^2 - h^2\right)^{\frac{1}{2}}} \qquad (5.27)$$

where ρ and θ are the normal polar coordinates relative to the centre of symmetry. Assuming that the electron density decays as the inverse square of radius (i.e. $n_e = n_A/\rho^2$), (5.27) can be integrated to give:-

$$\theta = h \cdot \left(\frac{n_A}{n_c} + h^2\right)^{-\frac{1}{2}} \cdot \mathrm{Sin}^{-1}\left[\left(\frac{n_A}{n_c} + h^2\right)^{\frac{1}{2}} \cdot \frac{1}{\rho}\right] \qquad (5.28)$$

Fig. 5.11 shows (5.28) plotted against results obtained from the ray tracing code for the two cases $h = 0.8 \times 10^{-3}$ cm and $h = 4 \times 10^{-3}$ cm. n_A was set at 10^{17} cm^{-1} and space steps $\Delta z = \Delta r = 10^{-3}$ cm were used. It can be seen that for the outer ray there is very good agreement. However the inner ray, having passed through the correct turning point, leaves along a path parellel to, but slightly displaced from, the analytic solution. This displacement is small compared with the dimensions of the grid employed and hence is felt to be acceptable.

The aforementioned tests can also be used to check the absorption calculations of the ray tracing code. The results obtained for the spherical plasma will be given here.

The power associated with a ray at any point on its trajectory is given by:-

$$P = P_o \exp\left[- \int_{\rho}^{\infty} \alpha \, ds \right] \qquad (5.29)$$

where P_o is the initial power assigned to the ray and s is distance along the ray path. An expression for ds can be obtained from (5.27), and assuming temperature has a constant value T_c throughout the plasma, the absorption coefficient can be written as:-

$$\alpha = \frac{Cn^2}{n_c\left(1 - \frac{n}{n_c}\right)^{\frac{1}{2}}} \qquad (5.30)$$

where C is a constant. Integrating (5.29) then gives:-

$$P = P_o \exp\left\{- \frac{n_A^2 C}{n_c} \cdot \left[\frac{(\rho'^2 - H)^{\frac{1}{2}}}{2\rho'^2 H} + \frac{1}{2H^{3/2}} \operatorname{Sec}^{-1}\left(\frac{\rho'}{H^{\frac{1}{2}}}\right)\right]_{\rho}^{\infty}\right\} \qquad (5.31)$$

where $H = h^2 + n_A/n_c$.

Fig. 5.12 shows absorption results for the two rays of fig. 5.11 plotted against (5.31). The initial powers are set at 4×10^{13} erg/sec and 2×10^{14} erg/sec and T_c is taken as 10^6 °K. It can be seen that in the high absorption

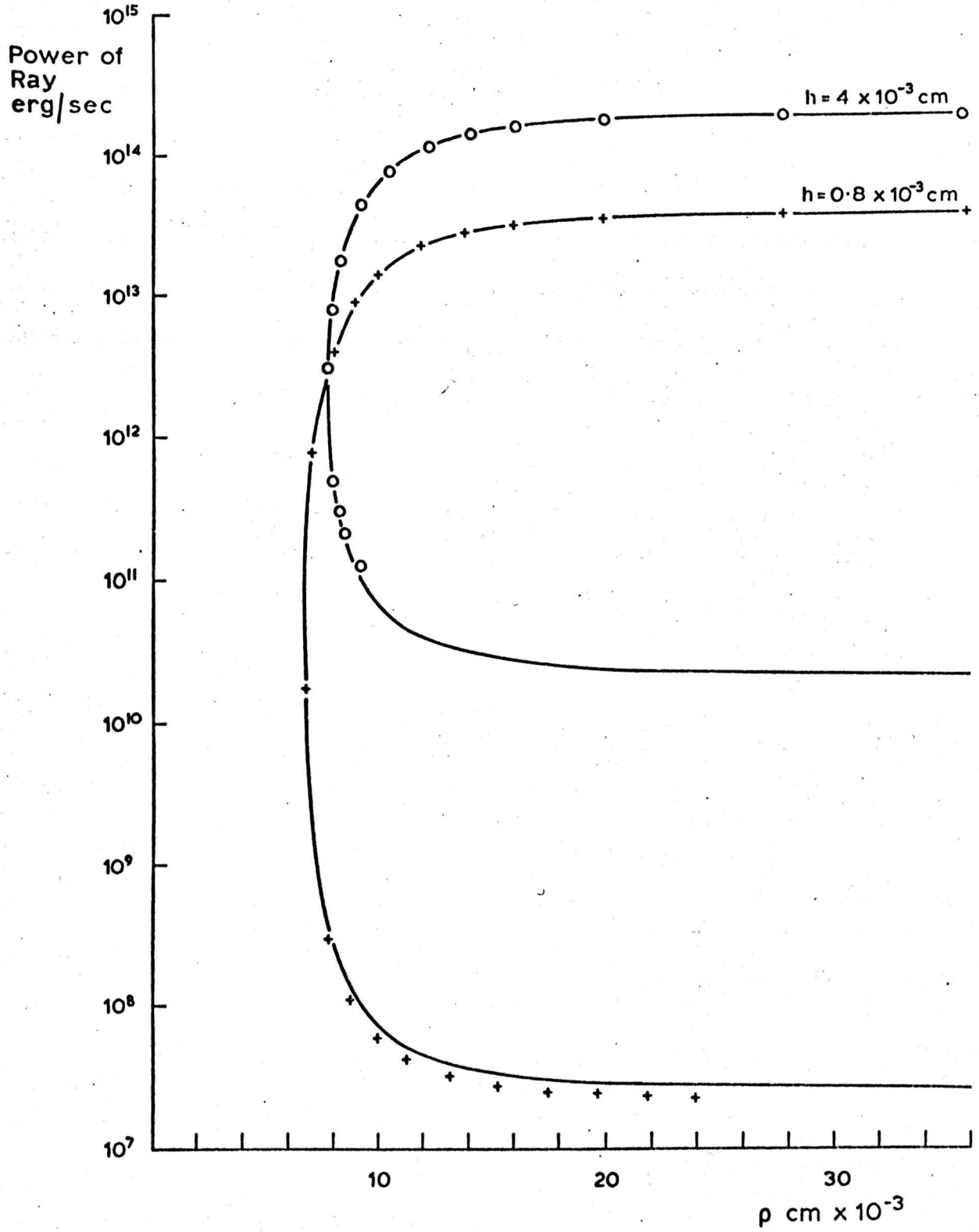

Fig. 5.12

Absorption along the ray path for the two rays of Fig. 5.11, compared with the analytic solution (solid line).

region the agreement is good and it is only when most of the energy has been absorbed that any deviation occurs. Hence, again, the results are felt to be acceptable.

In conclusion, the above tests would appear to show that the accuracy of the ray-tracing code is very good, with the proviso that, as in all numerical schemes, space steps of suitable dimensions are used.

CHAPTER 6

(i) Introduction

The ray tracing code was used to make a preliminary investigation of refraction effects in laser-plasma interactions for plane targets. The results obtained will be presented in this chapter.

Ideally the ray tracing code should be incorporated into a hydrodynamic code with ray paths being calculated at each time step. However this would be particularly costly in computer time. Hence the method used here is to obtain density and electron temperature distributions from the hydrodynamic code of Chapter 3 at a given time, and to use these as data for the ray tracing code. Comparing the distribution of absorbed energy produced by the ray tracing code with that of the hydrodyanmic code at the given time will show whether refraction effects are significant. Although not ideal, this method will serve to indicate the cases where the strongest effects are to be expected.

Typical ray paths and contours of energy absorption will be presented for each case considered. In each case the target material is hydrogen and the laser has a radius of 10^{-3} cm. The latter is modelled using twenty real rays plus one imaginary ray. Absorption in the underdense

plasma is solely by inverse bremsstrahlung. To facilitate comparison with the hydrodynamic code, resonant absorption is omitted here in favour of a simple 'dump', as described in Chapter 5, sec III.

(ii) Results

The first three cases examined are for a ruby laser with intensities chosen so as to be representative of the three regimes:- thin S-R, thin D-W and thick D-W. Cases 4, 5 and 6 will deal similarly with a CO_2 laser.

Case 1

Ruby laser, $\phi = 10^{18}$ c.g.s (thin S-R), t = 2 n.s.

The density and electron temperature distributions obtained from the hydrodynamic code can be seen in Figs. 4.2(a) and 4.6(a). Fig. 6.1 shows some typical ray paths obtained from the ray tracing code. It can be seen that there is very little refraction until the critical density surface is reached. Here the beam is scattered through a large area. Since, in this case, the majority of the laser energy will be absorbed before or at the critical density, it is to be expected that the heating of the plasma will be little affected when refraction is taken into consideration. This can be seen in Fig. 6.2 where contours of the rate of energy absorption per c.c. for the case of no refraction (a) are compared with those

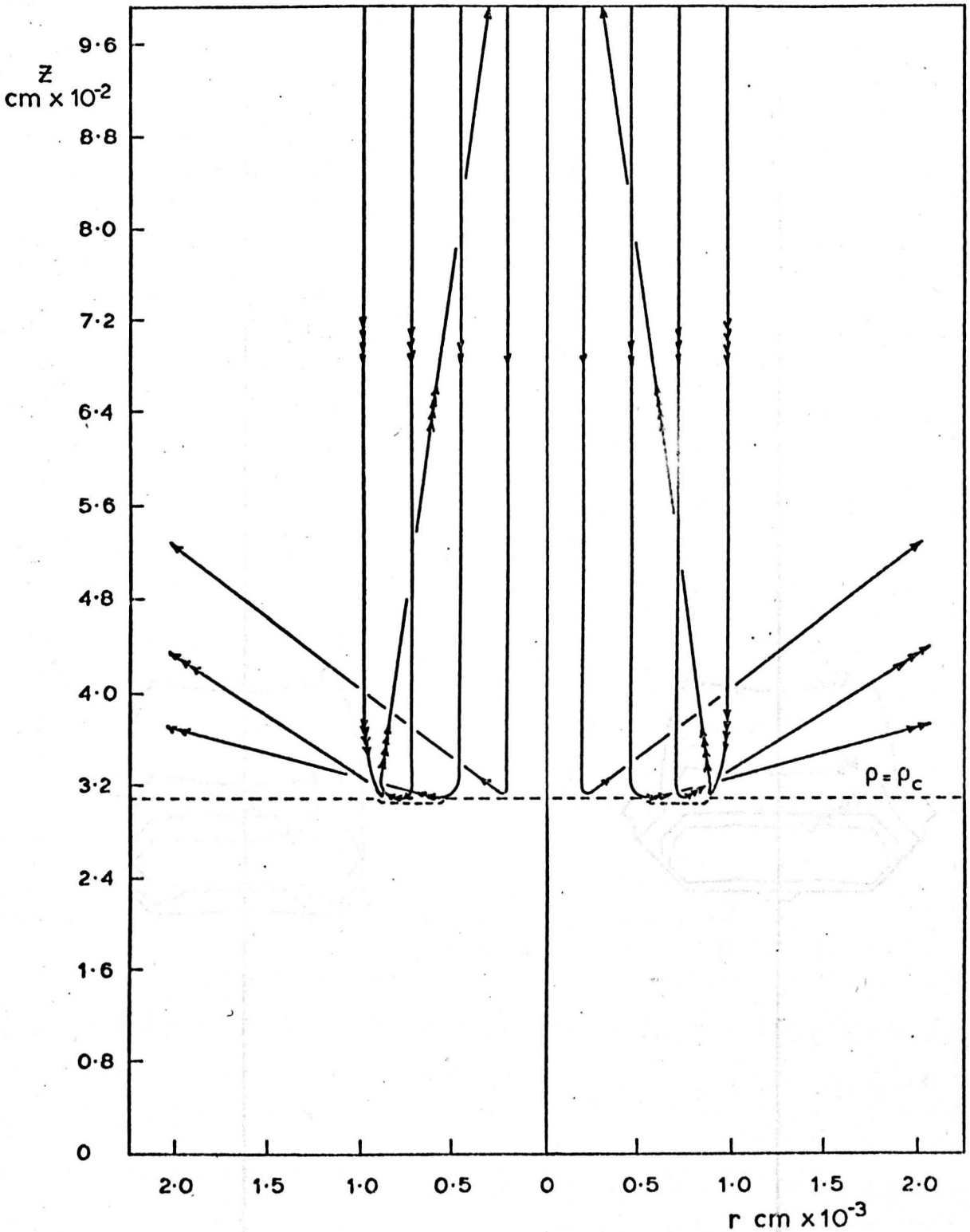

Fig. 6.1

Ray paths for a ruby laser ($\phi = 10^{18}$ c.g.s.) at $t = 2$ n.s. $\Delta r = 2.5 \times 10^{-4}$ cm, $\Delta z = 2 \times 10^{-3}$ cm.

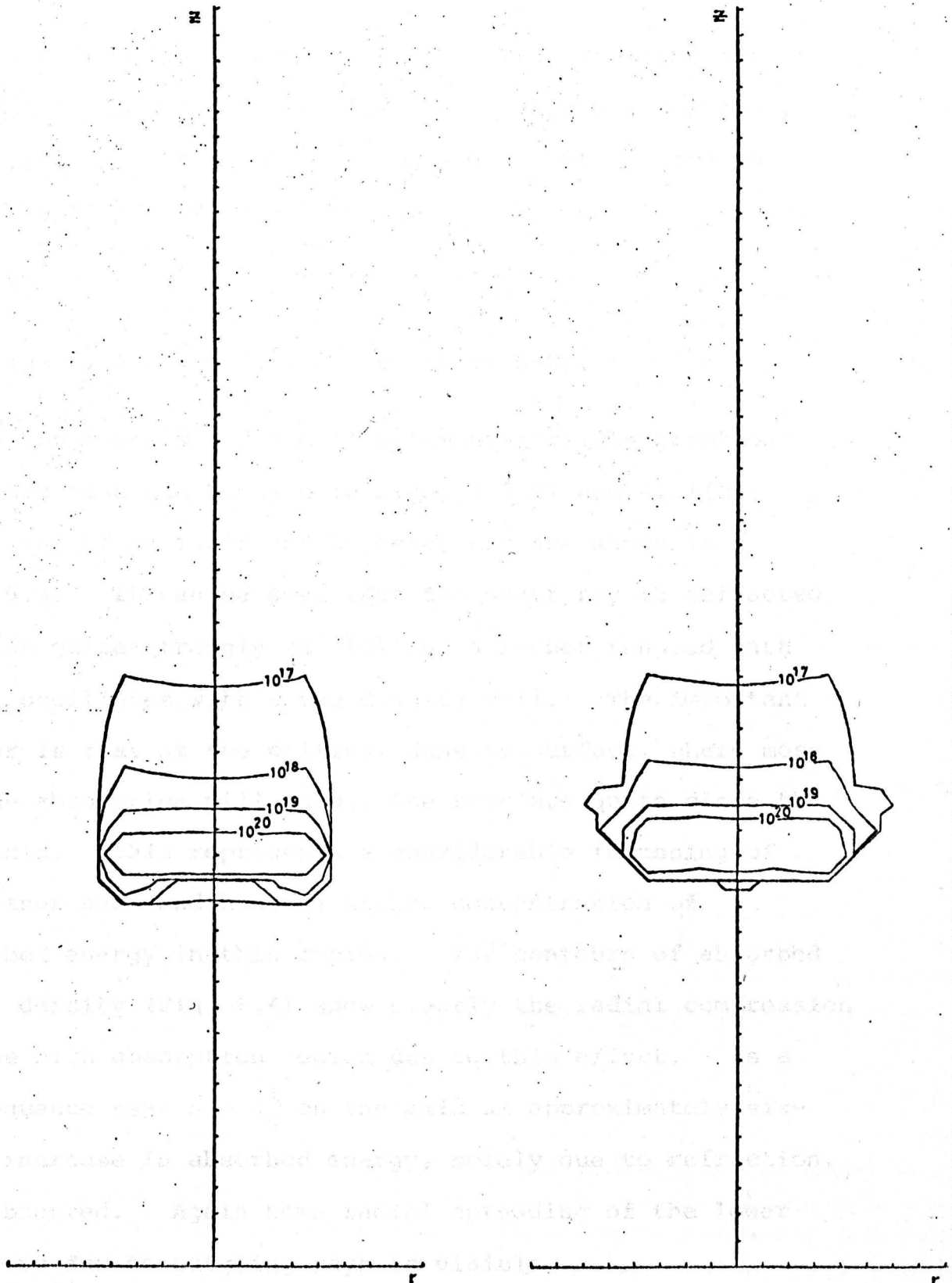

(a) No Refraction

(b) With Refraction

Fig 6.2
Absorbed Power Density
(erg/sec. cc)
Ruby Laser, $\phi = 10^{16}$ c.g.s,
$\Delta r = 2.5 \times 10^{-4}$cm, $\Delta z = 2 \times 10^{-3}$cm.
t = 2n.s.

obtained from the ray tracing code (b). No important difference is perceivable in the high absorption region. A slight radial spreading of the lower contours due to outgoing refracted rays can be seen.

Case 2

Ruby laser, $\phi = 2 \times 10^{20}$ c.g.s. (thin D-W), t = 2 n.s.

The density and electron temperature distributions for this case can be seen in Figs. 4.7(a) and 4.11(a). The paths of an inner and an outer ray are shown in Fig. 6.3. It can be seen that the outer ray is refracted inwards quite strongly and follows a rather tangled path as it oscillates within the density well. The important factor is that at the critical density surface, where most of the absorption will occur, the rays are quite close to the axis. This represents a considerable focussing of the laser beam and hence a higher concentration of absorbed energy in this region. The contours of absorbed power density (Fig. 6.4) show clearly the radial compression of the high absorption region due to this effect. As a consequence near $\rho = \rho_c$ on the axis an approximately six-fold increase in absorbed energy, solely due to refraction, is observed. Again some radial spreading of the lower contours due to outgoing rays is visible.

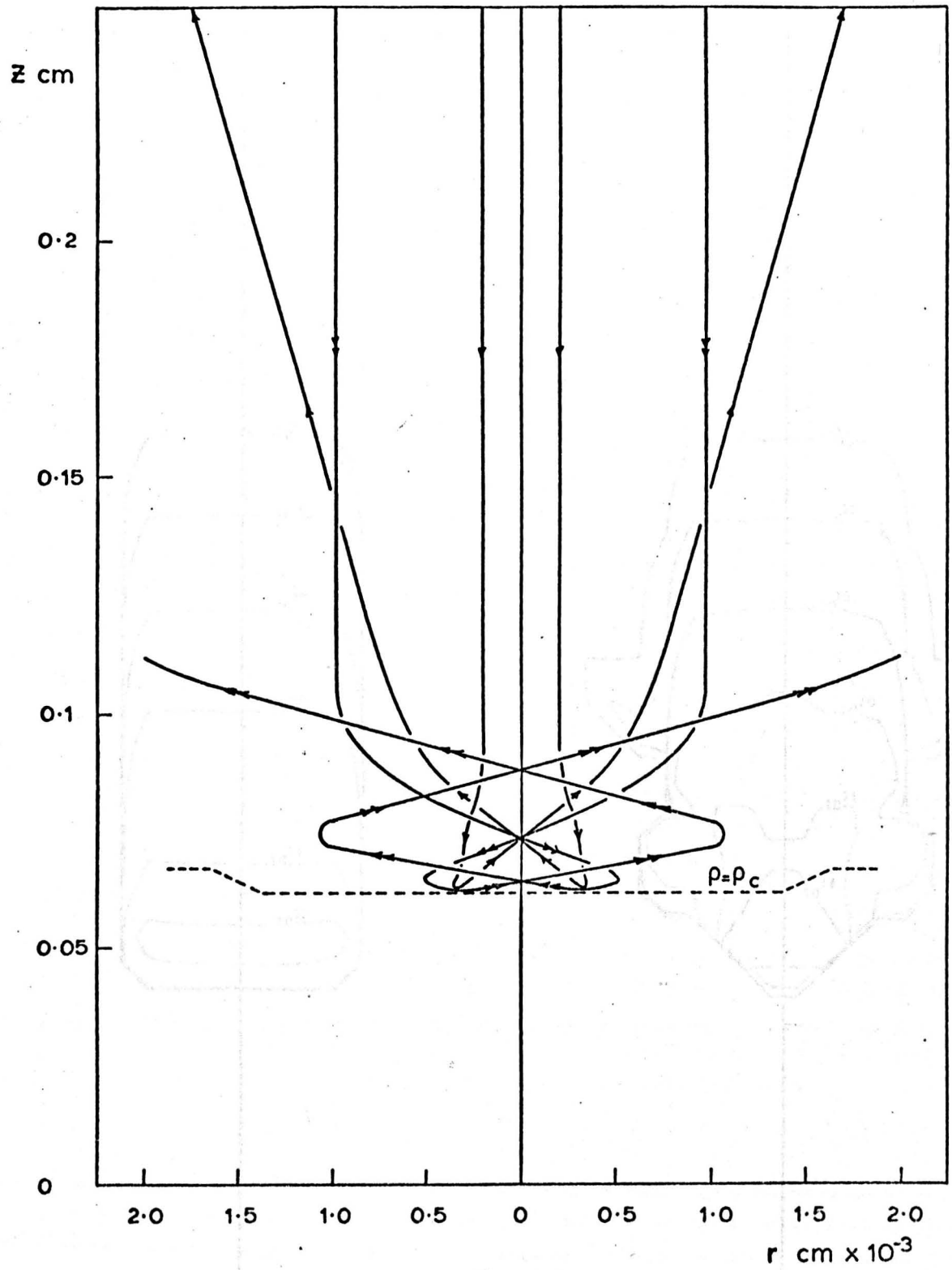

Fig. 6.3

Paths of inner and outer rays for a ruby laser ($\phi = 2 \times 10^{20}$ c.g.s.) at t = 2 n.s.

$\Delta r = 2.5 \times 10^{-4}$ cm, $\Delta z = 5 \times 10^{-3}$ cm.

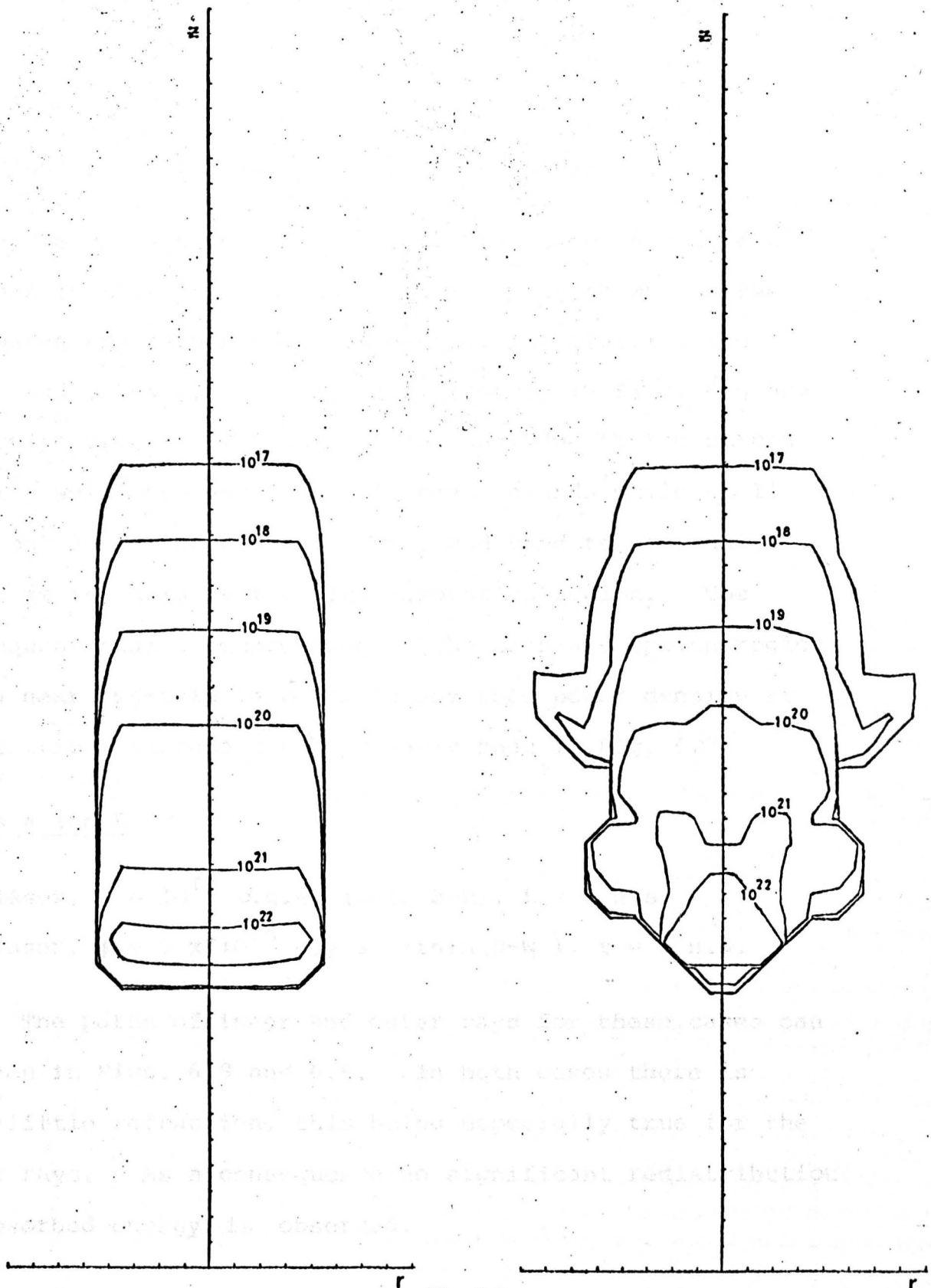

(a) No Refraction

(b) With Refraction

Fig. 6.4
Absorbed Power Density
(erg/sec.cc)
Ruby Laser, $\phi = 2\times10^{20}$ c.g.s.
$\Delta r = 2.5\times10^{-4}$cm, $\Delta z = 5\times10^{-3}$cm.
t = 2 n.s.

Case 3

Ruby laser, $\phi = 5 \times 10^{21}$ c.g.s. (thick D-W), t = 1 ns.

The relevant density and electron temperatures can be seen in Figs. 4.12(a) and 4.16(a). In this case the ray paths are rather tortuous and so, for clarity, the inner and outer rays are shown separately in Figs. 6.5 and 6.6 respectively. It can be seen that, due to the strong density well, the rays are refracted inwards while still well out in the expanding plasma, and tend to stay quite close to the axis in the high absorption region. The consequent radial compression of the high absorption region and a near ten-fold increase in absorbed power density at the critical surface can be clearly seen in Fig. 6.7.

Cases 4 and 5

CO_2 laser, $\phi = 10^{14}$ c.g.s. (thin S-R), t = 2 n.s.
CO_2 laser, $\phi = 5 \times 10^{15}$ c.g.s. (thin D-W), t = 2 n.s.

The paths of inner and outer rays for these cases can be seen in Figs. 6.8 and 6.9. In both cases there is very little refraction, this being especially true for the inner rays. As a consequence no significant redistribution of absorbed energy is observed.

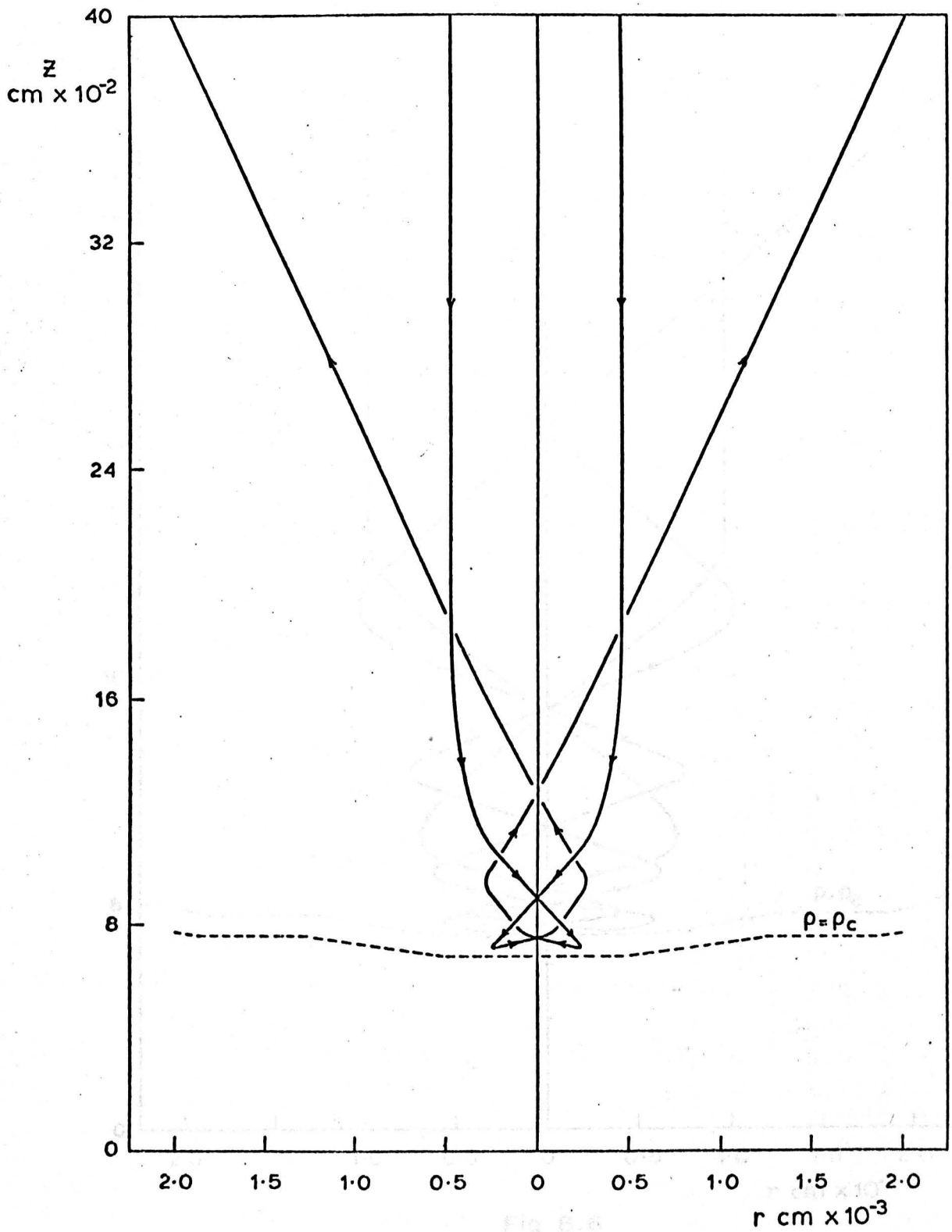

Fig. 6.5

Path of an inner ray for a ruby laser (ϕ = 5 x 10^{21} c.g.s) at t = 1 n.s.

$\Delta r = 5 \times 10^{-4}$ cm, $\Delta z = 8 \times 10^{-3}$ cm

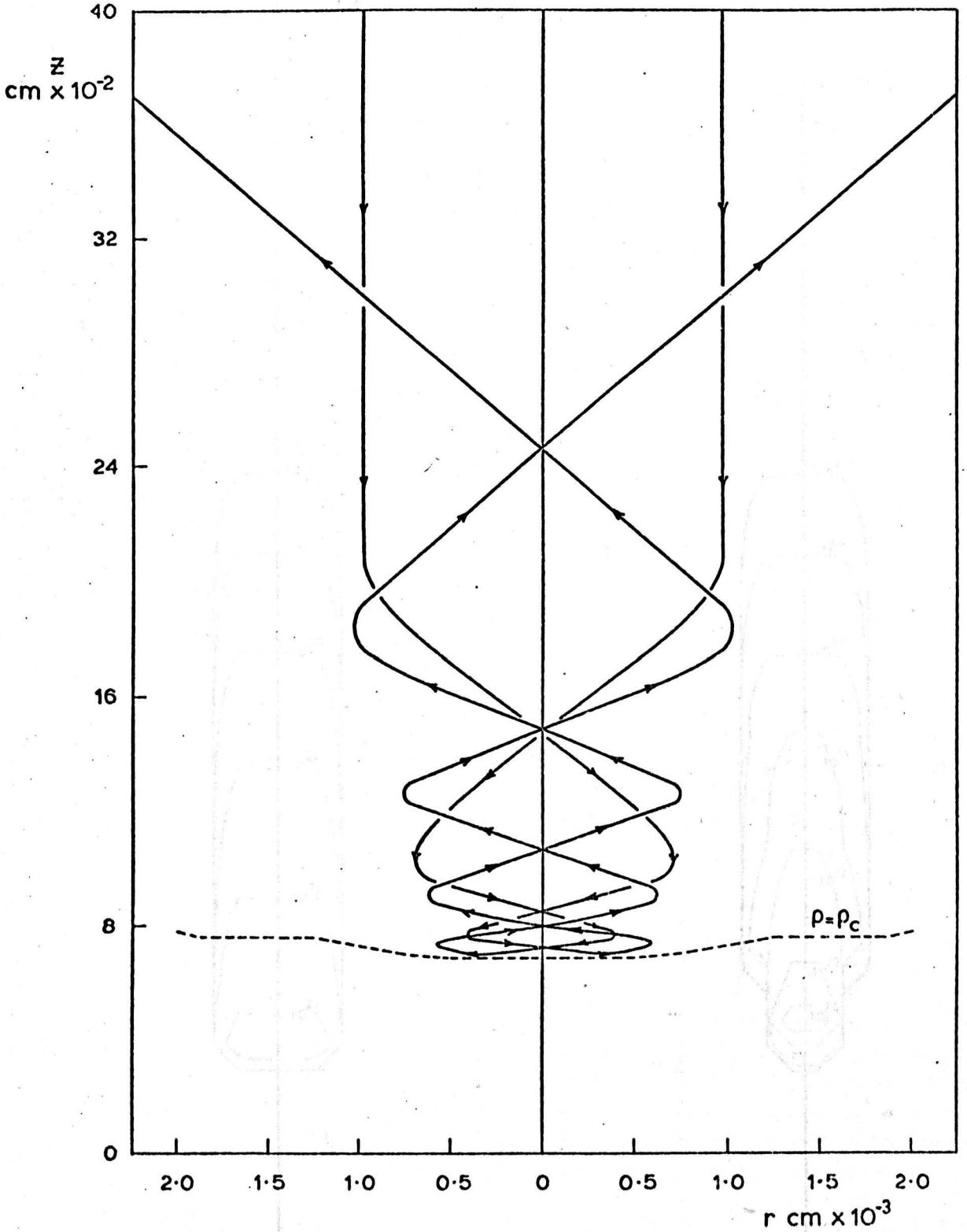

Fig. 6.6

Path of an outer ray for a ruby laser (ϕ = 5 x 10^{21} c.g.s) at t = 1 n.s.

$\Delta r = 5 \times 10^{-4}$ cm, $\Delta z = 8 \times 10^{-3}$ cm

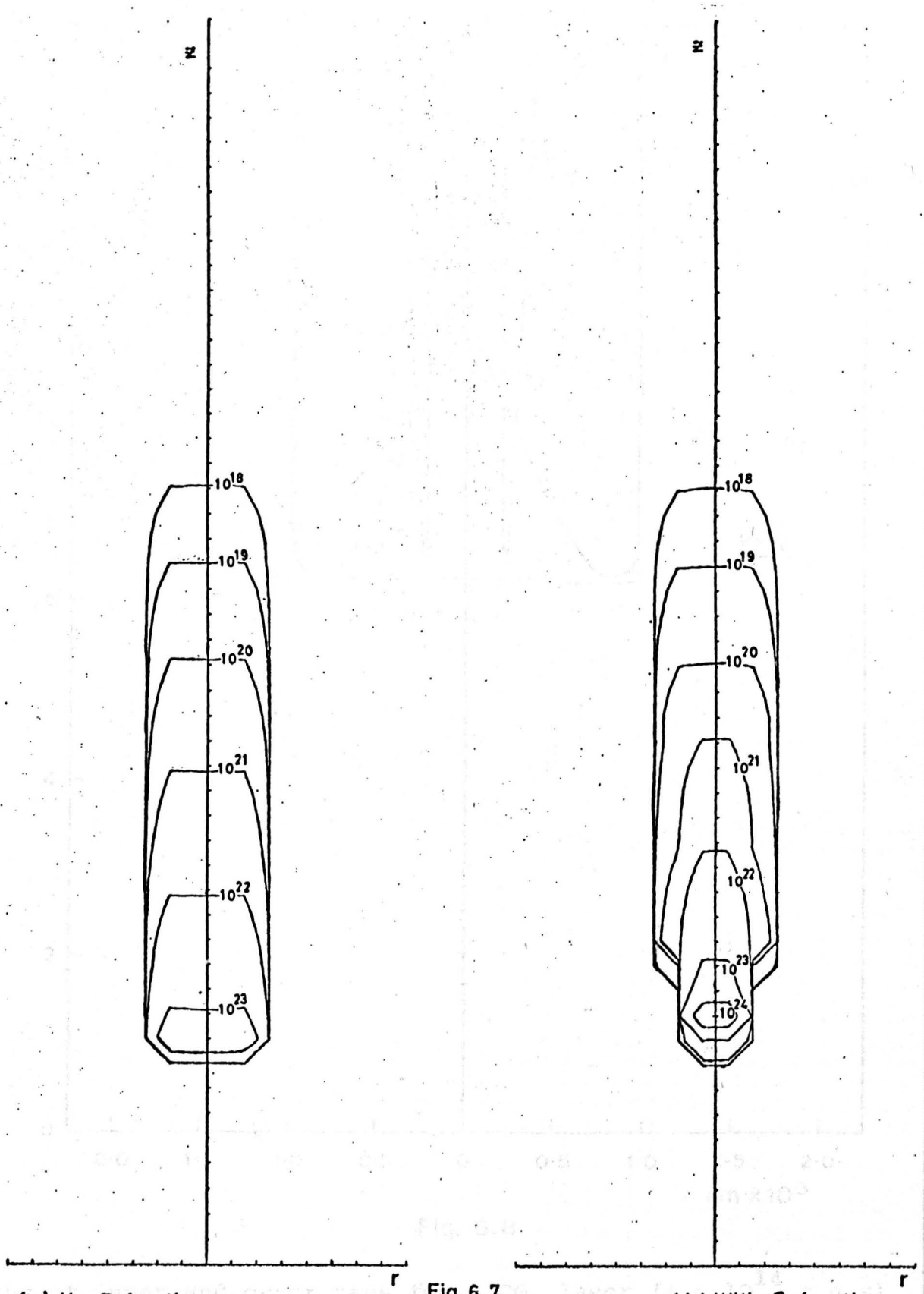

(a) No Refraction

(b) With Refraction

Fig. 6.7
Absorbed Power Density
(erg/sec.cc)
Ruby Laser, $\phi = 5 \times 10^{21}$ c.g.s.
$\Delta r = 5 \times 10^{-4}$ cm, $\Delta z = 8 \times 10^{-3}$ cm.
t = 1n.s.

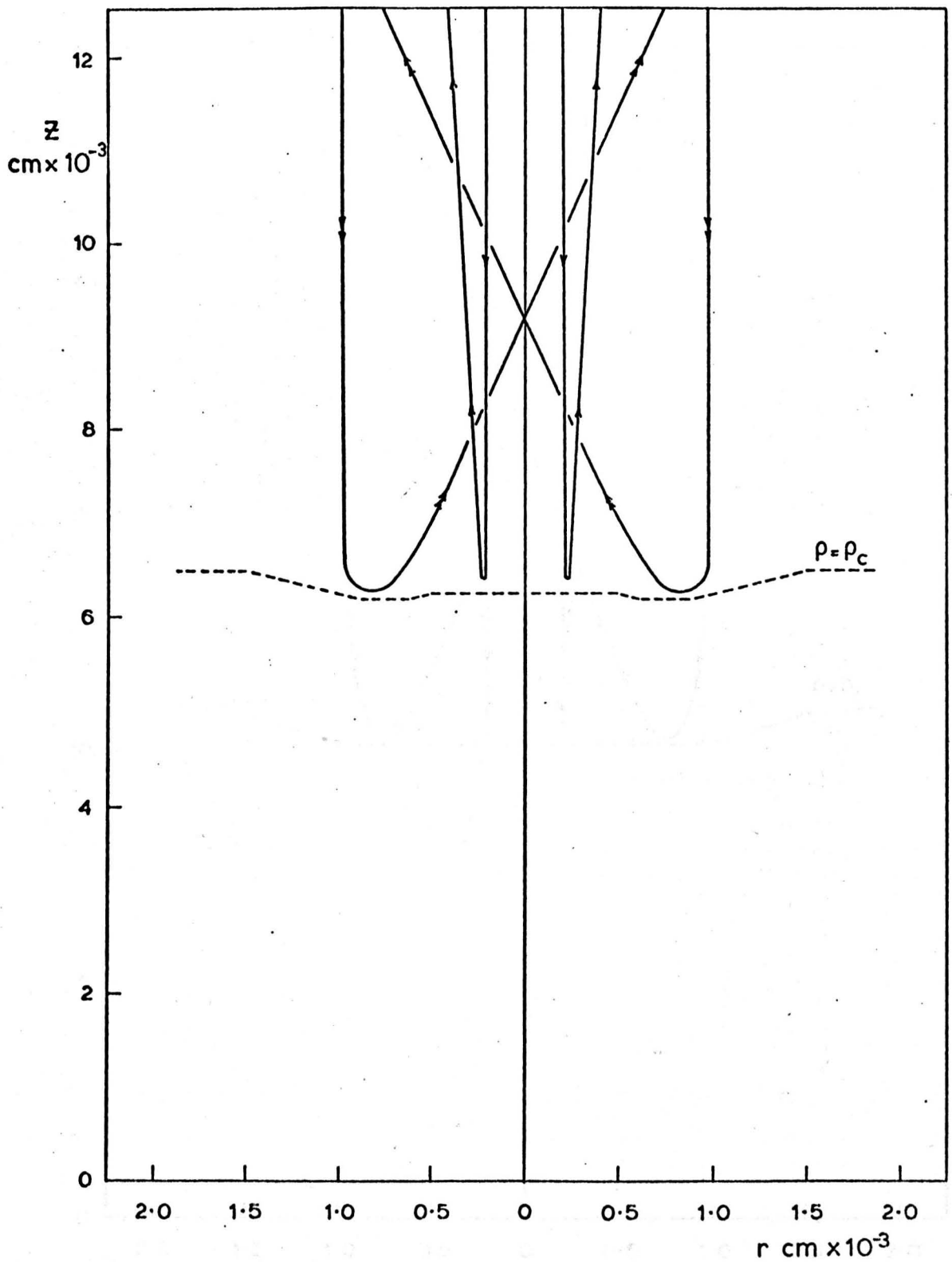

Fig. 6.8

Paths of inner and outer rays for a CO_2 laser ($\phi = 10^{14}$ c.g.s) at t = 2 n.s.

$\Delta r = 2.5 \times 10^{-4}$ cm, $\Delta z = 2.5 \times 10^{-4}$ cm.

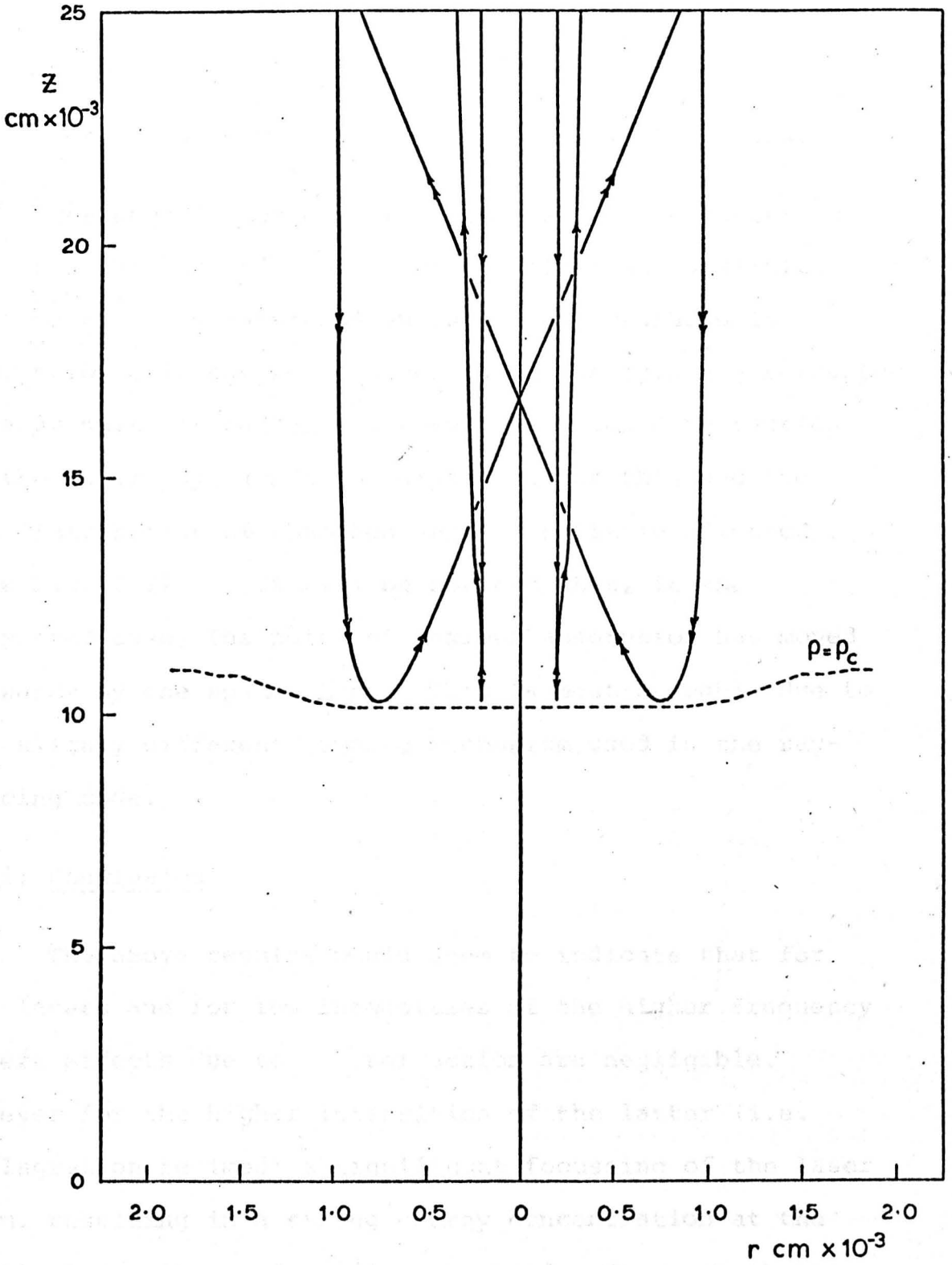

Fig. 6.9

Paths of inner and outer rays for a CO_2 laser ($\phi = 5 \times 10^{15}$ c.g.s) at t = 2 n.s.

$\Delta r = 2.5 \times 10^{-4}$ cm, $\Delta z = 5 \times 10^{-4}$ cm

Case 6

CO_2 laser, $\phi = 5 \times 10^{18}$ c.g.s. (thick D-W), t = 1 n.s.

The density and electron temperature distributions for this case can be seen in Figs 4.17(b) and 4.21(b). The paths of an inner and an outer ray are shown in Fig. 6.10. It can be seen that the outer rays are refracted inwards quite strongly. However the outward refraction of the inner rays tends to compensate for this and the net distribution of absorbed energy is little affected (see Fig. 6.11). It will be noticed that, in the refracted case, the point of maximum absorption has moved outwards by one space-step. This is most probably due to the slighly different dumping mechanism used in the ray-tracing code.

(iii) Conclusion

The above results would seem to indicate that for CO_2 lasers and for low intensities of the higher frequency lasers effects due to refraction are negligible. However for the higher intensities of the latter (i.e. deflagration regimes) a significant focussing of the laser beam, resulting in a strong energy concentration at the critical density surface, is observed. Hence in these cases a significant deviation from the theoretical temperature scaling might be expected. However thermal conduction will of course be in operation and this may well be strong

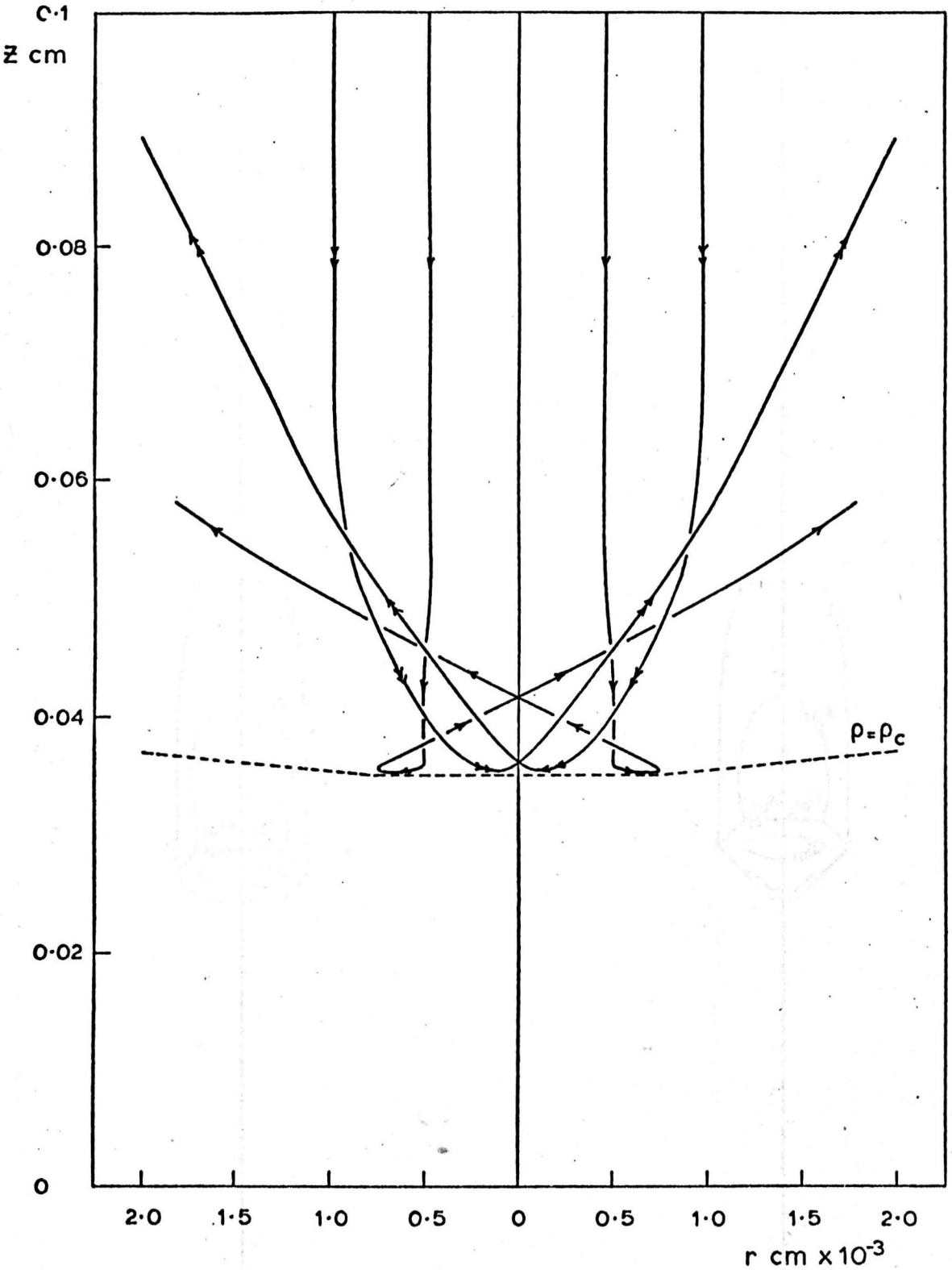

Fig. 6.10

Paths of inner and outer rays for a CO_2 laser (ϕ = 5 x 10^{18} c.g.s) at t = 1 n.s.

$\Delta r = 5 \times 10^{-4}$ cm, $\Delta z = 2 \times 10^{-3}$ cm.

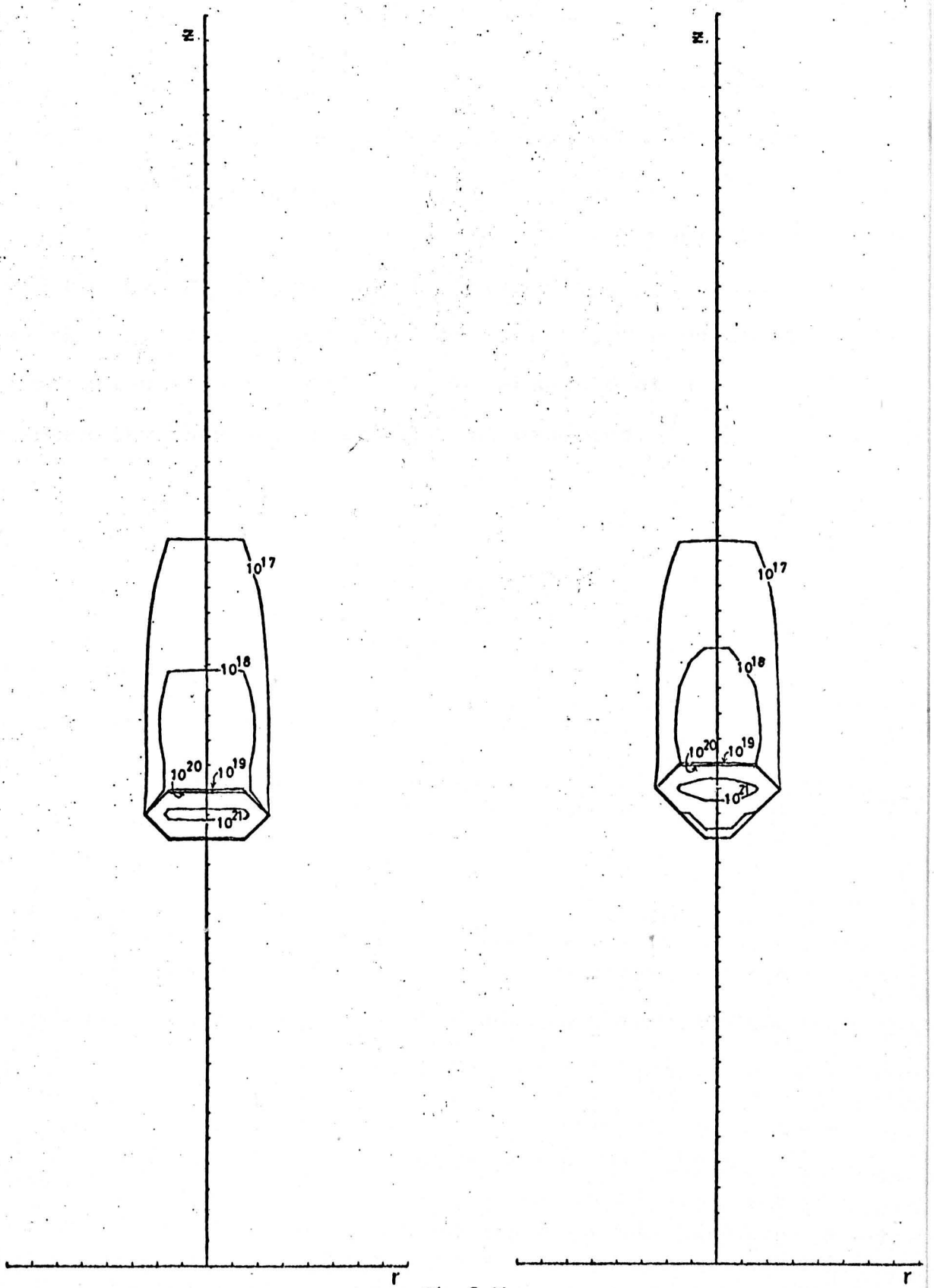

(a) No Refraction

Fig 6.11
Absorbed Power Density
(erg/sec.cc)
CO_2 Laser, $\phi = 5\times10^{18}$ c.g.s
$\Delta r = 5\times10^{-4}$cm, $\Delta z = 2\times10^{-3}$cm.
t = 1 n.s., f = 0.05

(b) With Refraction

enough to smooth out these effects. A further investigation using the ray tracing code incorporated in a hydrodynamic code would be needed to confirm this. Be this as it may the larger temperature gradients that would be produced by this concentration of absorbed energy, would suggest that for the higher frequency lasers, the onset of flux limitation effects might well be observed at a lower intensity than would normally be expected.

APPENDIX I

Values of the effective coefficient of resonant absorption A(q). (See Chapter 5).

q	A(q)	q	A(q)
0.0	0.0	1.6	0.0925
0.1	0.2207	1.7	0.0730
0.2	0.3655	1.8	0.0571
0.3	0.4494	1.9	0.0442
0.4	0.4874	2.0	0.0340
0.5	0.4924	2.1	0.0259
0.6	0.4728	2.2	0.0195
0.7	0.4382	2.3	0.0145
0.8	0.3957	2.4	0.0109
0.9	0.3485	2.5	0.0081
1.0	0.3010	2.6	0.0059
1.1	0.2558	2.7	0.0043
1.2	0.2139	2.8	0.0031
1.3	0.1766	2.9	0.0022
1.4	0.1439	3.0	0.0016
1.5	0.1160	3.1	0.0011
		$\geq$ 3.2	$\approx$ 0.0

APPENDIX II

Ray Path in a Quadratic Density Well

Assume that the density is given by $n = n_A + n_g r^2$. Taking λ to be the angle the ray makes with the z-axis, Snell's law gives:-

$$\mu \cos\lambda = \mu_\infty \qquad (1)$$

where μ_∞ is the refractive index when $\lambda = 0$. The refractive index can be written in the form:-

$$\mu^2 = \mu_\infty^2 (1 + \alpha - \beta r^2) \qquad (2)$$

where

$$\beta = \frac{n_g}{n_c \mu_\infty^2} \qquad (3)$$

If the ray crosses the z-axis at angle $\lambda = \lambda'$ then (1) gives:-

$$\mu' \cos\lambda' = \mu_\infty \qquad (4)$$

where $\mu' = (1 - n_A/n_c)^{\frac{1}{2}}$ is the refractive index on the z-axis; also (2) gives:-

$$\mu'^2 = \mu_\infty^2 (1 + \alpha) \qquad (5)$$

Hence from (4) and (5):-

$$\alpha = \mathrm{Tan}^2\lambda' \qquad (6)$$

Using (1) and (2) the ray path is given by:-

$$\frac{dr}{dz} = \tan\lambda = (\alpha - \beta r^2)^{\frac{1}{2}} \qquad (7)$$

Integrating between (z_1,r_1) and (z_2,r_2) gives the sinusoidal solution:

$$z_2 - z_1 = \frac{1}{\sqrt{\beta}} \cdot \left[\sin^{-1}\left(\left[\frac{\beta}{\alpha}\right]^{\frac{1}{2}} \cdot r_2 \right) - \sin^{-1}\left(\left[\frac{\beta}{\alpha}\right]^{\frac{1}{2}} \cdot r_1 \right) \right] \qquad (8)$$

with wavelength:-

$$L = \frac{2\pi}{\sqrt{\beta}} = 2\pi\mu'\cos\lambda'(n_c/n_g)^{\frac{1}{2}} \qquad (9)$$

and amplitude

$$A = \left(\frac{\alpha}{\beta}\right)^{\frac{1}{2}} = L \tan\lambda'/2\pi \qquad (10)$$

REFERENCES

Chapter 1

(1) W. J. Fader. Phys. Fluids 11, 2200 (1968)

(2) R. E. Kidder. Nucl. Fusion 8, 3 (1968)

(3) J.W. Shearer and W. S. Barnes. Laser Interaction with Matter and Related Plasma Phenomena. Ed. H. J. Schwarz and H. Hora. Plenum Press

(4) P. Mulser. Z. Naturforsch 25, 282 (1970)

(5) J. Nuckolls, T. Wood et al. Nature 239, 139 (1972)

(6) E. B. Goldman. Plasma Physics 15, 289 (1973)

(7) J. S. Clarke, H. N. Fisher and R. J. Mason. Phys. Rev. Lett. 30, 89 (1973)

Chapter 2

(1) J. M. Dawson and C. R. Oberman, Phys Fluids 5, 517 (1962)

(2) L. Spitzer. Physics of Fully Ionized Gases. Interscience Publishers, Inc., New York, 1956

(3) P. D. Lax. Comm. Pure Appl. Math. 7, 159 (1954)

(4) P. D. Lax and B. Wendroff. Comm. Pure Appl. Math. 8, 217 (1960)

(5) R. A. Gentry, R. E. Martin and B. J. Daly. J. of Comp. Phys. 1, 87 (1966)

(6) J. P. Boris and D. L. Book. J. of Comp. Phys. 11, 38 (1973)

(7) D. L. Book, J. P. Boris and K. Hain. J. of Comp. Phys. 18, 248 (1975)

(8) G. J. Pert. Private communication

(9) R. D. Richtmyer and K. W. Morton. Difference Methods for Initial-Value Problems. Wiley, New York.

(10) D. S. Kershaw. J. of Comp. Phys. 26, 43 (1978)

(11) J. P. Christiansen and K.V. Roberts. J. of Comp. Phys. 17, 332 (1975)

(12) C. W. Hirt. J. Comp. Phys. 2, 339 (1968)

(13) C.W. Hirt, A. A. Amsden and J. L. Cook. J. of Comp. Phys. 14, 227 (1974)

Chapter 3

(1) J. M. Dawson. Phys. Fluids 7, 981 (1964)

(2) N. G. Basov and O. N. Krokhin. Sov. Phys. JETP 19, 123 (1964)

(3) A. Caruso and F. Gratton. Nucl. Fusion 5, 87 (1965)

(4) O. N. Krokhin. Sov. Phys - Tech. Physics 9, 1024 (1965)

(5) O. N. Krokhin. J. of Appl. Math. and Phys. 16, 123 (1965)

(6) Yu V. Afanasyev, V. M. Krol, O.N. Krokhin and I. V. N. Nemchinov. PMM 30, 1218 (1966)

(7) Yu. V. Afanasyev, O. N. Krokhin and G. V. Sklizkov. J. of Quant. Electronics 2, 483 (1966)

(8) A.Caruso, B. Bertotti and P. Giupponi. Nuovo Cimento 10, No. 45, 176 (1966)

(9) A. Caruso and R. Gratton. Plasma Physics 10, 867 (1968)

(10) H. Puell. Z. Naturforsch 25a, 1807 (1970)

(11) C. Fauquignon and F. Floux. Phys. Fluids 13, 386 (1970)

(12) J. L. Bobin. Phys. Fluids 14, 2341 (1971)

(13) A. R. Fraser. Proc. R. Soc. A245, 536 (1960)

(14) G. J. Pert. Plasma Physics. 16, 1019 (1974)

(15) L. D. Landau and G. M. Lifshitz. Fluid Mechanics, Course of Theoretical Physics. Vol. 6, Pergamon Press

(16) H. Salzmann. Phys. Lett. 41A, 363 (1972)

(17) R. L. Morse and C. W. Nielson. Phys. Fluids 16, 909 (1973)

(18) R. J. Bickerton. Nucl. Fusion 13, 457 (1973)

(19) W. M. Manheimer. Phys. Fluids 20, 265 (1977)

(20) S. I. Braginskii in Reviews of Plasma Physics Vol. I, Ed. M. A. Leontovich. Consultants Bureau, New York 1965.

(21) J. B. Chase, J. M. LeBlanc and J.R. Wilson. Phys. Fluids 16, 1142 (1973)

(22) N. K. Winsor and D. A. Tidman. Phys. Rev. Lett. 31, 1044 (1973)

(23) D. A. Tidman and R. A. Shanny. Phys. Fluids 17, 1207 (1974)

(24) Los Alamos Report Jan-Jun (1975)

(25) J. A. Stamper and B. H. Ripin. Phys. Rev. Lett. 34 138 (1975).

Chapter 4

(1) R.C. Malone, R. L. McCrory and R. L. Morse. Phys. Rev. Lett. 34, 721 (1975)

(2) Los Alamos Report Jan-Jun (1977) p.87-92.

(3) R.E. Dyer, D. J. James, G. J. Pert, S. A. Ramsden and M. A. Skipper in Laser Interaction with Matter and Related Plasma Phenomena, Vol. 3, Ed. H.Schwarz and H. Hora. Plenum Press, New York.

(4) M. Rabeau, M. Rostaing and D. Colombant, Paper given at Congress du Centenaire de la Societe Francais de Physique at Vittel, June 1973.

Chapter 5

(1) L. Spitzer. Physics of Fully Ionized Gases. Interscience Publishers, Inc., New York, 1956.

(2) G. J. Pert. Plasma Physics 20, 175 (1978)

(3) S. F. Smerd. Australian J. of Sc. Research 3, 376 (1950)

(4) J.C. Jaeger and K. C. Westfold. Australian J. of Sc. Research 3, 34 (1950).